The low-lying dipole response of medium-mass nuclei - Study of ^{64}Ni using complementary real-photon scattering experiments

Inaugural-Dissertation

zur
Erlangung des Doktorgrades
der Mathematisch-Naturwissenschaftlichen Fakultät
der Universität zu Köln

vorgelegt von

Miriam Müscher
aus Olpe

Köln 2023

Diese Arbeit stellt eine von der Mathematisch-Naturwissenschaftlichen Fakultät der Universität zu Köln angenommenen Dissertation dar.

Berichterstatter:	Prof. Dr. Andreas Zilges Prof. Dr. Jan Jolie
Tag der mündlichen Prüfung:	16. Januar 2024

Abstract

This thesis deals with the analyses of real-photon scattering experiments to investigate the dipole response of the proton-magic $Z = 28$ nucleus ^{64}Ni. Studies based on the (γ, γ') reaction are commonly performed up to the particle-separation energies of the nuclide of interest. Up to these energies, $E1$ decays are mainly associated with the Pygmy Dipole Resonance (PDR) and $M1$ transitions above 5 MeV with spin-flip resonances, i.e., transitions between spin-orbit partners ($l + 1/2 \rightarrow l - 1/2$), in the $A \approx 60$ mass region. It is of utmost importance to characterize the observed decays, i.e., differentiate between $E1$ and $M1$ transitions, for the study of the various dipole-excitation modes. Furthermore, the absolute cross sections have to be determined.

Therefore, two complementary (γ, γ') experiments were performed on ^{64}Ni. On the one hand, an energetically-continuous and mainly-unpolarized photon beam was used at the γELBE facility in Dresden-Rossendorf, Germany, to extract absolute cross sections of observed transitions. On the other hand, quasimonenergetic and linearly-polarized γ rays were utilized at the HIγS facility in Durham, US, for the distinction between $E1$ and $M1$ transitions. Both complementary measurements are necessary to obtain complete information about the dipole response of atomic nuclei.

In all, 87 1^- states and 23 1^+ levels of ^{64}Ni were firmly identified between 4.3 MeV and the neutron-separation threshold $S_n = 9.7$ MeV. For transitions up to 9.3 MeV, absolute energy-integrated cross sections were determined. Besides, absolute photoabsorption cross sections were calculated between 5.86 MeV and 9.05 MeV.

The results corresponding to the $E1$ decay channel were compared to theoretical calculations within the equation of motion (EOM) framework. Furthermore, $M1$ ground-state decays of ^{64}Ni were interpreted using two shell-model calculations.

Besides these comparisons between experiment and theory, systematic investigation of the dipole response in the $A \approx 60$ mass region were performed. Results of real-photon scattering experiments on ^{54,56}Fe, ^{58,60}Ni, and ^{66}Zn were compiled together with the obtained results of ^{64}Ni and compared. Based on this compilation, it was concluded that the nuclear shell structure has not only an impact on the spin-flip resonance but also on the PDR in this region of the nuclear chart.

Contents

1 Introduction

The properties of light with various wavelengths and its interaction with matter can be observed in many different aspects of our daily life. For instance, a rainbow just occurs due to the interaction (refraction, internal reflection, and dispersion) of visible light (typical wavelength in the order of 10^{-6} m) with rain droplets. Also photons with more energy, i.e., a shorter wavelength (10^{-10} m), and their interaction with matter have found a way in everybody's life: X rays discovered by Wilhelm Conrad Röntgen in 1895 [1] are commonly-used for the investigation of the human body. Even higher-energetic photons with wavelengths in the order of 10^{-12} m are used in medicine in form of, e.g., radiotracers [2]. These are only some examples for the occurrence and usage of photons of all wavelengths in our daily life and a variety of other important phenomena and applications exists. As it can be seen, the research in this field led to some important discoveries for humankind. Therefore, the continuation of studying photons and their interaction with matter and the resulting improved understanding of observed phenomena may find important applications.

It was found that atomic nuclei can be excited by the absorption of γ rays if certain conditions are fulfilled. These resonances, which are predominantly dipole excitations if they are induced by photons, occur due to different underlying structures and properties of the nucleus. In Fig. 1.1, the dipole modes below 20 MeV are schematically shown in a simple and (mostly) macroscopic way. As indicated, the excitation energies E_X are partly overlapping and, for studying the individual dipole excitations, a distinction between the different modes is crucial. The most obvious differentiation can be done with respect to the radiation character, i.e., if an electric (upper part of the figure) or a magnetic dipole excitation (lower part of the figure) is observed. Both are discussed in the following.

1.1 Electric-dipole (E1) excitation modes

Already in 1937, the first evidence for the IsoVector Giant Dipole Resonance (IVGDR) was discovered by Bothe and Gentner [4]. They accelerated protons up to 440 keV and exploited

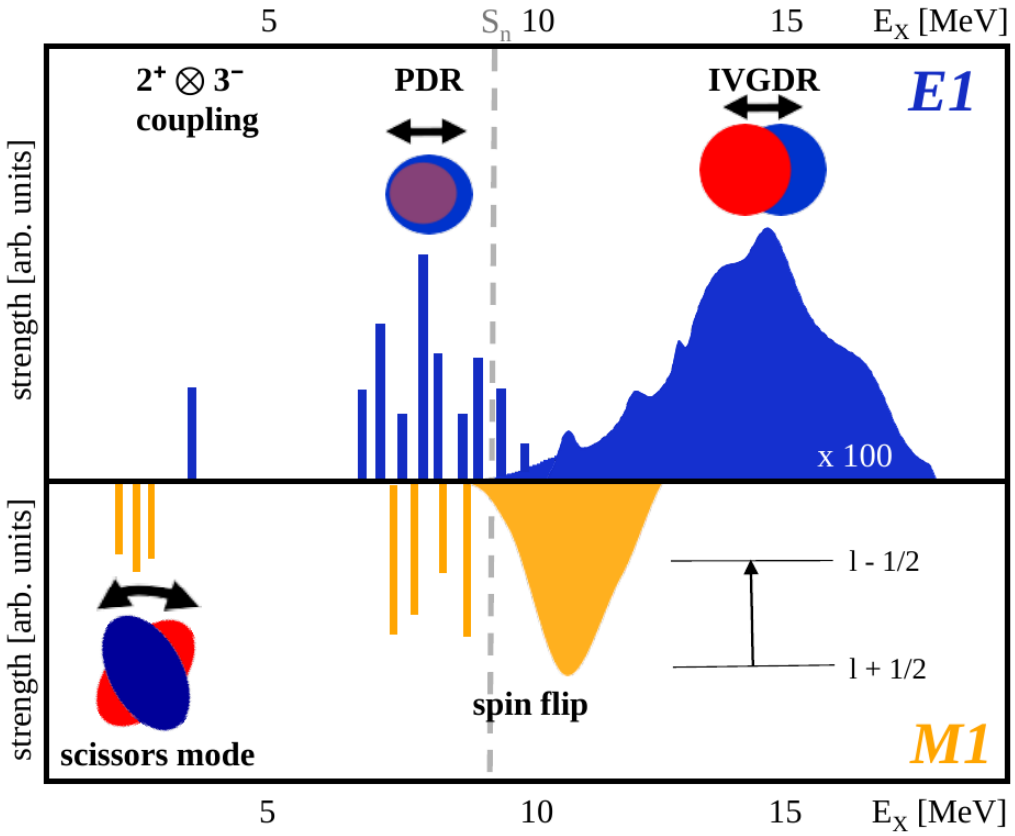

Figure 1.1: The different dipole-excitation modes in dependence on the excitation energy are schematically illustrated in a simplified way. In the upper part, the electric dipole ($E1$) modes are shown. It has to be noted that the states corresponding to the quadrupole-octupole ($2^+ \otimes 3^-$) coupling and the Pygmy Dipole Resonance (PDR) are depicted enlarged. In the lower part, the magnetic dipole ($M1$) excitation modes are shown. The scissors mode occurs only in well-deformed nuclei. The figure is a modified version of Fig. 1 in Ref. [3].

the $^7Li(p,\gamma)$ reaction to produce γ rays between 14 and 17 MeV. The investigation of the photodissociation process (γ, n) revealed enhanced cross sections for different nuclei. Bothe and Gentner proposed resonances as possible reason for their findings. In 1944, it was discovered that dipole excitations give rise to the enhanced cross section [5]. The performance of systematic studies led to the observation of many fundamental properties of the IVGDR. For a detailed compilation, see Ref. [6]. One example is that the centroid-excitation energy of the IVGDR can be well described by [6]

$$E_X[\mathrm{MeV}] = 31.2\, A^{-1/3} + 20.6\, A^{-1/6} \tag{1.1}$$

with A being the number of nucleons. Both terms result from a macroscopic picture of an out-of-phase, i.e., an isovector oscillation of all Z protons against all N neutrons. While the first term is associated with the Jensen-Steinwedel model which interprets the IVGDR as out-of-phase density oscillation of the neutron against the proton fluid [7], the second term results due to the Goldhaber-Teller model in which the rigid and interpenetrating proton and neutron spheres oscillate against each other [8]. Applying Eq. (1.1) results in values between $E_X = 15\,\mathrm{MeV}$ and $E_X = 20\,\mathrm{MeV}$ for most nuclei.

As displayed in Fig. 1.1, at low energies, an additional collective $E1$ excitation can be observed. In near-spherical, even-even nuclei, this 1^- state is a member of a quintuplet of negative-parity states which results from the coupling of the 2^+_1 and 3^-_1 excitation [9]. By combining information about the excitation energy ($E_X(1^-) \approx E_X(2^+_1) + E_X(3^-_1)$) and transition strengths to the one-phonon vibrational states, evidences can be found which lead to an identification of this two-phonon-coupled state and support the picture of multiphonon couplings. For further information, the reader is referred to Ref. [9] and references therein.

Between the two-phonon state and the IVGDR, i.e., in the vicinity of the neutron-separation threshold S_n, an accumulation of additional $E1$ strength was observed by Bartholomew in the 1960s [10]. Since the associated strength is small compared to that of the IVGDR, it was referred to as 'pigmy resonances' by Brzosko *et al.* [11]. Nowadays, the term Pygmy Dipole Resonance (PDR) is commonly used. In 1971, R. Mohan *et al.* interpreted the PDR in a three-fluid hydrodynamical model in which the three fluids are formed by (i) the protons, (ii) the neutrons of the $N = Z$ core, and (iii) the excess neutrons [12]. In the following years, alternative mechanisms causing $E1$ strength in atomic nuclei were discussed such as the toroidal mode [13, 14] which is still a research topic of interest [15]. A variety of macroscopic interpretations and also microscopic models were established to describe the PDR.

These are summarized and more deeply discussed in Refs. [16–18] and references therein.
Many theoretical and experimental studies have been performed to investigate the PDR (see, e.g., Refs. [17–19]). Based on these publications, the most important findings are summarized in the following.
For the last decades, a variety of experiments have been performed to study the PDR. Since the PDR is a dipole-excitation mode, it is plausible to investigate it, among others, with probes which selectively induce dipole excitations from the ground state, such as photons [20–22]. Therefore, many real-photon scattering experiments have been performed along isotopic (e.g., $Z = 50$ [23–27]) and isotonic (e.g., $N = 50$ [28–33]) chains to investigate the evolution of the PDR with increasing neutron excess and deformation. For a complete list, the reader is referred to Ref. [22].
Besides, systematic experimental and theoretical studies using different probes, recently denoted as 'multi-messenger investigation' [34], for the excitation of the PDR states were performed and revealed important properties of the PDR states.
On the one hand, a splitting of the PDR was observed by investigating ^{140}Ce [35], ^{138}Ba [36], and ^{124}Sn [37] in real-photon scattering and $(\alpha, \alpha'\gamma)$ experiments with α energies of $E_\alpha = 136\,\mathrm{MeV}$ and at forward angles with respect to the incoming particle beam. It was found that the α particles induced $E1$ transitions only up to approximately 6 MeV whereas $E1$ excitations up to approximately 9 MeV were observed in the real-photon scattering experiment. It was concluded that the different excitation pattern results due to different underlying structures of the states. Whereas an α particle is a hadronic probe which mainly interacts with the surface of the nucleus (using these kinematic conditions), a photon interacts with the complete nucleus via the electromagnetic interaction. Hence, it was concluded that the lower-lying levels have a strong isoscalar character and surface-peaked transition densities whereas the states only excited by photons exhibit a more isovector nature. This observation was supported by theory by investigating the contributions of the electromagnetic and isoscalar dipole operator independently [37]. Further studies with hadronic probes such as (^{17}O,$^{17}O'\gamma$) [38–40] or $(p, p'\gamma)$ [34] experiments were performed and the results confirm the previous finding. This difference of the excitation patterns was observed in all nuclei which have been studied in both (γ, γ') and $(\alpha, \alpha'\gamma)$ experiments so far.
On the other hand, very recently, the microscopic structure of PDR states was investigated in (d, p) [41, 42] and $(d, p\gamma)$ studies [43] by quantifying the (relative) one-particle-one-hole $(1p-1h)$ contributions to the wave functions associated with the excited states. In the case of ^{120}Sn, energetically lower-lying $J = 1$ states (up to approximately 7.5 MeV) were excited in real-photon scattering and in the ^{119}Sn$(d, p\gamma)$ experiment. However, ground-state decays of

higher-lying states were only observed in the (γ, γ') measurement [43]. It has been shown that this behavior is predicted by the quasiparticle-phonon model (QPM), and it was discovered that the lower-lying states are dominated by $1p-1h$ configurations whereas the contributions of more complex configurations, i.e., two-particle-two-hole and three-particle-three-hole excitations becomes more important at higher excitation energies. The theoretical calculations showed that the fraction of decays directly back to the ground state becomes smaller with increasing excitation energy and with the correspondingly increasing complexity of the configurations contributing to the states.
Indeed, the analysis of a (γ, γ') experiment on ^{120}Sn using a quasimonoenergetic photon beam revealed the decreasing fraction of ground-state decays at higher excitation energies [44]. By combining the dipole strengths included in ground-state transitions and decays via intermediate states to the ground state, not only the deexcitation but also the excitation behavior can be studied in real-photon scattering.
Although many new insights were gained in the last years, some aspects concerning the PDR are still not fully understood such as its collectivity or the interplay of isoscalar and isovector contributions. Therefore, further studies on experimental and theoretical sides are needed to answer these questions.

1.2 Magnetic-dipole (M1) excitation modes

Besides various $E1$ excitation modes, different mechanisms to induce $M1$ excitations exist. These are divided into orbital $\vec{l}$ and spin $\vec{s}$ excitations. This is also expressed by the magnetic dipole operator in fermion space

$$T(M1) = \sqrt{\frac{3}{4\pi}} \sum_i (g_l(i)\vec{l}_i + g_s(i)\vec{s}_i)\mu_N \tag{1.2}$$

with g_l and g_s being the orbital and spin g factor, respectively [45]. The following discussion of $M1$ excitations is based on Refs. [6, 45] if not other stated. As illustrated in Fig. 1.1, in general, two magnetic dipole excitation modes can be differentiated.
As seen for the $E1$ excitations, two-phonon states can be built by the coupling of two phonons. Such a phenomenon is present for the magnetic dipole transitions as well: the isoscalar one-phonon 2^+_1 excitation is coupled to the isovector (also called mixed-symmetry *ms*) one-quadrupole phonon state $2^+_{1,ms}$ which generates a two-phonon quintuplet of mixed-symmetry states $J^\pi = 0^+, 1^+, 2^+, 3^+, 4^+$ [46].

In well-deformed nuclei, the 1^+_{ms} member of this quintuplet forms the scissors mode. This name results from the scissors-like orbital oscillation of protons and neutrons. It was predicted in two different theories [47–50] and discovered in an electron-scattering experiment in the 1980s [51]. Since then, it has intensively been studied in a variety of theoretical calculations and (e, e') and (γ, γ') experiments. It was found that, in all known cases, the scissors-mode strength is fragmented and included in more than one 1^+ state as indicated in Fig. 1.1. It turned out that the mean excitation energy and the reduced $B(M1)$ strength of the scissors mode are dependent on the deformation parameter β_2 and its square [52], respectively.

In contrast to the orbital scissors mode, the spin-flip resonance is associated to the spin part of the $M1$ operator given in Eq. (1.2). As displayed in Fig. 1.1, this magnetic dipole excitation results from single-particle transitions of nucleons between two spin-orbit partners, i.e., $l + 1/2 \rightarrow l - 1/2$. In the $A \approx 60$ ($A \approx 90$) region, observed spin-flip strength is mainly associated with $1f_{7/2} \rightarrow 1f_{5/2}$ ($1g_{9/2} \rightarrow 1g_{7/2}$) excitations. It is located at

$$E_X[\mathrm{MeV}] = p \cdot A^{-1/3} \tag{1.3}$$

where the factor p is approximately $p \approx 35$ ($p \approx 45$) for light (heavy) nuclei [6]. The origin of the spin-flip resonance and this shell-model like excitation-energy dependence indicate that this excitation mode can be well described in shell-model calculations. However, several comparisons between shell-model calculations and experiment have shown that the total spin-flip strength is overpredicted by theory. Therefore, an effective g factor has to be introduced which corrects for this quenching and is in the order of $g_{\mathrm{eff}}/g_{\mathrm{free}} \approx 0.7$. It accounts for more complex interactions and effects within the nucleus. The reader is referred to Refs. [6, 45] and references therein for more information.

As it can be seen, the dipole response of atomic nuclei consists of a variety of different excitation modes with very different generation mechanisms. The corresponding properties were found by many experimental and theoretical studies.
In this work, the systematic investigation with respect to the Pygmy Dipole Resonance and the spin-flip resonance is continued by two complementary real-photon scattering experiments on the proton-magic $Z = 28$ nucleus ^{64}Ni. The combination of experiments with a linearly-polarized, quasimonoenergetic γ-ray beam and an energetically-continuous, mainly-unpolarized bremsstrahlung beam enables the clear distinction between $E1$ and $M1$ transitions and the determination of absolute cross sections. Furthermore, the ratios of ground-state decays and decays to intermediate states are investigated which give, as stated before, a first

indication of the complexity of the excited states. Real-photon scattering experiments on ^{54,56}Fe and ^{58,60}Ni have already been analyzed [53–57] and also the $N = 36$ isotone ^{66}Zn has been studied in (γ, γ') experiments [58, 59]. Hence, the evolution of these two dipole excitation modes with increasing neutron number as well as with increasing proton number can be investigated and the impact of crossing the magic proton shell can be tested.

The thesis is structured as follows: in the following chapter, the formalism of real-photon scattering experiments is introduced. In Chapter 3, the experimental facilities and setups used for the experiments on ^{64}Ni are presented and experimental details are given. This is followed by a detailed description of the data analyses. A manuscript, in which part of the results of this work will be published in combination with theoretical calculations, is included in Chapter 5. The results of (γ, γ') studies in the $Z = 28$ region are shown and compared to the results obtained for ^{64}Ni in Chapter 6. In the last chapter, the work is summarized and an outlook is given.

2 Nuclear Resonance Fluorescence

The Nuclear Resonance Fluorescence (NRF) technique is based on the excitation of a nuclear state by the absorption of a real photon and the subsequent deexcitation by the emission of, at least, one γ ray. Therefore, the corresponding measurements are also called (γ, γ') or real-photon scattering experiments. This implies that the NRF approach is mostly used to investigate states below particle-separation thresholds. This chapter gives a short overview about the principles of (γ,γ') measurements and the underlying physics. For more details, see, e.g., Refs. [20–22].

To introduce the NRF formalism, it is assumed that the nucleus is excited out of its ground state, which is in the case of an even-even nucleus a $J_0^{\pi_0} = 0^+$ state, via the absorption of a real photon γ_1 with angular momentum L_1. The spin and parity quantum number of the excited state is denoted by $J_1^{\pi_1}$. The subsequent decay of this excited state happens via the emission of a photon γ_k and can either be to an intermediate state $J_k^{\pi_k}$ ("inelastic" transition) or directly back to the ground state $J_k^{\pi_k} = J_0^{\pi_0}$ ("elastic" decay) (cf. Fig. 2.1). It has to be mentioned that the denotation "elastic" does not mean that the energy of the photon in the exit channel is the same as in the entrance channel. The energies of the exciting γ_1 and deexciting $\gamma_{1'}$ photons have to be different even in the elastic-decay channel due to the recoil energy of the nucleus during absorption and emission.

From the conservation of angular momentum and parity, the well-known selection rules for a γ-ray transition from an initial state i to a final state f result

$$
\begin{aligned}
&|J_i - J_f| \leq L \leq J_i + J_f \\
&\quad \pi_f = (-1)^L \cdot \pi_i \qquad \text{electric radiation} \qquad \Pi = E \\
&\quad \pi_f = (-1)^{L+1} \cdot \pi_i \qquad \text{magnetic radiation} \qquad \Pi = M.
\end{aligned}
\tag{2.1}
$$

In fact, photons transfer only small angular momenta limiting all following considerations predominantly to electric dipole $\Pi L = E1$ and magnetic dipole $\Pi L = M1$ transitions and with a lower probability to electric quadrupole $\Pi L = E2$ transitions. When one of the involved states has spin-parity quantum number of $J^\pi = 0^+$ and the radiation's multipolarity and character ΠL can be determined, by applying Eq. (2.1) the spin-parity quantum number

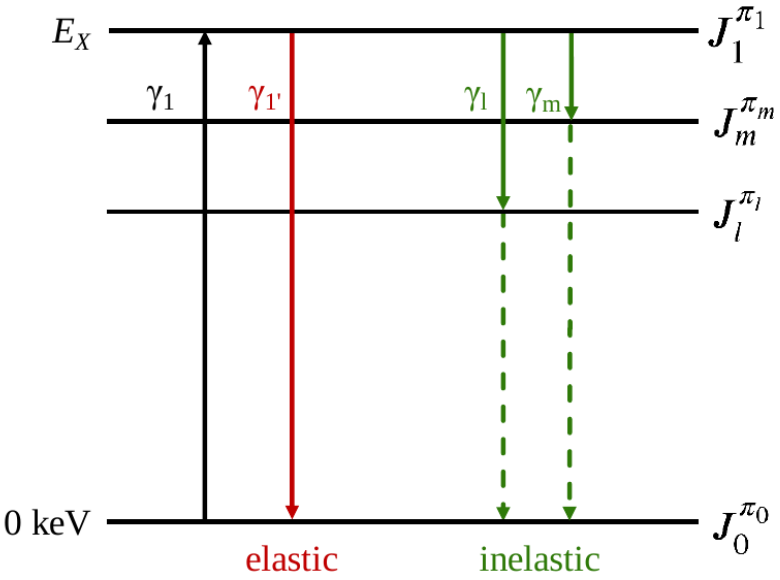

Figure 2.1: The NRF method is schematically illustrated. The atomic nucleus is excited from its ground state $J_0^{\pi_0}$ to an excited state $J_1^{\pi_1}$ by the absorption of a photon γ_1. Afterwards, the state decays back to the ground state either directly (elastic decay) or via intermediate states $J_k^{\pi_k}$ (inelastic decay) by the emission of at least one γ ray. Both decay possibilities are shown as red and green arrows, respectively.

of the other involved state can be assigned. For the identification of the transition, angular distributions are investigated.

2.1 Angular distributions

As stated above, the angular distribution of deexciting γ rays can be used to assign the multipolarity L and the radiation character Π to the occurring transition. The following discussion and introduction to angular-correlation theory is suited for (γ, γ') investigations and may deviate for other kinds of nuclear reactions.

Because the excited state is oriented by the absorption of the incoming photon γ_1, a non-equal population $P(m_i)$ of the magnetic substates m_i is created. If the angular distribution of the outgoing γ ray γ_k is measured, angular-correlation theory can be applied [21, 22, 60, 61].
At first, the discussion is focused on angular distributions for a (γ, γ') experiment in which neither the incoming photon beam nor the target nucleus is polarized.
The photon beam impinges on the target and induces an excitation from the ground state J_0 to an excited state J_1 by the absorption of a photon γ_1 and the deexciting γ ray γ_k resulting

from the subsequent decay to state J_k is observed. The corresponding angular-correlation function $W(\theta)$, with θ being the angle between the directions of motion of the two photons, is calculated via [61]

$$W(\theta) = \sum_{\nu=0}^{\text{even}} A_\nu(\gamma_1) \cdot A_\nu(\gamma_k) \cdot P_\nu(\cos(\theta)) \tag{2.2}$$

where $P_\nu(\cos(\theta))$ denotes the ordinary Legendre polynomial and A_ν are the expansion coefficients defined via F coefficients which are tabulated, for example, in Ref. [60] as:

$$A_\nu(\gamma_1) = \left(\frac{1}{1+\delta_1^2}\right) \cdot [F_\nu(L_1 L_1 J_0 J_1) + 2\,\delta_1 F_\nu(L_1 L_1' J_0 J_1) + \delta_1^2 F_\nu(L_1' L_1' J_0 J_1)] \tag{2.3}$$

$$A_\nu(\gamma_k) = \left(\frac{1}{1+\delta_k^2}\right) \cdot [F_\nu(L_k L_k J_k J_1) + 2\,\delta_k F_\nu(L_k L_k' J_k J_1) + \delta_k^2 F_\nu(L_k' L_k' J_k J_1)]. \tag{2.4}$$

The square of the so-called mixing ratio δ is the ratio of the intensities of competing radiation multipole orders L and $L' = L + 1$ which has to be defined if more than one kind of multipolarity is allowed by the selection rules (cf. Eq. (2.1)). It can be calculated by

$$\delta_n^2 = \frac{\Gamma_{k,\Pi' L+1}}{\Gamma_{k,\Pi L}} \tag{2.5}$$

whereas the multipole-mixing ratio itself is defined as:

$$\delta_n = \frac{\langle \psi_f \mid L_n' \mid \psi_i \rangle}{\langle \psi_f \mid L_n \mid \psi_i \rangle} \tag{2.6}$$

with ψ_i (ψ_f) being the wave function of the initial (final) state. At this point, it is important to notice that Eq. (2.3) is defined for using the phase convention introduced by Krane, Steffen, and Wheeler for the multipole-mixing ratio [60]. Depending on the phase convention, the signs in Eq. (2.3) may change.

Assuming the excitation of a $J_1 = 1$ ($J_1 = 2$) state with an elastic decay back to the ground state of an even-even nucleus $J_k = J_0$, i.e., two successive pure dipole (quadrupole) transitions occur, Eq. (2.2) simplifies to

$$\begin{aligned} W(\theta) &= \frac{3}{4} \cdot (1 + \cos^2\theta) && \text{dipole transition} \\ W(\theta) &= \frac{5}{4} \cdot (1 - 3\cos^2\theta + 4\cos^4\theta) && \text{quadrupole transition .} \end{aligned} \tag{2.7}$$

The corresponding distributions are illustrated in Fig. 2.2.

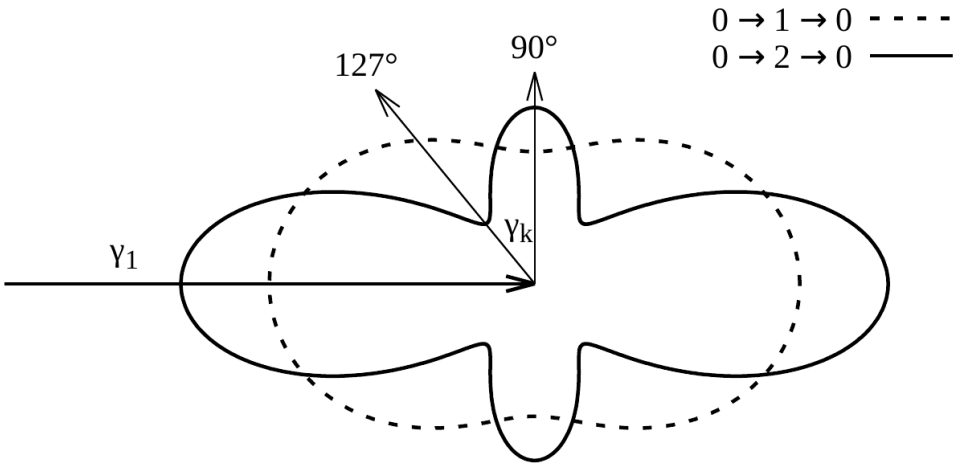

Figure 2.2: The angular distributions for a pure dipole ($0 \rightarrow 1 \rightarrow 0$) (dashed) and for a pure quadrupole transition ($0 \rightarrow 2 \rightarrow 0$) (solid) after the excitation from a $J_0 = 0$ ground state are depicted. The direction of the incoming γ-ray beam γ_1 is illustrated by the black arrow and encloses the angle θ with the deexciting photon γ_k. The scattering angles of $\theta = 90^\circ$ and $\theta = 127^\circ$ are displayed.

If the polarization is added as one observable in the experiment, the radiation character can be determined as well. In general, there are two possibilities for including polarization. On the one hand, an unpolarized incoming photon beam can be used if the polarization of the deexciting γ ray is measured $\vec{\gamma}_k$ by exploiting, e.g., the polarization dependence of the Compton effect. On the other hand, a linearly-polarized photon beam can be utilized in the entrance channel $\vec{\gamma}_1$. The deexciting photon is detected with respect to the polarization plane which is spanned by the electric-field vector of the incoming radiation and the radiation-propagation direction. The angle between the outgoing photon and the polarization plane is denoted as ϕ. The angular-correlation functions for both cases are different. Due to the relevance of the second case for this work, i.e. the polarized incident photon beam, the corresponding formalism is introduced [21, 22, 61].
For taking into account the polarized photon beam, a polarization term has to be added to the angular-correlation function for an unpolarized photon beam given in Eq. (2.2):

$$W(\theta, \phi) = W(\theta) + (\pm)_{L_1} \cdot P_\gamma \sum_{\nu=2}^{\text{even}} B_\nu(\vec{\gamma}_1) \cdot A_\nu(\gamma_k) \cdot P_\nu^{(2)}(\cos\theta) \cdot \cos(2\phi) \qquad (2.8)$$

Here, P_γ includes the degree of polarization of the γ-ray beam and $P_\nu^{(2)}$ denotes the unnor-

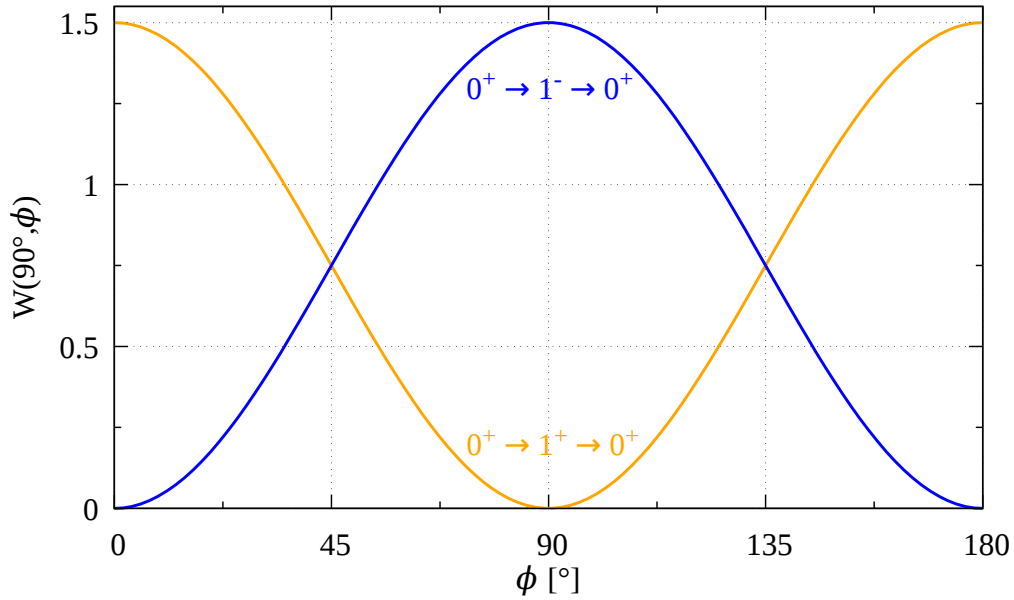

Figure 2.3: The angular distributions of pure $E1$ and $M1$ transitions in dependence on the angle between the polarization plane and the direction of movement of the outgoing photon ϕ are illustrated in blue and orange, respectively. The scattering angle $\theta = 90°$ is fixed.

malized associated Legendre polynomial of νth order. $B_\nu(\vec{\gamma}_1)$ is defined as

$$B_\nu(\vec{\gamma}_1) = \left(\frac{1}{1+\delta_1^2}\right) \cdot [\kappa_\nu(L_1 L_1) \cdot F_\nu(L_1 L_1 J_0 J_1) \\ - 2\,\delta_1 \cdot \kappa_\nu(L_1 L_1') \cdot F_\nu(L_1 L_1' J_0 J_1) - \delta_1^2 \cdot \kappa_\nu(L_1 L_1') \cdot F_\nu(L_1' L_1' J_0 J_1)] \tag{2.9}$$

where the coefficients κ_ν are given in Ref. [61]. The $\pm$ behind the angular-correlation function of an unpolarized beam is dependent on the multipole character of the leading multipole of the first photon L_1 and equals $+$ $(-)$ for an electric (magnetic) transition. By assuming pure dipole transitions in the entrance and the exit channel, Eq. (2.8) simplifies to

$$W(\theta, \phi) = \frac{3}{4}\left(1 + \cos^2\theta + \pi_1\, P_\gamma \cos(2\phi) \sin^2\theta\right) \tag{2.10}$$

with π_1 being the parity quantum number of the state which is excited by the incoming photon. This equation shows that the angular distribution is maximal for an $M1$ transition at $\theta, \phi = 90°, 0°$ and minimal at $\theta, \phi = 90°, 90°$. For an $E1$ transition, it is exactly the other way around, i.e., $W(\theta, \phi)$ is minimized for $\theta, \phi = 90°, 0°$ and maximized for $\theta, \phi = 90°, 90°$ (cf. Fig. 2.3). Further illustrations of angular-correlation functions of different transition cascades are shown, for instance, in Ref. [22].

2.2 Energy-integrated cross sections and reduced transition strengths

Besides the identification of the transitions, the probability of the occurrence of the reaction, i.e., the corresponding cross section is of importance to study excitation modes of atomic nuclei. It is described for the excitation from the ground state J_0 by a photon with energy E_γ to an excited state J_1 and its subsequent decay by a Breit-Wigner distribution [20, 22]

$$\sigma^0(E_\gamma) = \frac{1}{2}\pi \cdot \lambda\!\!\!^{-2} \cdot g \cdot \frac{\Gamma_0\Gamma}{(E_\gamma - E_r)^2 + (\Gamma/2)^2}. \tag{2.11}$$

Here, $\lambda\!\!\!^{-}$ equals the reduced wavelength of the photon, E_r denotes the resonance energy including the nuclear recoil, and g is the so-called spin factor $g = \frac{2J+1}{2J_0+1}$ which takes into account the degeneracy of the magnetic substates. When the cross section of one specific γ-decay channel is of interest, the total decay width Γ in the numerator of Eq. (2.11) has to be replaced by the corresponding partial decay width Γ_k.
On resonance, i.e., if the photon energy E_γ equals the resonance energy E_r, Eq. (2.11) simplifies to

$$\sigma^0(E_r) = 2\pi \cdot \lambda\!\!\!^{-2} \cdot g \cdot \frac{\Gamma_0}{\Gamma}. \tag{2.12}$$

This results in rather high cross sections at resonance. Because the natural line widths of particle-bound states $\Gamma = \hbar/\tau$ are in the order of meV, these resonances are only very weakly excited in experiments as long as the spectral intensity of the incoming photon beam is low (as it is typically the case).

Up to this point, it was assumed that the target nuclei are at rest. This is not the case in experiments because of their thermal motion at finite temperatures. Therefore, the cross section has to be folded with a Maxwellian-velocity distribution and integrated over all possible velocities. This leads to a broadening of the cross section and the line width. By assuming that the photon flux is constant or at least linear close to the resonance energy over this effective line width, the energy-integrated cross section I_S can be defined as

$$I_S = \pi^2 \cdot \lambda\!\!\!^{-2} \cdot g \cdot \Gamma_0 \tag{2.13}$$

which is independent from the exact motions of the nuclei. For a more detailed discussion, the reader is referred to Refs. [20, 22].
Because the photoexcitation happens from the ground state, only states with sufficiently large

ground-state decay widths Γ_0 are directly excited. Γ_0 is proportional to the reduced transition strength for excitation $B(\Pi L) \uparrow$ via [21]

$$\Gamma_0 = \sum_{\Pi L} \frac{8\pi(L+1)}{L[(2L+1)!!]^2} \left(\frac{E_\gamma}{\hbar c}\right)^{2L+1} \frac{1}{g} B(\sigma L) \uparrow . \tag{2.14}$$

By applying Eq. (2.14) with respect to $E1$, $M1$, and $E2$ transitions and using the γ-ray energy E_γ in MeV and the ground-state decay width Γ_0 in meV, the corresponding reduced transition strengths can be calculated with

$$\begin{aligned} B(E1)\uparrow &= 2.86 \cdot 10^{-3} \frac{\Gamma_0}{E_\gamma^3} \qquad [\mathrm{e}^2\mathrm{fm}^2] \\ B(M1)\uparrow &= 2.58 \cdot 10^{-1} \frac{\Gamma_0}{E_\gamma^3} \qquad [\mu_\mathrm{N}^2] \\ B(E2)\uparrow &= 6.20 \cdot 10^{+3} \frac{\Gamma_0}{E_\gamma^5} \qquad [\mathrm{e}^2\mathrm{fm}^4]. \end{aligned} \tag{2.15}$$

Γ_0 can only be directly determined if either the ground-state decay is the only possible decay channel, i.e., $\Gamma_0 = \Gamma = \Gamma_k$, or all other decay channels are observed as well because the deexcitation and not the excitation process is investigated in NRF measurements.

3 Real-photon scattering on ^{64}Ni

3.1 Photon sources

There are two different methods which are most commonly used for the production of photon beams nowadays. An energetically-continuous, mainly-unpolarized bremsstrahlung beam can be generated by the deceleration of electrons in a radiator target. The Laser-Compton Backscattering (LCB) method can be utilized to produce quasimonoenergetic and linearly-polarized photons. For this generation process, laser photons [eV] are Compton backscattered off electrons with energies in the order of GeV. The laser photons experience a Lorentz boost which is the largest for a head-on collision of the particles ($E_\gamma^{\max} \approx 4\gamma^2 E_{\text{laser}}$ for ultrarelativistic electrons with the Lorentz factor $\gamma = 1/\sqrt{1-(v/c)^2}$). In this way, the photons can reach energies in the MeV range.
The characteristics of the photon beams generated by the different production mechanisms enable a complete study of excited $J = 1$ states and their decays.
By using an energetically-continuous bremsstrahlung beam, many states are excited in a single experiment and spin quantum numbers, exploiting the different angular distributions, are assigned (see Sec. 2.1). Additionally, the usage of a calibration target with known transitions distributed over the total excitation-energy range allows the determination of the absolute photon flux impinging on the target of interest. Hence, absolute quantities can be calculated. The wide excitation range holds the problem that a clear distinction between elastic and inelastic decays is not easily feasible. Therefore, an inelastic decay may be interpreted as ground-state decay and is not identified as γ-decay branch of the corresponding excited state. This prevents the calculation of reduced transition strengths $B(\Pi L)$. Moreover, higher-lying levels may decay via one of the lower-lying states before reaching the ground state. This leads to an overestimation of the energy-integrated cross section corresponding to the ground-state decay of the lower-lying, fed state. Furthermore, bremsstrahlung beams do generally not allow the determination of the radiation character since only the edges of the bremsstrahlung cone are linearly polarized.

Both problems are overcome when using the LCB technique. If the first excited state of a nucleus has a sufficiently high excitation energy, all transitions, which occur in the energy range covered by the photon flux, can firmly be identified as elastic decay and associated with a nuclear state due to the small bandwidth of the photon beam (mostly in the order of $\Delta E/E \approx 3\,\%$). Additionally, as aforementioned, the photon beam is linearly polarized which enables the study of the transition's multipole character by using the different angular distributions of electric and magnetic radiations. Besides all these advantages, the use of a calibration standard is not easily feasible due to the small bandwidth, i.e., the determination of the absolute photon flux impinging on the target is more difficult. Hence, already known transitions of the target of interest itself are often used for the calibration.

To conclude, both techniques have advantages and disadvantages. In general, the bremsstrahlung and the LCB experiments serve as complementary measurements and both have to be performed to obtain all information about the observed states and transitions of the nucleus of interest.

3.2 Experimental facilities and setups

Two different kinds of NRF experiments were performed on ^{64}Ni: (i) two bremsstrahlung measurements with different maximal photon energies at the γELBE facility of the Helmholtz-Zentrum Dresden-Rossendorf (HZDR), Germany [62] and (ii) an LCB experiment at the High Intensity γ-ray Source (HIγS) facility at the Duke University and TUNL in the US [63]. In the following, both facilities and the setups are presented and experimental details are given.

3.2.1 γELBE

This section gives a short overview about the NRF setup at the Helmholtz-Zentrum Dresden-Rossendorf (HZDR). All information were taken from and additional information can be found in Ref. [62].
At the ELBE (Electron Linear accelerator of high Brilliance and low Emittance) facility, the superconducting accelerator can accelerate electrons up to 20 MeV with average currents up to 1 mA. After the acceleration, the electron beam is deflected and focused on a niobium radiator by multiple dipole and quadrupole magnets. The high melting point (2468°C) and the medium atomic number of niobium ($Z = 41$) make it a good radiator material. Six Nb radiators are installed with varying thicknesses between 1.7 mg/cm^2 and 10.6 mg/cm^2. The radiator targets can easily be interchanged during the experiment depending on the experi-

mental needs. All electrons which pass the radiator are deflected from the bremsstrahlung beam into a beam dump by another dipole magnet. Behind the Nb radiator, an aluminum beam hardener can be moved into the γ-ray beam to reduce, especially, the low-energy photons. The generated photon beam is guided by a 2600 mm-long aluminum ($S_n = 13.1$ MeV) collimator, which is positioned 1 m behind the radiator, through a 1.6 m-thick concrete wall to the NRF setup. At the entrance, the collimator has a diameter of 5 mm and, at the exit, of 24 mm.

In the experimental hall, the γ-ray beam passes a CD_2 film which is surrounded by four silicon detectors perpendicular to the beam ($\theta = 90^\circ$) and at azimuthal angles ϕ of 0°, 90°, 180°, and 270°. This setup can be used to determine the maximal photon energy by exploiting the well-known process of photodisintegration of deuterons and the determination of the maximal kinetic energy of the emitted protons.

Afterwards, the γ rays impinge on the targets (the calibration target and the target of interest) and the deexciting photons are recorded by four High-Purity Germanium (HPGe) detectors. Each has a full-energy-peak (FEP) efficiency of 100 % relative to a 3 inch x 3 inch NaI detector at 1332 keV. Two of these are positioned at $\theta = 90^\circ$ relative to the beam axis and two at $\theta = 127^\circ$. All four detectors are surrounded by passive background-suppression lead shields of 10 cm thickness with conical holes acting as collimators for the HPGe detectors and active Compton-suppression bismuth-germanate (BGO) scintillators (which serve as passive background shield as well). Additionally, thin absorption filters made of lead and copper can be placed in front of the detectors for the reduction of, especially, low-energy photons. Behind the NRF setup, the photon-beam dump is located.

Experimental details of the bremsstrahlung measurements

In this experiment, no beam hardener was positioned in the beam line. The ^{64}Ni target was a metallic disk with a diameter of 1.9 cm, a weight of 1456.56 mg, and an isotopic enrichment of 92.1 %. As calibration standard a 300 mg ^{11}B target with an isotopic enrichment of 99.5 % was used. The deexciting γ rays were detected by two 100 % HPGe detectors at $\theta = 127^\circ$ ($\theta = 90^\circ$) relative to the beam axis with a distance of 28 cm (32 cm) to the target. More details with respect to the two measurements are given in Table 3.1. The neutron-separation energy of ^{64}Ni equals $E_\gamma = 9.7$ MeV which is 0.3 MeV higher than the maximal photon energy of the high-energy (HE) measurement $E_{\mathrm{max}}(\mathrm{HE}) = 9.4$ MeV.

Table 3.1: Experimental details of the bremsstrahlung experiments on ^{64}Ni.

	low-energy (LE) measurement	high-energy (HE) measurement
E_{max} [MeV]	7.3	9.4
measuring time [h]	120	80
average current [μA]	604	604
Nb thickness [μm]	7	12.5
filter at 90°	3 mm Pb + 3 mm Cu	8 mm Pb + 3 mm Cu
filter at 127°	3 mm Pb + 3 mm Cu	3 mm Pb + 3 mm Cu
source measurement	^{226}Ra	-

3.2.2 HIγS

In this section, information, relevant for this work, about the HIγS facility [63] and the γ^3 setup [64] are compiled.

The HIγS facility is a joint project between the Duke Free Electron Laser Laboratory (DFELL) and the Triangle Universities Nuclear Laboratory (TUNL) [63]. At HIγS, the Laser-Compton-Backscattering (LCB) process is used to generate the quasimonoenergetic and polarized photon beam.

Electrons are preaccelerated by a linear accelerator ($0.18 - 0.28$ GeV) and, afterwards, injected in a booster synchrotron where the electrons can be accelerated up to 1.2 GeV. Then, the electron beam is guided to the electron-storage ring. This consists of two 34 m long straight sections, one includes the injector and the other one the Free Electron Laser (FEL), and two 20 m arcs. Approximately in the magnetic field-free center of the FEL straight section, the collision point for photons and electrons is located. For the production of γ rays, the storage ring is operated in a two-bunch mode, i.e., two electron bunches, which are equally separated, circulate in the storage ring at the same time.

The polarization of the photon beam is achieved by using polarized laser photons. Compton-scattering processes conserve the polarization, i.e., if linearly-polarized laser photons are used in the entrance channel, the γ rays are linearly polarized as well. At HIγS, a linearly- as well as a circularly-polarized photon beam can be produced. In the following, it is focused on the generation of the linear polarization since this was used during the (γ, γ') experiment on ^{64}Ni.

The OK-4 FEL consists of a system of wiggler magnets which periodically reflect the elec-

tron beam in the horizontal plane. Therefore, the electrons' trajectories are sinusoidal. This implies that the electrons experience an acceleration and, in this way, synchrotron radiation, which is polarized in the plane of the trajectory, is produced. The laser photons are reflected back and forth along the FEL-straight section of the storage ring by a system of optical mirrors. The distance between the mirrors is 54 m. In the magnetic field-free center of the FEL-straight section, the photons, generated by one electron pulse, collide with the second electron beam. This produces a γ-ray burst every 179 ns. Because the mirrors are transparent for high-energy photons, the γ rays can pass the mirrors and propagate through a collimator to the experimental areas.
The HIγS facility provides γ-ray beams with energies between 1 and 100 MeV and a degree of polarization of $> 95\,\%$. Depending on the experimental needs, the γ rays can be produced in either the pulsed or the quasicontinuous-wave (cw) mode. Furthermore, the experiment can be conducted in the high-flux or the high-resolution mode. If the high-flux mode is chosen, photon fluxes in the order of $10^9\gamma$/s for γ-ray energies between 5 MeV and 20 MeV with an energy resolution of $\Delta E/E \approx 3\,\%$ can be achieved. By using the high-resolution mode, the energy resolution can be improved at the expense of a reduced photon flux.

The γ^3 setup [64], used for the experiment on ^{64}Ni, is located approximately 60 m behind the collision point. Before reaching the setup, the photon beam is again collimated (diameter between 1/2 inch and 3/4 inch) and, then, propagates through a plastic beam pipe, which can be evacuated, to the γ^3 setup. There, it impinges on the target which is surrounded by four HPGe and four $LaBr_3$ detectors. All detectors have cylindrical shapes. Several HPGe detectors are available at HIγS with relative FEP efficiencies of 55 % and 60 %. The $LaBr_3$ detectors have diameters and lengths of 3 inch. The positions of the detectors during the ^{64}Ni experiment are given in Table 3.2. Furthermore, a 123 % HPGe detector (also denoted as 0° detector) is used which can be automatically moved and positioned directly in the beam for the detection of the incoming photon spectrum before each measurement. It is shielded by thick copper absorbers to decrease the beam intensity during these measurements.
Two independent data-acquisition (DAQ) systems are utilized. The genie system is an analog DAQ which reads out the signals detected by the HPGe detectors only. Additionally, the digital GSI Multi Branch System (MBS) [65] is used to process the signals of all detectors, i.e., the HPGe and $LaBr_3$ detectors, and stores these on an event-by-event basis with certain trigger conditions. Because the MBS records the energy and the time information of the incoming signals, the resulting data can be used for $\gamma - \gamma$ coincidence analyses. For more information about the γ^3 setup, the reader is referred to Ref. [64]

The statistics (due to a lower dead time) and energy resolution achieved by the genie DAQ are better than that of the MBS. Therefore, the singles spectra are commonly analyzed using the genie data.

Experimental details of the HIγS measurements

For the experiment on ^{64}Ni, the γ-ray beam was generated in the cw mode in combination with the high-flux mode. A 3/4 inch collimator was used which approximately matches the diameter of the coin-like ^{64}Ni target which was also used in the bremsstrahlung measurement. Moreover, a pencil-like ^{64}Ni target was positioned in the γ^3 setup during measurements at high energies. This was also a metallic target with a diameter of 8 mm and a total weight of 4 g (92.3 % isotopic enrichment), i.e., the diameter was smaller than that of the beam. In Table 3.2, the most relevant information about the experiment is given. The distances between the detectors and the target, and the copper and lead filters in front of the detectors were changed two times during the experiment depending on the count rates of each detector.

Table 3.2: Experimental details of the experiments on ^{64}Ni at HIγS.

E_{beam} [MeV]	4.33, 4.48, 4.63, 4.75, 4.95, 5.13, 5.43, 5.63	5.86, 6.15, 6.38, 6.55, 6.75, 6.95, 7.15, 7.35, 7.55, 7.8, 8.05, 8.3, 8.55, 8.8, 9.05	9.3, 9.6, 10.0
target	coin	coin	pencil like
measuring time [h]	$\approx 2-3$ each	$\approx 3-4$ each	$\approx 3-4$ each
source	^{56}Co	^{56,60}Co, ^{152}Eu	^{56}Co, ^{152}Eu
distances between detectors (θ, ϕ) and target [mm], thicknesses of absorbers [mm]			
HPGe 1	X	(135°, 315°), 130.0, 1.02 (Cu), 0.9 (Pb)	(135°, 315°), 179.0, 1.15 (Cu), 1.9 (Pb)
HPGe 2	(90°, 90°), 60.4, 1.15 (Cu), 1.2 (Pb)	(90°, 90°), 79.5, 1.02 (Cu), 1.4 (Pb)	(90°, 90°), 140, 1.15 (Cu), 4.63 (Pb)
HPGe 3	(135°, 45°), 130.0, 1.15 (Cu), 1.2 (Pb)	(135°, 45°), 122.0, 1.02 (Cu), 0.98 (Pb)	(135°, 45°), 152.0, 1.15 (Cu), 0.8 (Pb)
HPGe 4	(90°, 0°), 61.0, 1.2 (Pb)	(95°, 180°), 108.5, 1.85 (Pb)	(95°, 180°), 185.0, 6.05 (Pb)
$LaBr_3$ 1	X	(90°, 0°), 71.5, 1.15 (Cu)	(90°, 0°), 83.4, 1.15 (Cu)
$LaBr_3$ 2	(90°, 270°), 59.4, 1.15 (Cu)	(90°, 270°), 75.0, 1.15 (Cu)	(90°, 270°), 88.4, 1.15 (Cu)
$LaBr_3$ 3	(135°, 225°), 72.0 -	(135°, 225°), 98.0 -	(135°, 225°), 100.0, 3.15 (Cu)
$LaBr_3$ 4	(135°, 135°), 69.0 -	(135°, 135°), 92.5, -	(135°, 135°), 124.0 3.15 (Cu)

4 Data analyses

In this chapter, the analysis procedures for the two complementary (γ, γ') experiments are discussed. One aim of both analyses is the extraction of energy-integrated cross sections I_S. These are calculated by correcting the peak area A deduced from the recorded deexcitation spectra for the number of target nuclei N_T, the photon flux impinging on the target $N_\gamma(E_X)$, the detection efficiency $\epsilon(E_\gamma)$, and the angular distribution $W_{\Pi L}(\theta, \phi)$ [22]:

$$I_S = \frac{A}{N_T \cdot N_\gamma(E_X) \cdot \epsilon(E_\gamma) \cdot W_{\Pi L}(\theta, \phi)}. \tag{4.1}$$

The analysis steps for receiving these quantities are explained in the following.
Besides this state-by-state analysis, average cross sections were extracted from the HIγS data. The corresponding analysis steps are explained in Sec. 4.2.6.
If not otherwise noted, the uncertainties were calculated using Gaussian uncertainty propagation.

4.1 Bremsstrahlung data of ^{64}Ni

4.1.1 Photon-flux and detection-efficiency determination

The model-independent determination of absolute energy-integrated cross sections I_S is one advantage of the NRF technique. For this purpose, the absolute product of photon flux impinging on the target $N_\gamma(E_X)$ and full-energy detection efficiency $\epsilon(E_\gamma)$ has to be known. This was determined by irradiating a calibration target in addition to the target of interest during the experiment. One commonly-utilized calibration nuclide for NRF studies is ^{11}B because of its well-distributed and strong transitions between 2 MeV and 9 MeV. Equation (4.1) was rearranged to calculate $N_\gamma\epsilon$. For this purpose, the number of target nuclei N_T, the energy-integrated cross section I_S, the angular distribution $W_{\Pi 1}(\theta)$, and the deduced peak areas, corrected for feeding contributions, A corresponding to transitions of ^{11}B were inserted. The corresponding quantities of the transitions of ^{11}B are summarized in Table 4.1. Since the bremsstrahlung beam is mainly unpolarized, the angular distribution depends only on the scattering angle θ as explained in Sec. 2.1. To obtain a functional dependence between the γ-ray energy and the product $N_\gamma \cdot \epsilon$, the shapes of both quantities have to be determined.

Table 4.1: Excitation energies E_X and energies of the final states E_f, after inelastic decays, of the relevant transitions in ^{11}B are given. The corresponding energy-integrated cross sections I_S were calculated using the total decay widths Γ of Ref. [66] and the ground-state decay branching ratios Γ_0/Γ taken from Ref. [67]. The angular distributions $W(\theta)$ were computed using the multipole-mixing ratios given in Ref. [67]. Furthermore, the ratios of the angular distributions $\omega = W(90°)/W(127°)$ are presented.

E_X [keV]	E_f [keV]	Γ_f/Γ in %	I_S [keV · fm^2]	$W(90°)$	$W(127°)$	ω
2125		100	5.1(4)	1	1	1
4445		100	16.3(6)	0.978	1.002	0.976
5020		85.8(4)	21.96(7)	0.922	1.007	0.916
	2125	14.2(4)		1.178	0.985	1.196
7286		88.4(3)	9.7(7)	0.930	1.006	0.924
	4445	5.3(4)		1.067	0.994	1.073
	5020	6.3(4)		0.937	1.005	0.932
8920		97.3(1)	29.86(15)	0.930	1.006	0.924
	4445	2.7(1)		1.068	1.027	1.040

The energy distributions of the bremsstrahlung were obtained by calculating the bremsstrahlung cross section using the process description by Roche *et al.* which takes into account the

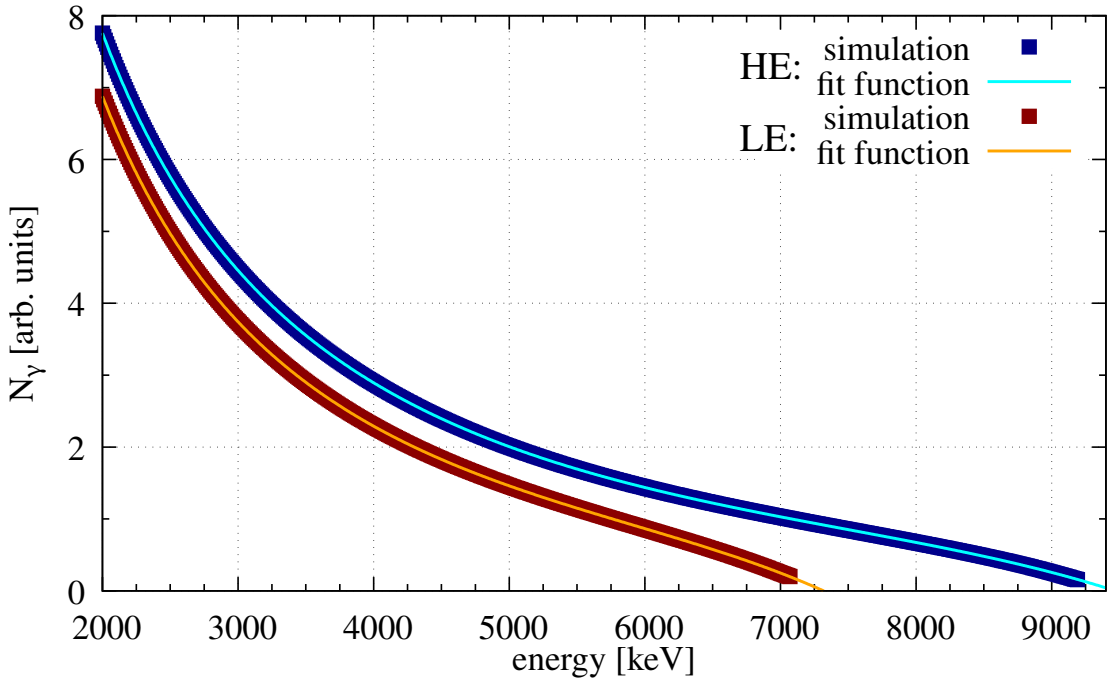

Figure 4.1: The energy distributions of the bremsstrahlung used during the HE (blue) and the LE (red) measurements at γELBE are illustrated.

Coulomb correction [68], i.e., the distortion of the plane waves associated with the incident electrons by the Coulomb field of the nuclei for low electron energies. However, it neglects the correction for the screening of the nuclear Coulomb potential by the surrounding electrons. This contribution is included in a second bremsstrahlung code that computes the Bethe-Heitler cross sections with and without the atomic screening [69]. In this way, the correction factor was extracted and subtracted from the Coulomb-corrected cross section. The computer codes were provided by E. Haug [70]. The resulting photon-flux distributions were described by polynomials of fifth order and are shown in Fig. 4.1 as blue (HE) and red (LE) squares.

The full-energy-peak (FEP) efficiencies were simulated for all detectors in the experimental setup configuration of the HE measurement using a Monte-Carlo code [71, 72] and were described by the so-called Wiedenhöver function:

$$\epsilon(E_\gamma) = a \cdot (E_\gamma - b + c \cdot \exp(-d \cdot E_\gamma))^{-e}. \tag{4.2}$$

Afterwards, the results were scaled to the extracted FEP-efficiency values of a ^{226}Ra source measurement. In Fig. 4.2, the Monte-Carlo simulations, ^{226}Ra data, and scaled Wiedenhöver functions are depicted in dark gray, red, and green, respectively. Whereas the absorbers in

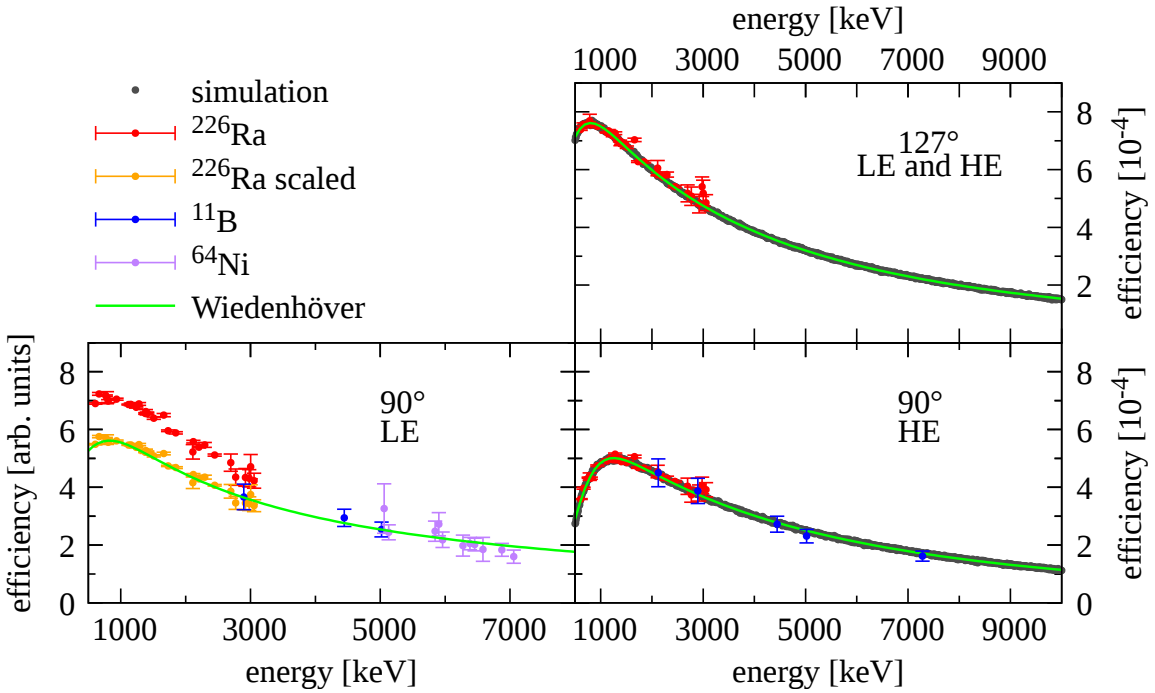

Figure 4.2: The FEP efficiencies of the detectors at $\theta = 127^{\circ}$ ($\theta = 90^{\circ}$) are depicted in the upper (lower) part of the figure. For the 90° detectors, different absorber configurations were utilized for the LE (left) and the HE (right) measurements. The calculated efficiencies of the ^{226}Ra measurement are shown in red and the scaled results of Monte-Carlo efficiency simulations in dark gray. The Wiedenhöver function was fitted to the scaled simulations (light green). In the case of the $\theta = 90^{\circ}$ detectors of the LE measurement, the Wiedenhöver function was fitted to the scaled ^{226}Ra data (orange) and the reconstructed efficiency values using transitions of ^{11}B (blue) and ^{64}Ni (purple). For details concerning the calculation and scaling, see text.

front of the backward detectors were not changed between the HE and the LE measurement, the thickness of the lead absorbers in front of the 90° detectors was reduced for the LE measurement (from 8 mm to 3 mm) (lower left part of Fig. 4.2). For this absorber configuration, no Monte-Carlo simulation existed. Therefore, the FEP efficiency was reconstructed up to the maximal photon energy by using strong dipole transitions of ^{64}Ni ($\Delta A/A < 20\%$) investigated in the LE spectra and assuming $\omega_{\Pi 1} = 0.74$ (purple data points). Therefore, it was required that these transitions were firmly identified as dipole transition in the analysis of the HE data. Furthermore, transitions of ^{11}B with statistical uncertainties $< 10\%$, and without an energetically-overlapping transition of ^{64}Ni (overlapping transitions were identified using the HIγS data) were used for this purpose (blue). The corresponding absolute FEP-efficiency values were calculated via

$$\epsilon(90^\circ) = \frac{A(90^\circ)}{A(127^\circ)} \cdot \frac{\epsilon(127^\circ) \cdot \tau(127^\circ)}{\tau(90^\circ) \cdot \omega} \tag{4.3}$$

with τ being the effective measuring times of the individual detectors. The ratios of the angular distributions ω of transitions of ^{11}B are listed in Table 4.1. To show that this method works, it was applied to the ^{11}B transitions recorded by the $\theta = 90^\circ$ detectors in the HE configuration (blue data points in the lower right part of Fig. 4.2).
As depicted in the lower left part of Fig. 4.2, the agreement between the reconstructed efficiencies and the ^{226}Ra data is rather poor. Hence, the source data were scaled to the energetically lowest-lying transition of ^{11}B which was not influenced by feeding contributions. Therefore, the γ-ray transition with $E_\gamma \approx 2895$ keV was used and not the ground-state decay of the 2125 keV level. The resulting scaling factor was applied to the source data and the results are shown as orange data points. Afterwards, the Wiedenhöver function was fitted to the scaled ^{226}Ra, ^{11}B, and ^{64}Ni data at once (light green). The deviating absolute values could be caused by, e.g., non-consistently recorded effective measuring times or inconsistent positioning of the ^{226}Ra source and the targets (^{11}B and ^{64}Ni). Since only the efficiencies' shapes and no absolute values were necessary, the differences do not impact the next steps of the analysis.

The fit functions determined to describe the photon-flux distributions and shapes of the FEP efficiencies were folded and scaled to experimental values of transitions of ^{11}B with statistical uncertainties smaller than 10 % (which excludes the decay of the 7285 keV level in the LE measurement). Furthermore, the ground-state transition of the level at 8920 keV was excluded in the HE measurement because the analysis of the HIγS data showed that a ground-state transition of ^{64}Ni energetically overlaps with this transition. Figures 4.3 and 4.4 depict the resulting absolute product $N_\gamma \cdot \epsilon$ in a logarithmic way for the backward $\theta = 127^\circ$ (red)

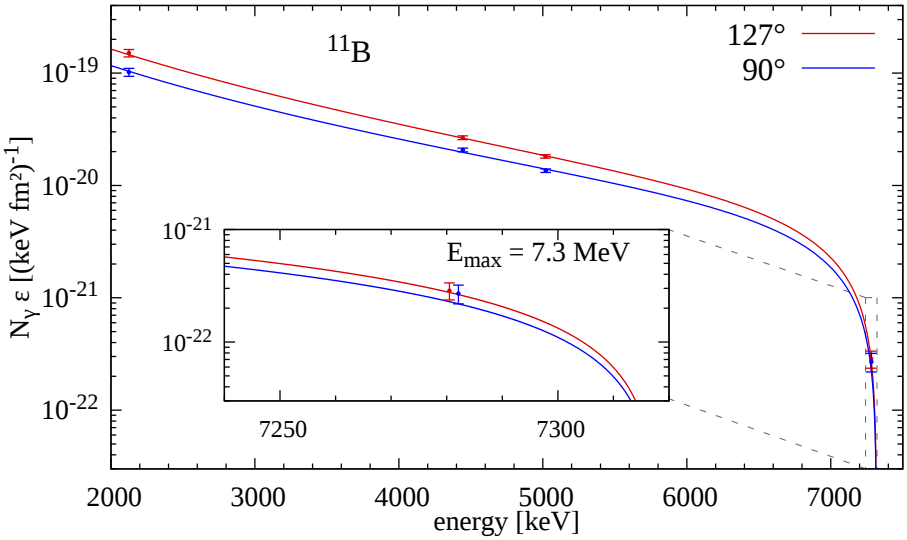

Figure 4.3: The logarithm of the product of absolute photon flux and FEP efficiencies of the LE measurement is scaled to well-known transitions of the calibration standard ^{11}B for the 127° (red) and 90° (blue) detectors.

and $\theta = 90°$ (blue) detectors for the LE and the HE measurement, respectively.
Although the ground-state decay of the 8920-keV state was not used for the scaling, the corresponding value is presented in Fig. 4.4. Because it agrees with the scaled product $N_\gamma \cdot \epsilon$, it was concluded that the transition of ^{64}Ni is comparably weak. Shown uncertainties include contributions of the peak-fitting procedure and the uncertainties of the energy-integrated cross sections I_S given in Table 4.1.
To estimate the precision of the used description of the product $N_\gamma \cdot \epsilon$ with respect to the calculated ^{11}B values, the corresponding relative deviations were computed (cf. Fig. 4.5). Based on this, the systematic uncertainty introduced by the functional description was estimated to be 10 %. The larger deviation and the large error bars corresponding to the 7283 keV decay recorded by the $\theta = 90°$ detectors are probably caused by the vicinity to the maximal photon energy of the bremsstrahlung spectrum where the photon intensity steeply decreases. Because this steep decrease starts approximately at 6500 keV (cf. Fig. 4.3), the uncertainty above this energy was estimated to be 20 % which is in accordance with the deviation observed in Fig. 4.5.

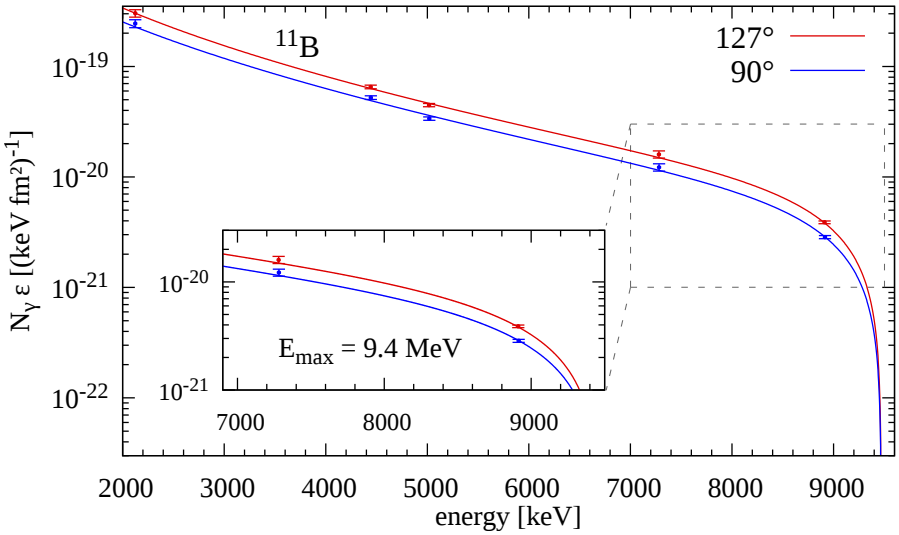

Figure 4.4: The logarithm of the product of absolute photon flux and FEP efficiencies of the HE measurement is scaled to well-known transitions of the calibration standard ^{11}B for the 127° (red) and 90° (blue) detectors.

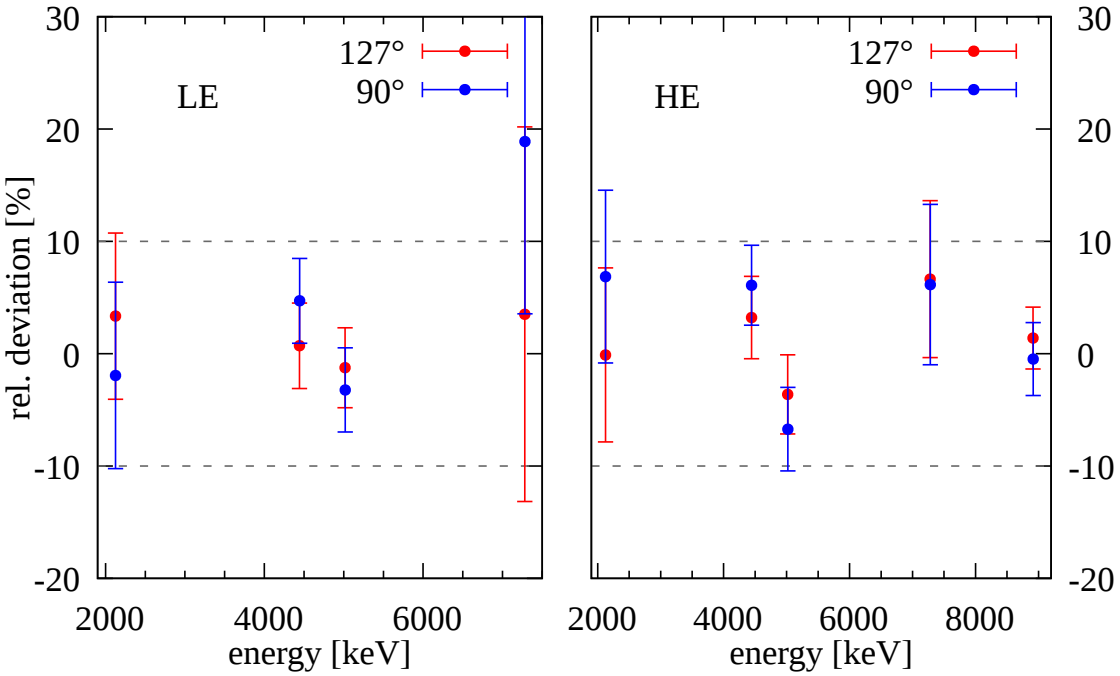

Figure 4.5: The relative deviations of the ^{11}B values from the determined, absolute product of absolute photon flux and FEP efficiencies of the LE (HE) measurement are depicted in the left (right) part of the figure for the 127° (red) and 90° (blue) detectors.

4.1.2 Multipolarity assignment

The distinction between dipole and quadrupole transitions was carried out by calculating the intensity ratio ω for all observed transitions using

$$\omega = \frac{A(90^\circ)}{A(127^\circ)} \cdot \frac{N_\gamma \epsilon(127^\circ)}{N_\gamma \epsilon(90^\circ)}. \tag{4.4}$$

The results were compared to the expected ratio between the two angular distributions $\frac{W(90^\circ)}{W(127^\circ)}$ (see Sec. 2.1). By taking into account the finite opening angles of the detectors, the ratios of the angular distributions equal $\omega = 0.74$ for a dipole transition and $\omega = 2.13$ for a quadrupole transition [53]. Peaks in the deexcitation spectra were assigned to a γ-ray transition if the relative uncertainties of the peak areas in both spectra are smaller than $\Delta A/A < 30\,\%$. In Fig. 4.6, all observed transitions, fulfilling this condition and not identified as background radiation, are illustrated.

In addition, transitions resulting completely from single-escape (SE) events were excluded. For this purpose, it was checked whether two transitions are energetically separated by 511 ± 1 keV and, afterwards, whether the lower one was observed in the HIγS spectra. When the transition did not appear in the HIγS spectra, it was identified as pure SE peak. Otherwise, only an SE contribution was assumed and the corresponding transition is included in the figure. The lowest (highest) horizontal line marks the expected angular ratio of a dipole (quadrupole) transition whereas the horizontal dashed line corresponds to an isotropic angular distribution.

States with low excitation energies can be fed by higher-lying states. This leads to a smeared-out angular distribution, i.e., the angular distribution is more isotropic, of the ground-state decay of the lower-lying state since different m substates were populated. Therefore, below 6.5 MeV (dashed vertical line), the intensity ratios extracted from the LE measurement were utilized for the multipolarity assignment and the HE data for higher-energetic ground-state transitions. In addition to the 10 % uncertainty resulting from the $N_\gamma \cdot \epsilon$ determination, the statistical uncertainties of the peak areas were taken into account.

The intensity ratios of the relevant ^{11}B transitions are shown as blue triangles. These agree with the expected values (cf. Table 4.1). Below 5 MeV, six transitions previously identified as $E2$ transitions of ^{64}Ni [73] were observed in this experiment (green circles in Fig. 4.6). It can be seen that most of the corresponding intensity ratios are below the expected angular-distribution ratio of a quadrupole transition. Therefore, it was concluded that these lower-lying states are highly fed as discussed above.

Besides already known inelastic decays of states of ^{64}Ni [73], further inelastic transitions

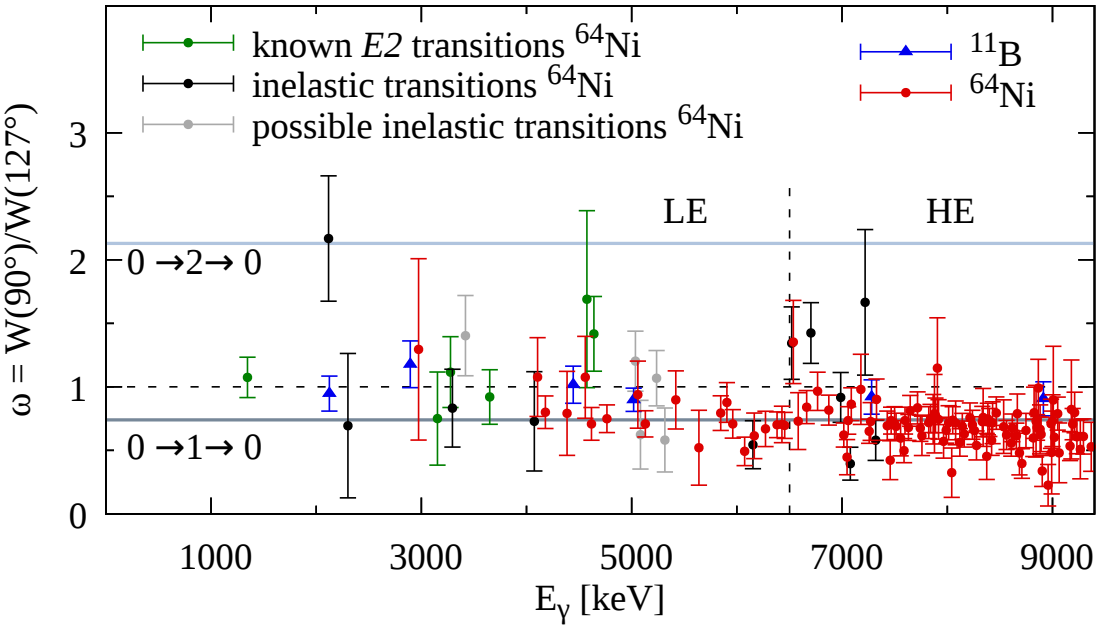

Figure 4.6: Calculated intensity ratios ω using the LE (HE) measurement are depicted on the left (right) side of the dashed vertical line at $E_\gamma = 6500\,\text{keV}$. Already known $E2$ and observed inelastic transitions are illustrated in green and black, respectively [73]. All other observed decays of ^{64}Ni are presented in red. Furthermore, transitions, which were identified as possible inelastic transitions due to their γ-ray energies, are shown in gray. The calculated intensity ratios of the relevant ^{11}B transitions are displayed as blue triangles. For details, see text

were identified. For this, the differences between all the transitions' energies were calculated and compared to the energy of the ground-state decay of the 2_1^+ state ($E(2_1^+) = 1346\,\text{keV}$). When the energy of a transition is $1346 \pm 1\,\text{keV}$ lower than that of any other transition and, additionally, this decay was not observed in the HIγS spectra, it was identified as inelastic transition. Not all energies, especially below 4 MeV and in the lower 5 MeV region, were covered in the HIγS experiment. Hence, the aforementioned energy condition was interpreted as a hint for an inelastic transition but not a clear proof for transitions with these energies (gray data points).

The red data points in Fig. 4.6 correspond to all other transitions of ^{64}Ni which were observed.

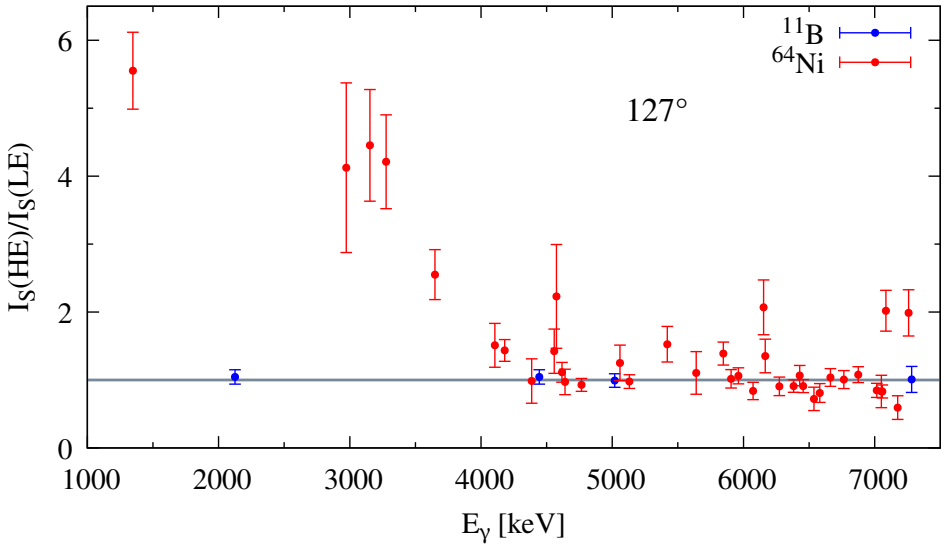

Figure 4.7: Calculated ratios of energy-integrated cross sections I_S deduced from the 127° detectors during the HE and LE measurements. Values corresponding to ^{64}Ni are shown in red and to ^{11}B in blue.

4.1.3 Feeding contributions

In bremsstrahlung experiments, many nuclear states are excited and can be investigated in one single measurement. This enables the simultaneous analysis of many states. However, lower-lying states can be fed by the higher-lying levels. To investigate feeding contributions, two bremsstrahlung measurements with different maximal photon energies (7.3 MeV (LE) and 9.4 MeV (HE)) were performed on ^{64}Ni. The ratios of the energy-integrated cross sections I_S (see Eq. (4.1)) deduced from the LE and HE measurements were calculated

$$\frac{I_S(\mathrm{HE})}{I_S(\mathrm{LE})} \begin{cases} \approx 1 & \text{no feeding contribution} \\ > 1 & \text{feeding contribution.} \end{cases} \tag{4.5}$$

Figure 4.7 shows the results for ground-state decays between both measurements utilizing the 127° detectors for ^{64}Ni (red) and ^{11}B (blue). The displayed uncertainties include the statistical uncertainties of the peak areas and the uncertainties introduced by the product of photon flux and efficiency as explained before. As stated in Eq. (4.5), $I_S(\mathrm{HE})/I_S(\mathrm{LE}) \approx 1$ means that the state is not fed whereas $I_S(\mathrm{HE})/I_S(\mathrm{LE}) > 1$ indicates a feeding contribution from a higher-lying level excited only in the HE measurement. As depicted in Fig. 4.7, the states of ^{64}Ni up to approximately 4.3 MeV are highly fed and levels above are not much influenced by feeding contributions.

4.2 Laser-Compton-Backscattering data of ^{64}Ni

4.2.1 Deconvolution of photon spectra

Recorded γ-ray spectra consist of events resulting from background radiation, incident photons of interest, and the corresponding detector response. For some analysis steps, a disentanglement of these contributions is crucial. Therefore, the method applied in this work is shortly introduced.
The deconvolution tool *Horst* (histogram original reconstruction spectrum tool) was used [74]. It is based on the fact that the recorded spectrum $\vec{s'}$ can be represented as superposition of the detector-response matrix $\boldsymbol{R}$ and the incoming γ-ray spectrum $\vec{s}$

$$\vec{s'} = \boldsymbol{R} \cdot \vec{s}. \tag{4.6}$$

To obtain the spectrum corresponding to photons of interest, the response matrix $\boldsymbol{R}$ is inverted and Eq. (4.6) is solved for $\vec{s}$. In Eq. (4.6), the influence of statistical fluctuations is neglected. These and systematic uncertainties resulting from the fitting procedure can be included by utilizing the Gaussian-propagation principle or the Monte-Carlo approach implemented in *Horst*. The latter method was used in this work. In each iteration, the input parameters, i.e., the recorded spectrum and the response matrix, are varied within their statistical uncertainties resulting in different solutions for $\vec{s}$. Besides returning each solution for $\vec{s}$, *Horst* calculates the mean and the standard deviation of all Monte-Carlo iterations for each energy bin. For more details, the reader is referred to Ref. [74].

4.2.2 Full-energy-peak efficiency

The full-energy-peak (FEP) efficiency up to 3.5 MeV was determined using source measurements (see Table 3.2). Because the activity of the ^{56}Co source is unknown, the corresponding values were scaled to the ^{152}Eu data. Furthermore, to take different locations of the sources in the beam line and different geometries into account, the ^{60}Co data were slightly (less than 10 %) adjusted to be in accordance with the ^{152}Eu data for determining the FEP efficiency for the beam-energy settings between 5.86 and 9.05 MeV. Figure 4.8 illustrates the ^{152}Eu and the adjusted ^{56,60}Co data valid for the energy runs between $E_{beam} = 5.86$ MeV and $E_{beam} = 9.05$ MeV as red, orange, and blue data points, respectively.
For gaining information about the FEP efficiencies up to 10 MeV, the *utr* tool was utilized [75] which is an implementation of the upper target room (utr) at HIγS based on GEANT4 [76–78]. The thickness of the implemented Cu and Pb filters in front of the detectors and

the distances between the detectors and the source were varied until the simulated efficiency data were in agreement with the source data (light-gray squares in Fig. 4.8). Afterwards, the best-fitting parameters were used to simulate an isotropic source that emits the γ rays out of a box which has the dimensions of the ^{64}Ni target. Furthermore, the ^{64}Ni target was simulated as well to take into account that, especially, low-energetic photons emitted from the target can interact with the material again before reaching the detector (dark-gray squares). As it can be seen in Fig. 4.8, this effect is strong for the detectors under $\theta = 90^{\circ}$ and comparably weak for the detector at backward angle. This means to reach one of the $\theta = 90^{\circ}$ detectors, the probability for an atomic interaction of the emitted photon within the target is much higher since the average amount of target material, which has to be passed, is higher for the $\theta = 90^{\circ}$ detectors. The simulated efficiencies were described by

$$\epsilon(E_\gamma) = m \cdot exp(-n \cdot E_\gamma) + o \cdot exp(-p \cdot E_\gamma) \tag{4.7}$$

and are depicted in light green in Fig. 4.8. The deviations between simulation values and fit function are smaller than 3 % for all HPGe detectors in the relevant energy range (between $E(2_1^+) = 1.35\,\text{MeV}$ and $10\,\text{MeV}$).

For the analysis of the NRF data, only one of the backward HPGe detectors (HPGe3 at $\theta, \phi = 135^{\circ}, 45^{\circ}$) was used since the crystal of the other backward detector is not positioned in the center of the dewar and no information about the alignment of the crystal and the target were given. Furthermore, the comparison of the FEP efficiencies obtained using the analog (genie) and the digital (MBS) data acquisition shows a deviation of more than 20 % for this detector. This is probably caused by a wrongly recorded effective measuring time of the genie system. Therefore, the inclusion of the data of this detector would increase the uncertainties and it was decided to neglected this detector for the analysis.

For the setup configuration, which was utilized for the measurements with beam energies below 5.86 MeV, only a ^{56}Co measurement was performed. However, as it is pointed out in Sec. 4.2.4, the knowledge about the relative FEP efficiencies is sufficient for these beam energies. In the case of $E_{beam} > 9.05\,\text{MeV}$, ^{152}Eu and ^{56}Co were used as radioactive sources, i.e., absolute FEP efficiencies were determined. The procedure for extrapolating the FEP efficiencies up to 10 MeV was always the same as described above.

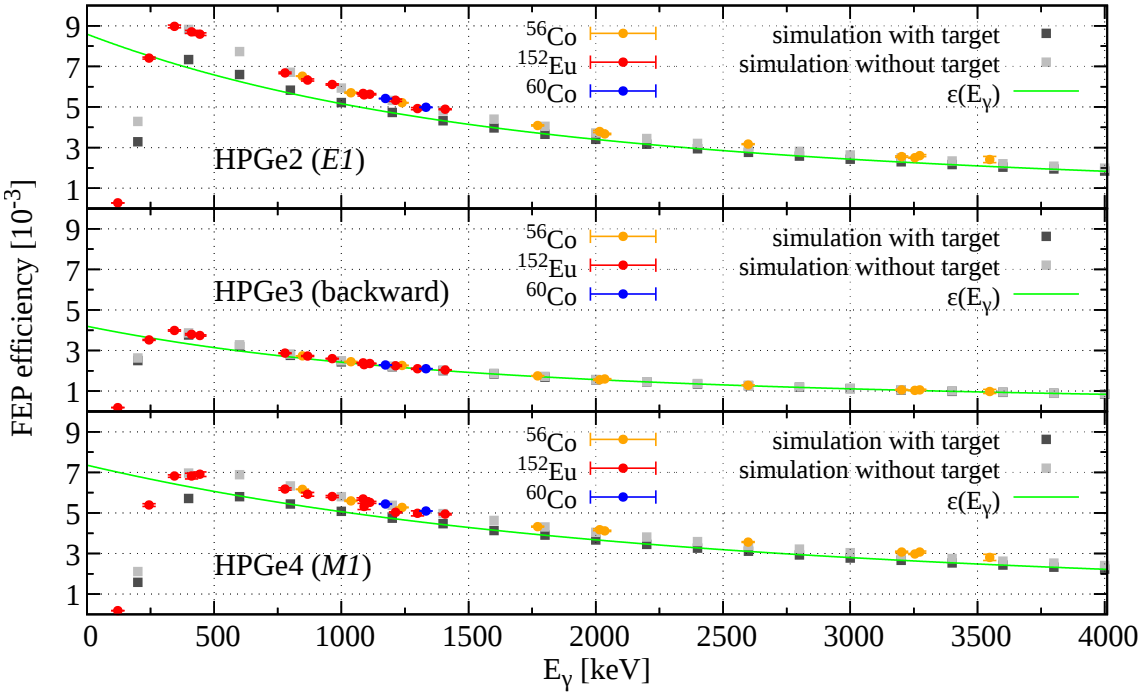

Figure 4.8: FEP efficiencies of the HPGe detectors are illustrated for the setup configuration of the experimental measurements between 5.86 and 9.05 MeV. The data of the ^{56,60}Co measurements (orange, blue) were scaled to the ^{152}Eu (red) values to obtain a good description of the efficiencies' shapes. Simulations were performed to reproduce the source data (light gray). The corresponding filter thicknesses and distances were applied to perform simulations including the target (dark gray). The fit functions according to Eq. (4.7) are shown in light green.

Table 4.2: The angular distributions of pure $E1$, $M1$, and $E2$ transitions are given for the positions θ, ϕ of the HPGe detectors.

	θ, ϕ	$W_{E1}(\theta, \phi)$	$W_{M1}(\theta, \phi)$	$W_{E2}(\theta, \phi)$
vertical detector ($E1$)	90°, 90°	1.5	0	0
backward detector	135°, 45°	9/8	9/8	5/8
horizontal detector ($M1$)	90°, 0°	0	1.5	1.5

4.2.3 Radiation-character assignment

At HIγS, the radiation character of a transition is assigned by determining the direction of movement of the deexciting photon relative to the polarization plane of the incident photon. The angular distributions $W_{\Pi L}(\theta, \phi)$ of $E1$, $M1$, and $E2$ transitions for the positions of the HPGe detectors are given in Table 4.2. To determine the radiation character, the analyzing power Σ_{hv} is defined as [79]:

$$\Sigma_{hv} = \frac{W_{\Pi L}(90°, 0°) - W_{\Pi L}(90°, 90°)}{W_{\Pi L}(90°, 0°) + W_{\Pi L}(90°, 90°)} = \begin{cases} +1 & M1 \text{ and } E2 \text{ transitions} \\ -1 & E1 \text{ (and } M2\text{) transitions.} \end{cases} \tag{4.8}$$

The experimentally accessible quantity is the so-called asymmetry ϵ_{hv} which corrects the analyzing power for the finite opening angles of the detectors and the degree of polarization of the incoming photon beam. These corrections are included in the factor q in:

$$\epsilon_{hv} = q \cdot \Sigma_{hv} = \frac{A_{\text{corr}}(90°, 0°) - A_{\text{corr}}(90°, 90°)}{A_{\text{corr}}(90°, 0°) + A_{\text{corr}}(90°, 90°)}. \tag{4.9}$$

Here, A_{corr} denotes the peak area corrected for the effective measuring time and FEP efficiency of the corresponding detector. For the assignment, the calculated asymmetry of each transition was compared to simulated asymmetries which include the opening-angle correction. By varying the distances between detector and target, the opening angle and, therefore, the expected asymmetry change. Three different setup configurations were utilized during the ^{64}Ni experiment indicated by the vertical, gray dashed lines in Fig. 4.9.
The asymmetries ϵ_{hv} for all observed transitions are illustrated in Fig. 4.9. A firm (tentative) radiation-character assignment was performed, when the calculated asymmetry ϵ_{hv} agrees within 2σ (3σ) with only one of the simulated asymmetry values (horizontal lines in Fig. 4.9). For that purpose, an uncertainty of 10 % was assumed for the simulated asymmetries to take into account the different positions and geometries of sources and the ^{64}Ni targets. In Sec. 4.2.4, the reason for the choice of an uncertainty of 10 % is given. In orange (blue), all

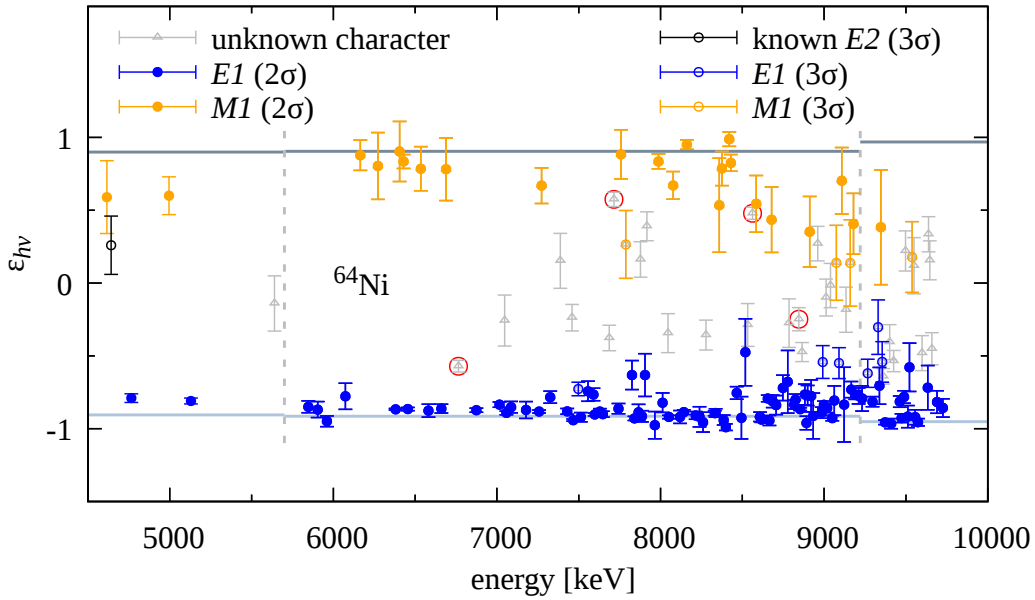

Figure 4.9: The asymmetry values $\epsilon_{h\upsilon}$ of all transitions of ^{64}Ni observed at HIγS are illustrated. In the case of a firmly (tentatively) identified $E1$ transition, the corresponding data point is illustrated as full (empty) blue circle. The same holds for $M1$ transitions but these are indicated in orange. When no radiation-character assignment was possible, the $\epsilon_{h\upsilon}$ value is shown as gray empty triangle. One known $E2$ transition [73] was observed at 4640 keV whose multipolarity was determined using the bremsstrahlung data and the investigation of the radiation character at HIγS confirms the $E2$ character within 3σ (black empty circle). The radiation characters of the transitions highlighted in red were determined by using the energy-integrated cross sections. Three different setup configurations were used during the experiment, resulting in three different simulated asymmetry pairs (solid horizontal lines) for $M1$ and $E1$ transitions. The energies at which the setup was modified are indicated by dashed vertical lines.

identified $M1$ ($E1$) transitions are indicated. Open circles correspond to transitions which are only tentatively characterized. For transitions corresponding to asymmetries $\epsilon_{h\upsilon}$ marked in gray, a radiation character could not be assigned using the aforementioned conditions.
As indicated in Table 4.2 and by the ground-state decay of a known 2^+ state at $E_x = 4641$ keV (black empty circle) [73], a similar asymmetry $\epsilon_{h\upsilon}$ is expected for $M1$ and $E2$ transitions. When the multipolarity was already known from the bremsstrahlung measurement, the transition was considered as fully characterized. When the multipolarity was not firmly assigned, the transition was further analyzed by using the deexcitation spectra recorded by the backward HPGe detector of the HIγS experiment as well. For that purpose, the asymmetries ϵ_{hb} and $\epsilon_{\upsilon b}$ were defined analogously to Eq. (4.9) [80]. The results for the affected transitions, and the simulated asymmetries are illustrated in Figs. 4.10 and 4.11 for transitions observed

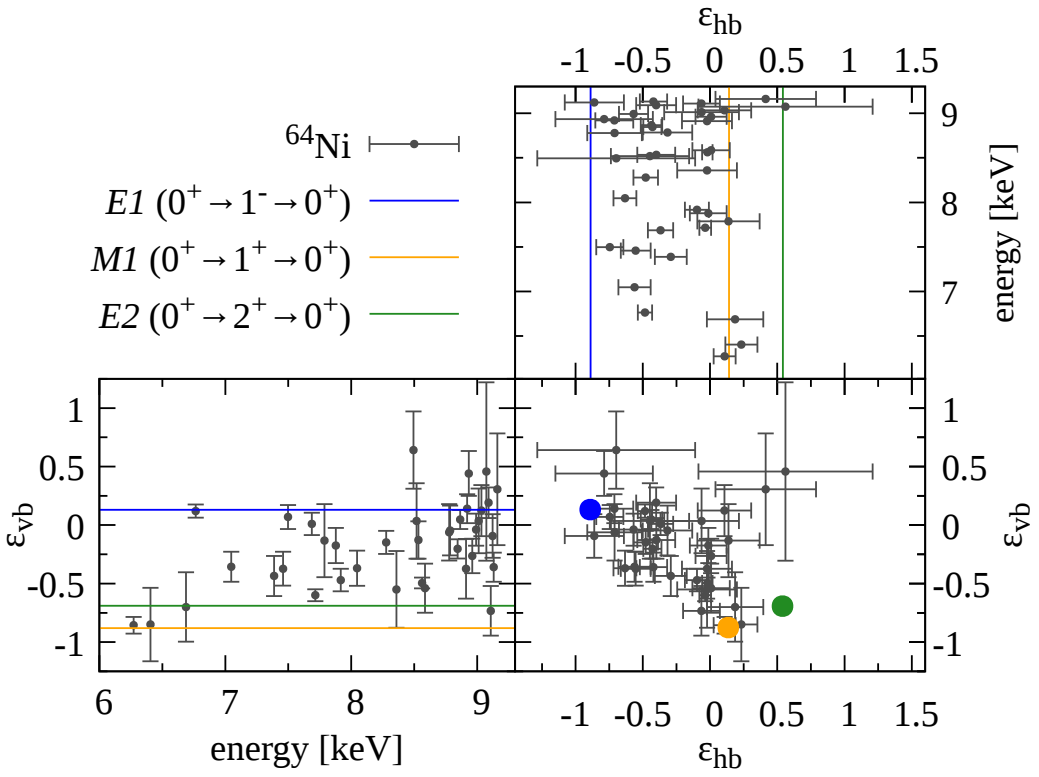

Figure 4.10: The calculated asymmetries ϵ_{hb} (upper right) and ϵ_{vb} (lower left) in dependence on the energy are illustrated for transitions investigated in the measurements at beam energies between 5.86 and 9.05 MeV. In the lower right, the correlation of both asymmetries is shown. Additionally, the simulated values for pure $E1$, $M1$, and $E2$ transitions are depicted in blue, orange, and green, respectively. The asymmetries were only calculated if the transition was not firmly characterized in the analysis of the bremsstrahlung data and the asymmetry ϵ_{hv}. For details, see text.

in the measurements between 5.86 and 9.05 MeV and between 9.3 and 9.6 MeV, respectively. For a firm (tentative) assignment using the backward detector the calculated ϵ_{hb} value had to agree within its 2σ (3σ) range with the corresponding simulated asymmetry and, at the same time, the simulated ϵ_{vb} value had to be within the 2σ (3σ) range of the calculated one.
The assigned spin-parity quantum numbers corresponding to the observed ground-state decays are summarized in Table I in the manuscript in Chapter 5. In addition, the characterizations of four transitions due to their energy-integrated cross sections are described. These are highlighted in red in Fig. 4.9.

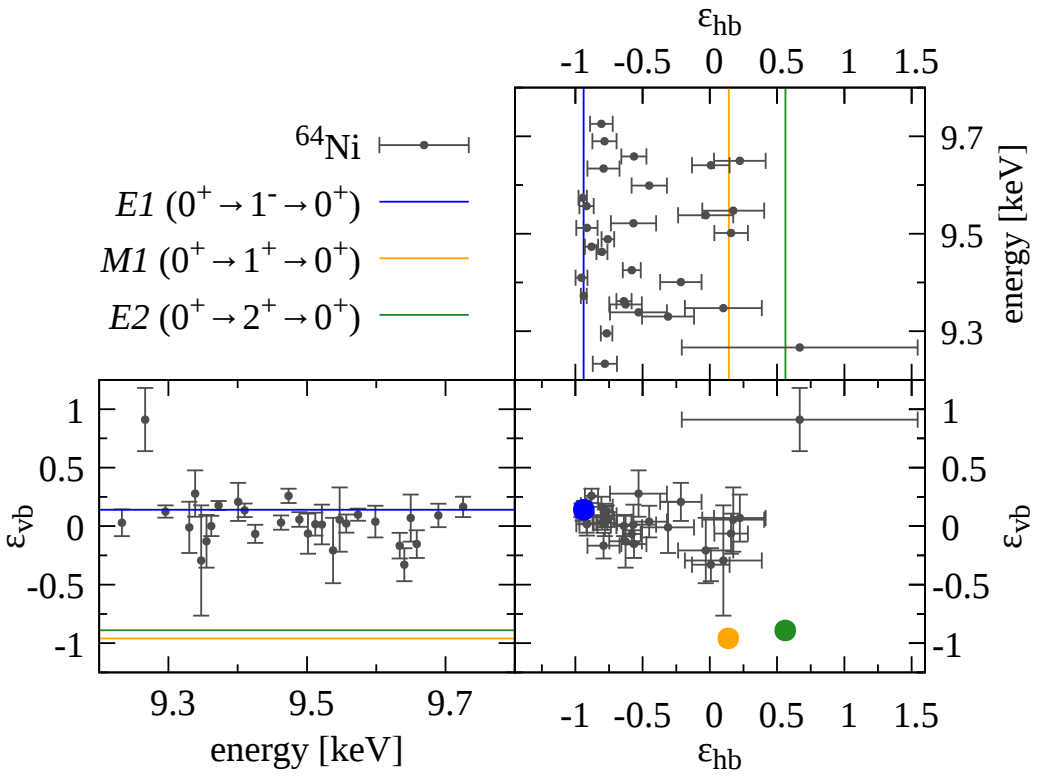

Figure 4.11: The calculated asymmetries ϵ_{hb} (upper right) and ϵ_{vb} (lower left) in dependence on the energy are illustrated for transitions investigated in the measurements at beam energies of 9.3 and 9.6 MeV. In the lower right, the correlation of both asymmetries is shown. Additionally, the simulated values for pure $E1$, $M1$, and $E2$ transitions are depicted in blue, orange, and green, respectively.

4.2.4 Photon-flux determination

The general principle of the photon-flux determination at HIγS is comparable to that of the bremsstrahlung experiment, i.e., the photon-flux distribution has to be determined which is, afterwards, scaled to known transitions.
For the determination of the photon flux' shape, a 123 % HPGe detector (0°detector) is positioned in the beam detecting the incident photon spectrum before each measurement with a different beam-energy setting. First, background due to cosmic radiation has to be subtracted from the recorded spectra. For this purpose, the shape of this background radiation above 4 MeV was determined by using the spectrum recorded during a ^{56}Co source measurement at the γ^3 setup for eight hours and it is well described by

$$\mathrm{bg}(E_\gamma) = a \cdot \exp(-b \cdot E_\gamma) + c \cdot \exp(-d \cdot E_\gamma) + e \cdot \exp(-f \cdot E_\gamma) + g. \tag{4.10}$$

It was scaled to and, afterwards, subtracted from the experimental ^{64}Ni spectra. The background-corrected spectrum (gray histogram in Fig. 4.12) was deconvoluted using the code *Horst*. One exemplary deconvoluted spectrum is illustrated in Fig. 4.12 as black histogram. As described before, the Monte-Carlo approach was utilized to estimate the uncertainties (cf. Sec. 4.2.1). All resulting distributions were individually fitted using

$$N_\gamma(E_\gamma) = a \cdot \frac{exp\left(\frac{-(E_\gamma - m)^2}{2s^2}\right)}{\sqrt{2\pi s^2}} \cdot \left(1 + erf\left(\frac{b \cdot (E_\gamma - m)}{\sqrt{2} \cdot s}\right)\right). \tag{4.11}$$

The parameters m and s can be interpreted as a measure for the centroid energy and the width of the distribution, respectively. The b parameter describes the skewed, high-energy side of the distribution. This procedure only gives information about the photon-flux distribution and not about the true number of photons impinging on the ^{64}Ni target due to the used copper absorbers in front of the 0° detector for attenuating the beam.

Because of the quasimonoenergetic γ-ray beam at HIγS, it is not easily feasible to use a calibration target for the absolute photon-flux determination. Hence, transitions of the nucleus of interest itself, which have been investigated in, e.g., bremsstrahlung experiments, serve as calibration points. As stated in Sec. 4.1.2 and Sec. 4.1.3, some transitions are contaminated by SE events or feeding contributions in the bremsstrahlung data but not in the Laser-Compton-Backscattering (LCB) experiment. Therefore, these transitions have to be identified beforehand and cannot be used for the photon-flux scaling. For strong transitions ($I_S > 2$ keV fm^2

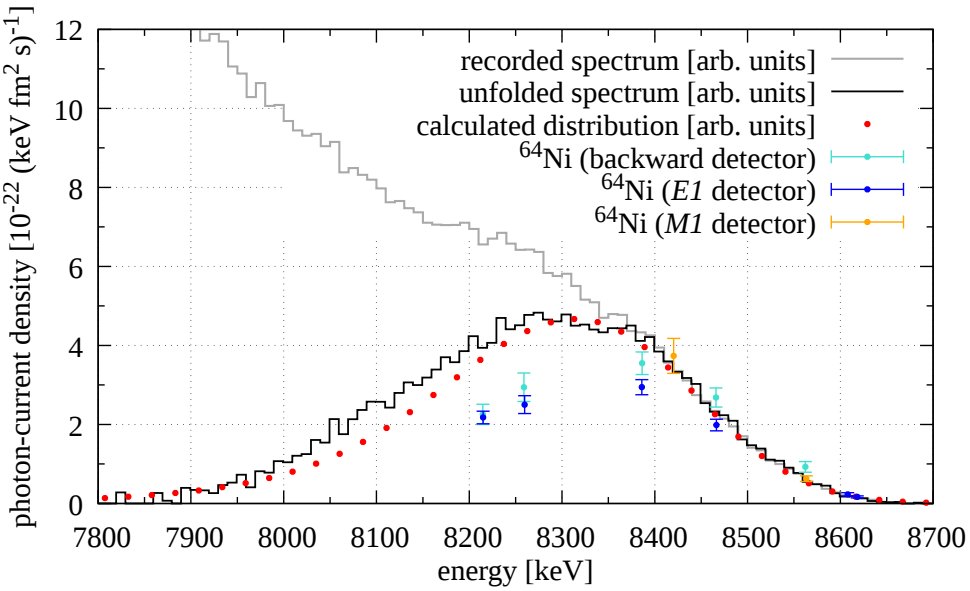

Figure 4.12: The energy distribution of the photons recorded by the beam monitor at a beam energy of $E_{beam} = 8.3$ MeV is depicted in gray and one exemplary deconvolution result in black. In addition, the calculated photon distribution using the accelerator settings is shown in red [81, 82]. All data are scaled to strong transitions of ^{64}Ni at the high-energy side of the distribution recorded by the backward (turquoise), $E1$ (blue), and $M1$ (orange) detectors.

and $\Delta I_S/I_S < 10\,\%$), the photon-current densities were calculated according to

$$N_\gamma = \frac{A}{N_T \cdot I_S(E_x) \cdot \epsilon(E_\gamma) \cdot W_{\Pi L}(\theta, \phi) \cdot \tau}. \tag{4.12}$$

To be independent from different γ^3 HPGe detectors, an additional correction was introduced to account for the different effective measuring times τ. Therefore, N_γ is the photon-current density in this section. For the determination of the uncertainties of the experimental N_γ values, only statistical uncertainties from the γELBE (ΔI_S) and HIγS (ΔA) experiments were taken into account. The deconvoluted spectra were scaled to extracted values of transitions of ^{64}Ni. In Fig. 4.12, the recorded spectrum at a beam energy of $E_{beam} = 8.3$ MeV (gray) and the high-energy side of the deconvoluted spectrum of one Monte-Carlo iteration determined by the code *Horst* (black) were scaled to transitions of ^{64}Ni recorded by the backward detector (turquoise).

As it can be noted, the photon-flux distribution impinging on the ^{64}Ni target is more narrow than the deconvoluted spectrum of the 0° detector. This effect occurred for all beam energies between 5.86 and 9.05 MeV. For lower and higher beam energies not enough ^{64}Ni transitions were observed in the bremsstrahlung data to investigate this effect. To exclude that this dis-

crepancy results due to problems concerning the 0° detector or the deconvolution procedure, the photon-flux distribution was calculated by using the settings of the accelerator as well (red data points in Fig. 4.12) [81, 82]. A good agreement between this calculation and the *Horst* result can be noticed. This is an additional indication that the photon flux impinging on the ^{64}Ni target is different than the generated one.

As possible explanation it is suggested that the target and the photon beam were not well aligned during the experiment. The beam and the target had approximately the same diameter. Since the beam has a spatial energy distribution (higher energies are in the center and lower energies at the edges of the circular beam), a not perfect alignment of target and beam would lead to a cutting off of the low-energy tail of the photon-flux distribution.

One additional result of this effect is illustrated in Fig. 4.13. During some measurements, an additional ^{64}Ni target with a diameter of only 0.8 cm was positioned in the beam line at a parasitic setup consisting of three HPGe detectors. This means that, actually, the same photon flux had to impinge on both ^{64}Ni targets. The direct comparison of the deexcitation spectra recorded by the $E1$ HPGe detectors ($\theta, \phi = 90°, 90°$) of both setups is shown in Fig. 4.13. Whereas the transition at approximately 8050 keV appeared more strongly in the spectra recorded at the γ^3 setup with the 1.9 cm diameter target (blue histogram), the strengths of all transitions above 8200 keV are comparable for both targets. This indicates that less low-energy photons impinged on the target with the smaller diameter (red) than on the other, i.e., different energy distributions can be observed.

Indeed, the beam pipe and the ^{64}Ni target were aligned relative to the incoming beam before the experiment had started. However, the target was unmounted between the 5.63 and the 5.86 MeV experimental runs to perform source measurements. It is possible that the target was not perfectly aligned when it was remounted which might result in this disagreement.

Because many strong transitions are present between 6 and 9 MeV in the ^{64}Ni data, it was decided to use these data points not only for the determination of the absolute photon flux but also for extracting the photon-flux distribution. For this purpose, some assumptions had to be made: first, the effect impacts all beam-energy settings to the same degree (if the target and detectors were not moved) which implies that functional dependencies using all measurements can be set up. Second, the high-energy side is not affected and is the same as recorded by the beam monitor, i.e., the b parameter of Eq. (4.11) extracted from the *Horst* result can be used to describe the high-energy side of the distribution impinging on the target. These assumptions would be justified if the discrepancy occurred due to a misalignment of the target.

For obtaining the functional dependencies, Eq. (4.11) was fitted to the ^{64}Ni data points us-

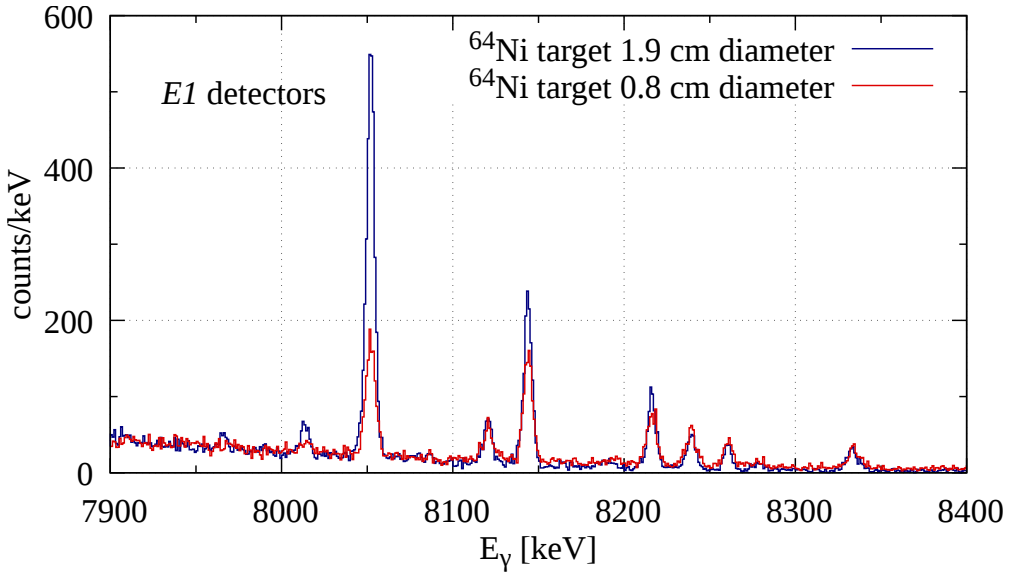

Figure 4.13: The deexcitation spectra recorded by the $E1$ detectors at the γ^3 setup (blue) and the parasitic setup (red). Whereas a ^{64}Ni target with a diameter of 1.9 cm (same diameter as the beam) was positioned at the γ^3 setup, a ^{64}Ni target with a diameter of only 0.8 cm was placed at the parasitic setup.

ing the b_{Horst} parameter, extracted from the deconvoluted beam-monitor spectra, for each Monte-Carlo iteration deduced by the code *Horst*. The results for all beam energies are displayed in the upper part of Fig. 4.14 for one exemplary Monte-Carlo iteration. For three beam-energy settings, no fit functions are illustrated since these were not determinable due to the low number of ^{64}Ni data points. The distributions impinging on the ^{64}Ni target deduced from six beam-energy settings (solid curves in the upper part of Fig. 4.14) are well described by the ^{64}Ni data points and the b_{Horst} parameter. The corresponding fit parameters s and m (cf. Eq. (4.11)) were utilized for determining systematic dependencies with respect to the parameters of the deconvolution results s_{Horst} and m_{Horst}. Linear dependencies were assumed for both parameters and are shown in the lower part of Fig. 4.14. In this way, the photon-flux distributions for all beam energies between 5.86 and 9.05 MeV were obtained.

As it was said, the target was moved between the measurements with $E_{\text{beam}} = 5.63$ MeV and $E_{\text{beam}} = 5.86$ MeV and ^{64}Ni has too few transitions for applying the same procedure for the low-energy setup configuration. Furthermore, the pencil-like ^{64}Ni target mentioned before was positioned at the γ^3 setup for the beam-energy settings $E_{\text{beam}} > 9.05$ MeV (diameter of 0.8 cm and length of 9 mm). Because of the smaller target diameter compared to the beam diameter, it was expected that the aforementioned effect would be even more pronounced (cf.

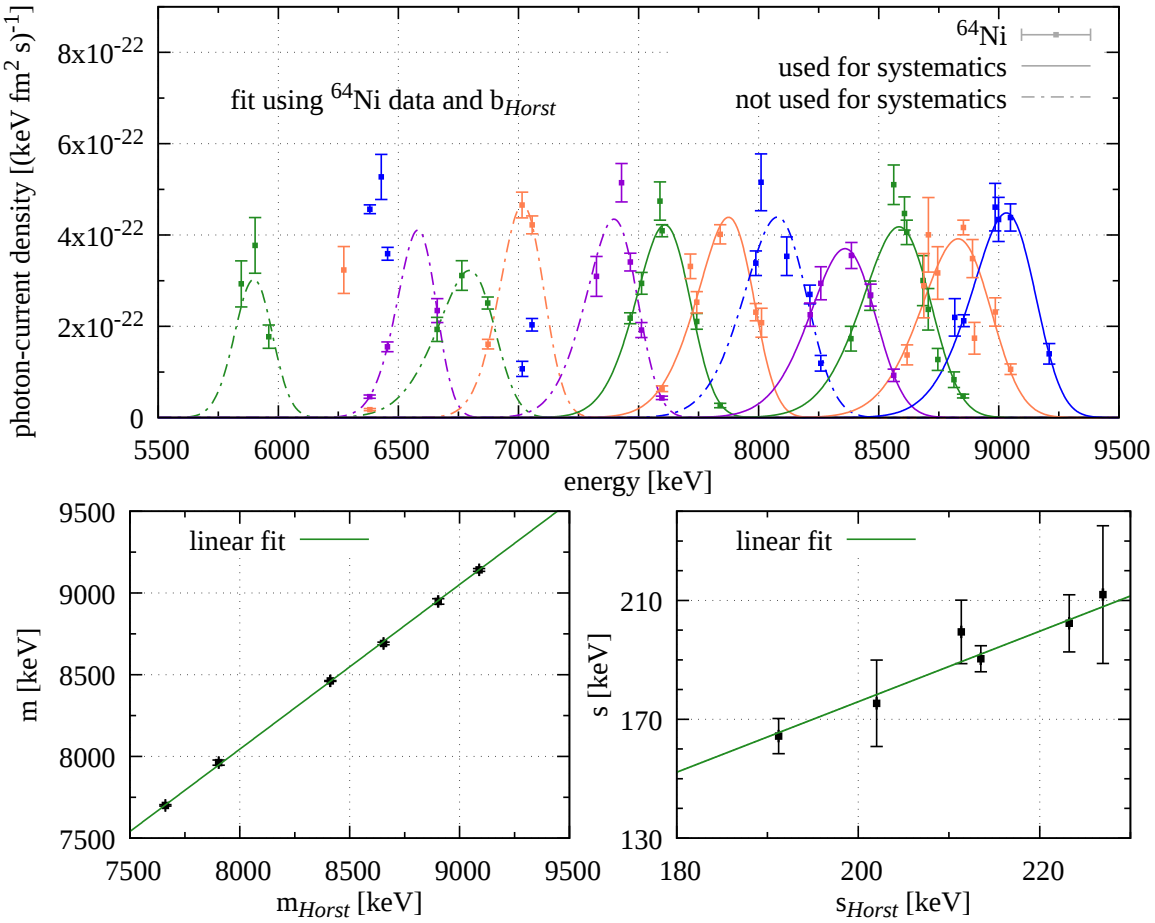

Figure 4.14: Upper panel: the illustrated photon-flux distributions in dependence on the photon energy were generated by fixing the high-energy side using the b_{Horst} parameter determined by the deconvolution of the photon spectra and strong transitions of ^{64}Ni. The different colors serve for a better distinction between the various beam energies. If the shape is depicted by a solid curve, the corresponding fit results were used to set up linear dependencies on the m_{Horst} (lower left figure) and s_{Horst} (lower right figure) parameters extracted from the deconvolution. For more details, see text.

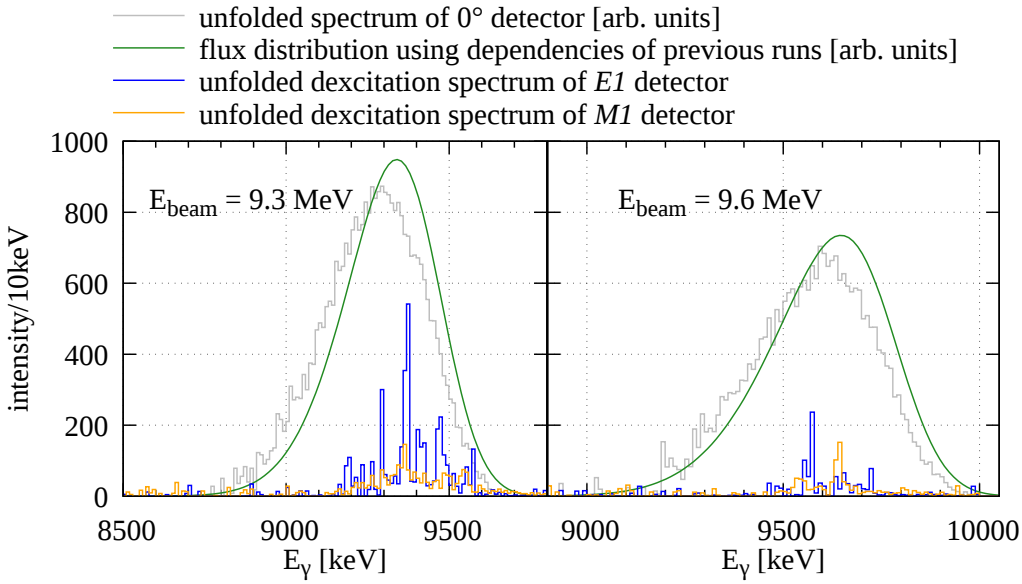

Figure 4.15: One exemplary Monte-Carlo iteration result of the deconvolution of the deexcitation spectra recorded by the $E1$ (blue) and $M1$ (orange) detector for the beam energies of 9.3 MeV (left panel) and 9.6 MeV (right panel). For these two measurements, the pencil-like target was utilized. The deconvoluted photon spectra of the 0° detector (gray histogram) and the photon distribution deduced by using the systematic dependencies obtained from measurements with the target with the larger diameter (green curves) are illustrated.

Fig. 4.13). This is supported by comparing the deconvoluted deexcitation spectra of the $M1$ (orange) and $E1$ (blue) detectors recorded during the 9.3 and 9.6 MeV measurements with the photon distributions using the deconvoluted spectra of the 0° detector for the respective beam energy (gray histograms) and the systematic dependencies obtained for the lower-energy settings (green curves) (see Fig. 4.15). For these two runs, the shape of the photon flux could not be reconstructed using known transitions of ^{64}Ni from the bremsstrahlung measurement since the maximal photon energy of the HE experiment was at 9.4 MeV and the energetically highest-lying transition was observed at 9.37 MeV. Hence, not enough transitions were known in the excitation-energy regions of the HIγS measurements at 9.3 and 9.6 MeV.

After the determination of the energy distributions of the photons, the absolute photon-current densities impinging on the target were deduced using two absolute-scaling techniques. On the one hand, each beam profile was individually scaled to the corresponding ^{64}Ni data (dashed fit functions in Fig. 4.17). When only very few ^{64}Ni data points are available, this method introduces large uncertainties.
On the other hand, a global-scaling procedure (solid curves) was applied [83]. For that pur-

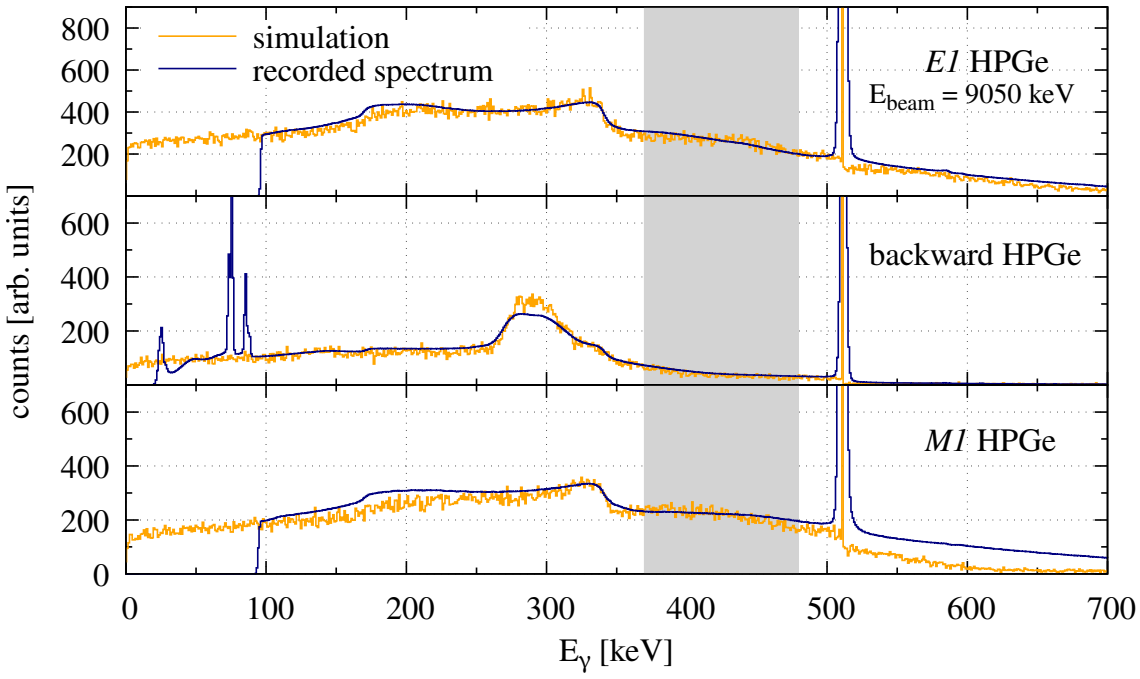

Figure 4.16: The simulated low-energy background (yellow) was scaled to the corresponding recorded one (blue) for each HPGe detector individually. The energy region between 370 and 480 keV was used for this purpose (gray-shaded area). The results for the beam energy at 9.05 MeV are shown.

pose, the normalized photon distributions were scaled relatively to each other by taking advantage of the fact that the low-energy background is proportional to the number of impinging photons on the target. Therefore, this background was simulated for each beam energy using 10^9 photons incident on the ^{64}Ni target and, afterwards, scattered in the HPGe detectors of the γ^3 setup. The simulated low-energy backgrounds (yellow histograms in Fig. 4.16) were scaled to the experimental spectra (blue) to obtain the total number of photons impinging on the ^{64}Ni target in the individual experimental runs. In Fig. 4.16, the results for a beam energy of 9.05 MeV are depicted. The energy region between 370 and 480 keV (gray-shaded area) was chosen in this work. At these low energies, the influence of photons reabsorbed within the target before reaching the detectors has to be taken into account. This effect is most significant for the detectors at $\theta = 90°$ (cf. Fig. 4.8). Therefore, only the deexcitation spectra of the backward detector were utilized for this purpose. Then, the relatively-scaled distributions were absolutely scaled to all photon-current densities determined from the ^{64}Ni data points simultaneously.

By simulating the low-energy background, energy dependencies of the atomic interactions are taken into account. In this work, it was decided not to use the 511 keV peak for rela-

tive scaling as it was done in Ref. [59], since it was observed that, above a certain beam energy, the number of 511 keV events slowly decreased with increasing γ-ray energy in the simulation. This is, with respect to the energy dependency of the cross section of pair production, counter intuitive. Possibly, this effect resulted due to the fact that with increasing γ-ray energy the positrons, generated in the pair production, have higher energies. Therefore, the number of positrons, which are not sufficiently slowed down to annihilate in the target material, increases. This implies that an increasing fraction of pair-annihilation processes occurred behind the γ^3 setup and the produced 511 keV photons were not recorded by the HPGe detectors. The position of the annihilation process is dependent on the air pressure. Since this was not recorded during the measurements, it was decided to use an energetically lower-lying region for the relative scaling.
In Fig. 4.17, one exemplary set of absolute photon-current densities, obtained by using transitions of ^{64}Ni recorded by the backward HPGe detector, is illustrated. The results of the global-scaling (individual-scaling) procedure are indicated by solid (dashed) curves. The agreement between both methods is good, when sufficient ^{64}Ni data points are present. Again, the different colors were used for a better distinction between the beam energies.
In the lower part of the figure, the same photon-current densities are depicted. However, ^{64}Ni data points determined by using the $E1$ (open circles) and the $M1$ (full circles) HPGe detectors are given. A mean deviation of +5 % (−5 %) was observed between the ^{64}Ni data of the $M1$ ($E1$) detector and the photon-current densities obtained using the backward detector. These differences appear due to a disagreement of the products of the detection efficiency and the angular distribution of the $E1$ and the $M1$ detectors with respect to the backward detector. Only $M1$ ($E1$) transitions of ^{64}Ni could be sufficiently accurately investigated in the deexcitation spectra recorded by the $M1$ ($E1$) detector to be used for the determination of the photon-current densities. Hence, the correction factor of +5 % (−5 %) can only be applied to the product of $W_{M1}(90°, 0°) \cdot \epsilon(90°, 0°)$ ($W_{E1}(90°, 90°) \cdot \epsilon(90°, 90°)$). This means that no correction factor could be determined for the other radiation character.

4.2.5 Energy-integrated cross sections

The energy-integrated cross sections I_S calculated for the analyzed transitions of ^{64}Ni are listed in Table I in Chapter 5. In general, the values determined in the bremsstrahlung experiment were used due to the more robust determination of the absolute photon flux. However, in some cases, the transition was only observed in the HIγS data or it was assumed that the corresponding peak area is contaminated in the γELBE spectra. Then, the energy-integrated cross section is presented which was extracted from the HIγS experiment. The procedure is

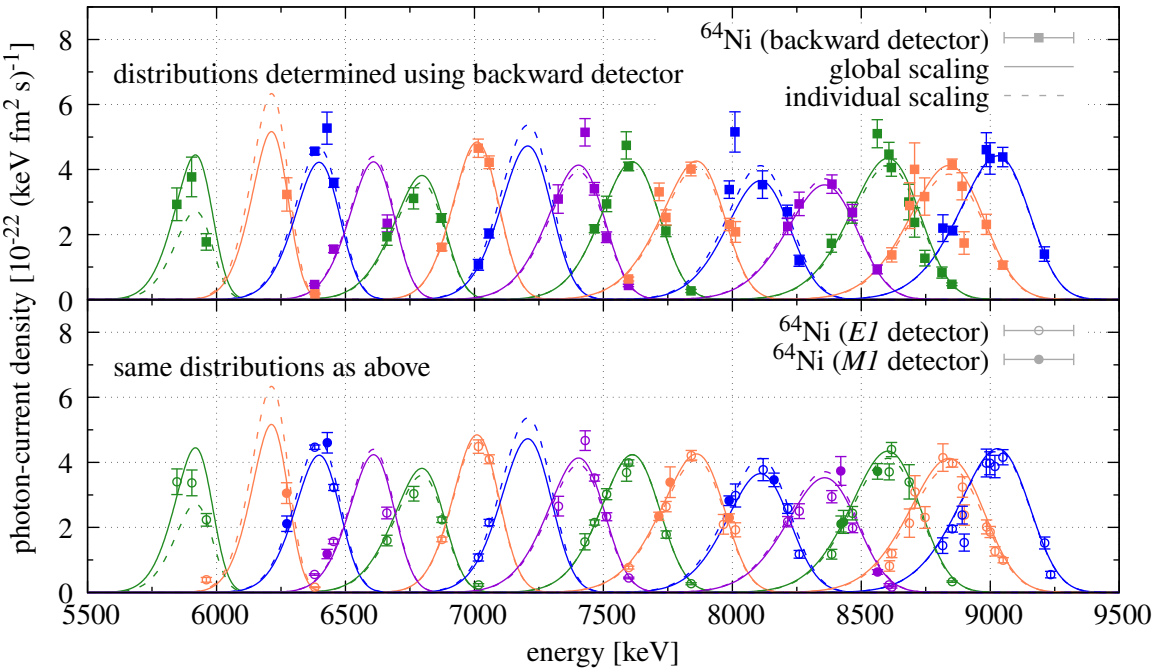

Figure 4.17: One exemplary set of the absolute photon-current densities obtained for all beam energies by using the backward detector is displayed. The results of the global (individual) scaling of the distributions to the ^{64}Ni data recorded by the backward detector are illustrated by the solid (dashed) fit functions. The different colors were utilized to distinguish the data of the different beam energies. The lower part of the figure shows the same photon-current densities but ^{64}Ni data points calculated using the $E1$ and $M1$ HPGe detectors.

described in the manuscript as well and the affected transitions are marked in the table.

4.2.6 Average cross sections

The results of state-to-state analyses are used to investigate individual transitions and give a first impression of the fragmentation of the low-lying dipole strength. Nevertheless, it fails in giving a total picture of the photoresponse. For that purpose, the total photoabsorption cross section σ_γ is a good measure. It includes the complete elastic-decay channel $\sigma_{\gamma\gamma}$ and an estimate for the inelastic decay channel $\sigma_{\gamma\gamma'}$.

Elastic cross section

In general, the average elastic cross section $\sigma_{\gamma\gamma}$ can be calculated from the HIγS data by summing all energy-integrated cross sections $I_{S,x\to0}$ corresponding to ground-state decays of the directly-excited states x by the quasimonoenergetic photon beam. To include also weak transitions, Eq. (4.1) was modified and used as approximation for the elastic-decay channel. The peak area of one individual transition is replaced by the total number of recorded events A(tot) in an energy interval δE, and the photon-current density by the integral over the same energy interval δE to obtain $N_{\gamma,\mathrm{tot}}$ yielding [84, 85]

$$\sigma_{\gamma\gamma} = \frac{\sum_x I_{S,x\to0}}{\delta E} \sim \frac{A(\mathrm{tot})}{N_T \cdot N_{\gamma,\mathrm{tot}} \cdot \overline{\epsilon(E_\gamma)} \cdot \tau \cdot W_{\Pi L}(\theta,\phi)}. \tag{4.13}$$

Moreover, $\overline{\epsilon(E_\gamma)}$ equals the average FEP efficiency and τ the effective measuring time of the detector.

To obtain A(tot), the recorded deexcitation spectra of ^{64}Ni were corrected for the cosmic background and deconvoluted using the code *Horst*. For this analysis step, the same procedures were applied as for the deconvolution of the photon spectra recorded by the 0° detector (cf. Sec. 4.2.1). The results of one Monte-Carlo iteration for the beam-energy settings of 5.86 MeV (left part) and 8.05 MeV (right part) are shown in Fig. 4.18. For a better visualization, the 5.86 MeV spectra were multiplied by 10. One of the deduced photon distributions indicates the excitation region for each beam energy in arbitrary units (gray). The unfolded deexcitation spectra recorded by the $E1$, $M1$, and backward detectors are depicted as blue, orange, and red histograms, respectively. Whereas almost no events occur at energies below the excitation-energy region in the unfolded deexcitation spectra of the 8.05 MeV measurement, an increase of the number of events for lower energies is present in the 5.86 MeV data.

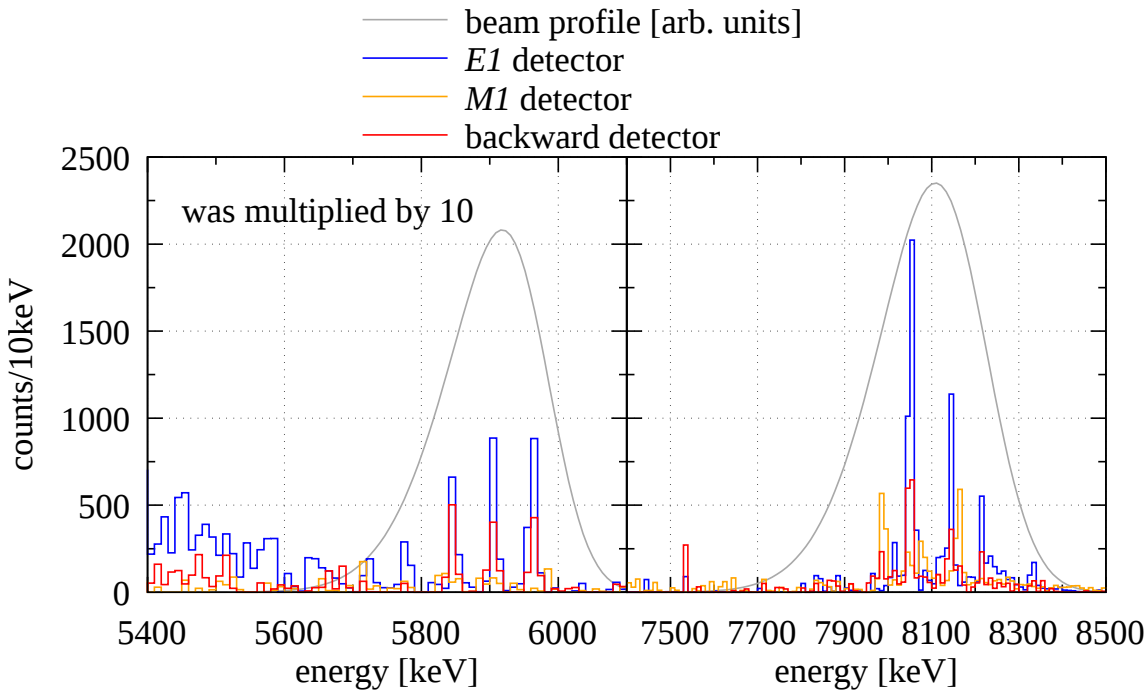

Figure 4.18: The left (right) part of the figure shows the deconvoluted deexcitation spectra recorded by the $E1$, $M1$, and backward detector in blue, orange, and red, respectively, for a beam energy of 5.86 MeV (8.05 MeV). The 5.86 MeV spectra were multiplied by 10 for better visualization. The excitation region is indicated by the photon distribution in arbitrary units.

During the measurements at 5.86 and 6.15 MeV, the beam pipe was not well evacuated resulting in an additional background contribution at energies below the excitation-energy region due to low-angle scattering of the photons off air. Since this effect is dependent on the air pressure in the beam line, which was not documented during the experiment, it cannot be reconstructed using simulations. Therefore, no average elastic cross section could be determined for $E_{\mathrm{beam}} < 6.38\,\mathrm{MeV}$. Before the measurement at $E_{\mathrm{beam}} = 6.38\,\mathrm{MeV}$ was conducted, the vacuum at the γ^3 setup has been improved. Hence, much better deconvolution results were obtained for the following measurements. Because the absolute photon-current density is needed to calculate average elastic cross sections $\sigma_{\gamma\gamma}$ according to Eq. (4.13), it could only be deduced up to 9.05 MeV.

Because of the finite opening angles of the detectors, each deexcitation spectrum consists of a superposition of $M1$ and $E1$ contributions. $E2$ contributions were excluded since these are rather unlikely and no resolved $E2$ transition was identified in the state-to-state analysis above 5 MeV. Therefore, a linear system of equations was set up according to

$$\begin{aligned} A(90^\circ, 90^\circ) &= \frac{1}{N_T \cdot N_{\gamma,\mathrm{tot}} \cdot \overline{\epsilon_{\mathrm{HPGe2}}} \cdot \tau_{\mathrm{HPGe2}}} \left(\frac{\sigma_{\gamma\gamma}(E1)}{f_2 \cdot W_{E1}(90^\circ, 90^\circ)} + \frac{\sigma_{\gamma\gamma}(M1)}{W_{M1}(90^\circ, 90^\circ)} \right) \\ A(90^\circ, 0^\circ) &= \frac{1}{N_T \cdot N_{\gamma,\mathrm{tot}} \cdot \overline{\epsilon_{\mathrm{HPGe4}}} \cdot \tau_{\mathrm{HPGe4}}} \left(\frac{\sigma_{\gamma\gamma}(E1)}{W_{E1}(90^\circ, 0^\circ)} + \frac{\sigma_{\gamma\gamma}(M1)}{f_4 \cdot W_{M1}(90^\circ, 0^\circ)} \right). \end{aligned} \tag{4.14}$$

The factors f_2 and f_4 are the correction factors deduced from the scaling of the absolute photon-current densities to the ^{64}Ni values calculated using HPGe2 (the $E1$ detector) and HPGe4 (the $M1$ detector) (cf. lower panel of Fig. 4.17). As mentioned before, this method could only be applied for the $E1$ ($M1$) transitions recorded with HPGe2 (HPGe4), since the transitions with the other radiation character were too weak. For each variation of the photon-current densities described above and for each Monte-Carlo iteration of the deconvolution of the deexcitation spectra, Eq. (4.14) was solved. Then, the mean and standard deviation were extracted separately from the resulting probability distributions for the outcomes of the two flux-scaling procedures. By applying the Monte-Carlo approach once again, both results were averaged which yielded the final average elastic cross sections $\sigma_{\gamma\gamma}$. The corresponding standard deviation represents the statistical uncertainty. The differences between the results of the two scaling approaches from the mean value are considered as systematic uncertainty.

In recent NRF studies, the complete excitation-energy range was chosen as energy range δE, e.g., in Refs. [29, 80]. However, the state-to-state analysis of the ^{64}Ni data showed that the strengths of the transitions strongly vary. Due to this and the non-constant energy distribu-

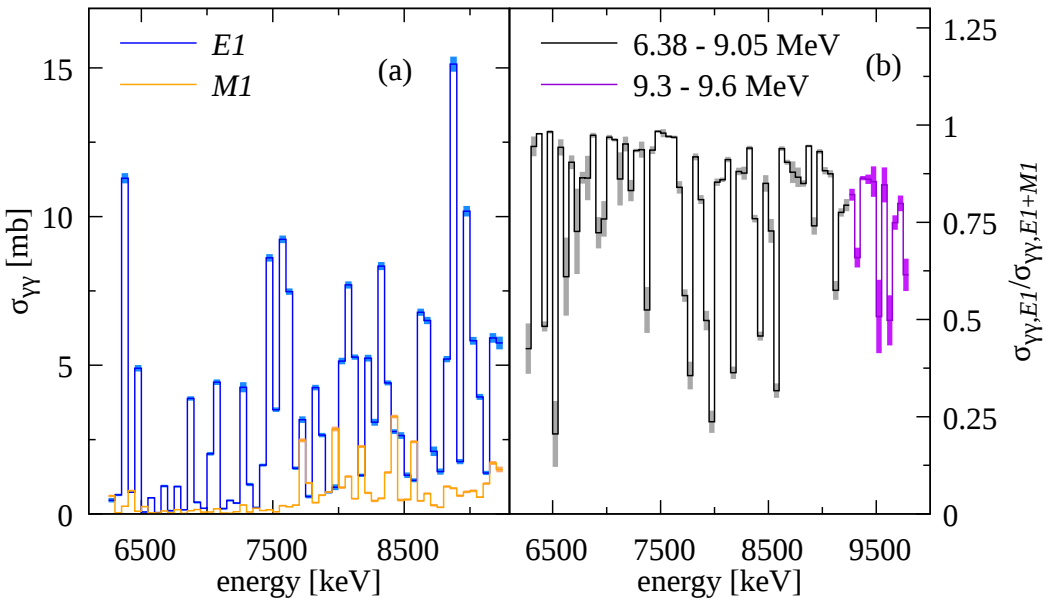

Figure 4.19: Left: $E1$ (blue) and $M1$ (orange) average elastic cross section deduced in 50 keV steps. Right: ratio of the $E1$ channel to the total elastic cross section for beam energies between 6.38 and 9.05 MeV (black) and for the two higher beam-energy settings of 9.3 and 9.6 MeV (purple). The shaded areas represent the statistical uncertainties.

tion of the photons, the estimation given in Eq. (4.13) no longer necessarily holds. Therefore, an energetically-continuous analysis of the average elastic cross section $\sigma_{\gamma\gamma}$ in $\delta E = 50$ keV steps was performed in this analysis. However, the statistics in each bin is still sufficient. The results of the $E1$ and $M1$ channel in 50 keV steps are illustrated in Panel (a) of Fig. 4.19 and the corresponding moving average over an energy range of 200 keV is displayed in Chapter 5. For the calculation of the moving average, the uncertainties were determined by using the Monte-Carlo approach and by varying the individual cross sections within their corresponding uncertainties following a Gaussian distribution. The display of the results as moving average has the advantage that more general trends can be observed although information about fine structure can be lost. In Panel (b) of the Fig. 4.19, the ratio of the $E1$ channel with respect to the total average elastic cross section is illustrated. This is a relative quantity and no absolute photon-current densities had to be known. Therefore, it was also extracted from the data recorded during the 9.3 and 9.6 MeV measurements (purple).

A good estimation of the total average elastic cross section can be obtained by investigating the deconvoluted spectra recorded by the backward detector due to its similar angular distributions $W_{E1,M1}(135°, 45°) \approx 1.2$ of $E1$ and $M1$ transitions. This result was extracted in 50 keV steps as well and the corresponding moving average over an energy range of 200 keV (red) is

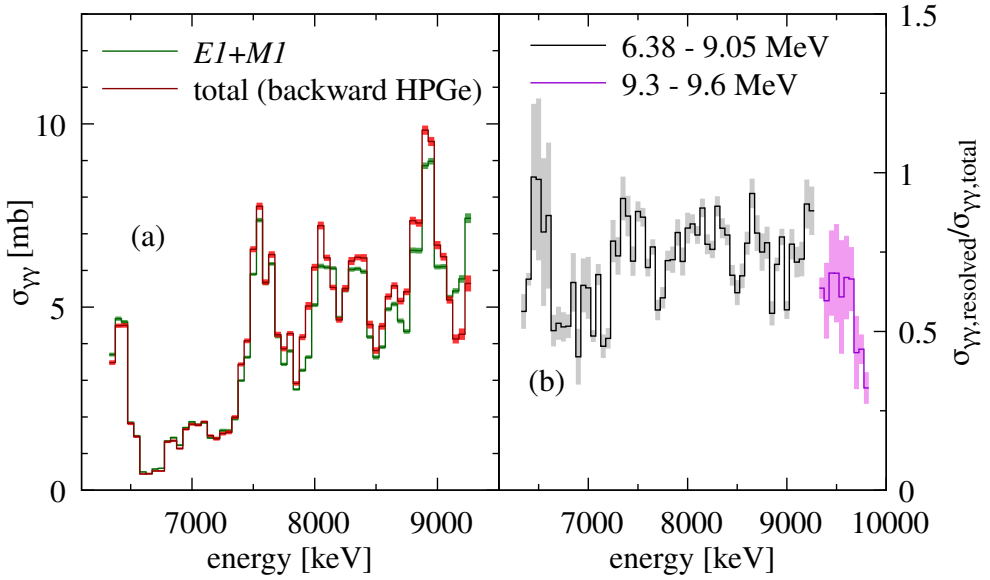

Figure 4.20: Panel (a): the average elastic cross sections were calculated in 50 keV steps and are shown as moving average over an energy range of 200 keV. In red, the results obtained by investigating the backward detector, for which the angular distributions of $E1$ and $M1$ transitions are very similar, are depicted. In green, the average cross sections were determined by summing the $E1$ and $M1$ contributions which were obtained using the $\theta = 90^\circ$ detectors. Panel (b): the ratios of the cross section included in resolved ground-state decays with respect to the total elastic cross section are illustrated between 6.38 and 9.05 MeV in black and between 9.3 and 9.6 MeV in purple. In both panels, only the statistical uncertainties are shown.

compared to the sum of the $E1$ and $M1$ channels (green) in Fig. 4.20. The agreement of both results serves as confirmation for the disentanglement procedure of the two contributions and, in this way, for the assumption of a negligible correction factor for $W_{E1}(90^\circ, 0^\circ) \cdot \epsilon(90^\circ, 0^\circ)$ ($W_{M1}(90^\circ, 90^\circ) \cdot \epsilon(90^\circ, 90^\circ)$) for the $M1$ ($E1$) detector. Panel (b) shows the ratios between the resolved and the complete elastic cross section using the backward detector for the beam energies between 6.38 and 9.05 MeV in black and for the beam energies of 9.3 and 9.6 MeV in purple. In average, the main part of the elastic decay channel is contained in resolved transitions but a decreasing trend with increasing energy can be observed.

In Fig. 4.21, the comparison between the results of the average elastic cross sections $\sigma_{\gamma\gamma}$ extracted from the continuous analysis in 50 keV steps in terms of the moving average over an energy range of 200 keV (red) and from the analysis of the complete excitation-energy region at once (black) is presented. The data were obtained from the analysis of the deexcitation spectra recorded by the backward detector. As illustrated, the results of both methods are very similar although the continuous analysis emphasizes the fine structure of the elastic

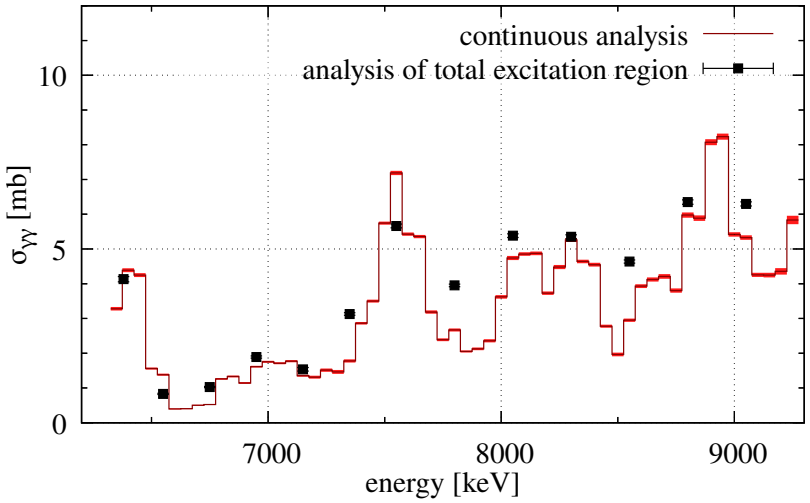

Figure 4.21: Comparison of the average elastic cross sections determined in the continuous analysis in terms of the moving average over an energy range of 200 keV (red) and by investigating the complete excitation regions at once (black). The results were deduced by using the spectra recorded by the backward detector. Only statistical uncertainties are included.

cross section.

Inelastic cross section

To investigate the inelastic-decay channel, it can be taken advantage of the fact that most lower-lying states, which are populated by the decay of the directly-excited levels by the quasimonoenergetic photon beam, decay themselves via one of the low-lying 2^+ states, i.e., these states act as a kind of funnel. Therefore, by means of the ground-state-decay intensity of the low-lying 2^+ states, the strength of the inelastic-decay channel can be estimated.
In the case of ^{64}Ni, the ground-state decays of the 2^+_1 state at 1346 keV, the 2^+ levels at 3154 and 3275 keV, and a state at 2972 keV, which spin-parity quantum number is given with $(1, 2^+)$, were investigated [73]. For this purpose, Eq. (4.13) is modified to [86]:

$$\sigma_{\gamma\gamma'} = \frac{\sum_x I_{S,x\to k}}{\delta E} \sim \frac{A(2^+)}{N_T \cdot N_{\gamma,\mathrm{tot}} \cdot \epsilon(E_{2^+}) \cdot \tau \cdot \overline{W_{\Pi L}(\theta,\phi)}}. \tag{4.15}$$

Here, the sum of the energy-integrated cross sections includes only transitions from the directly-excited state x in the excitation-energy region to an intermediate state k. The angular distribution is replaced by an average value $\overline{W_{\Pi L}(\theta,\phi)}$ since many different angular-correlation functions overlap.
As indicated in Fig. 4.21, the average elastic cross sections $\sigma_{\gamma\gamma}$ obtained from the analysis of

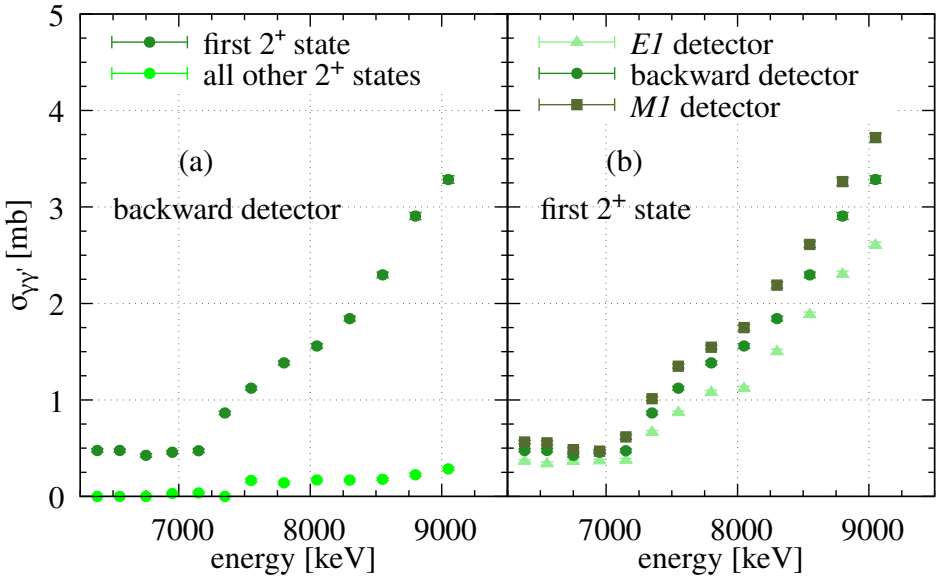

Figure 4.22: Panel (a): comparison between the average inelastic cross sections deduced from the ground-state decay of the 2_1^+ (dark green) and of all other low-lying 2^+ states (light green). The cross sections were determined using the backward detector. Panel (b): average inelastic cross sections corresponding to the ground-state decay of the 2_1^+ state calculated using the $E1$, backward, and $M1$ detectors are shown as triangles, circles, and squares, respectively. Only statistical uncertainties are included.

the total excitation-energy region represent the results of the continuous analysis well. Therefore, it is assumed that the average inelastic cross section can also be estimated in this manner, i.e., for the determination of $N_{\gamma,\mathrm{tot}}$, the photon-current densities were integrated over the total excitation regions.

On the one hand, the contributions of the different low-lying excited 2^+ states were investigated using the backward detector only (Panel (a) of Fig. 4.22). It was observed that the main part of the inelastic strength is collected by the 2_1^+ state.
On the other hand, the peak area of the ground-state decay of the 2_1^+ state was determined from the deexcitation spectra of each HPGe detector separately (cf. Panel (b) of Fig. 4.22). It can be seen that the cross sections determined by using the $M1$ detector are approximately 35 % (15 %) higher than the results obtained with the $E1$ (backward) detector. For this comparison, it was presumed that the detection efficiencies of all HPGe detectors are in agreement relative to each other which should be guaranteed by the source measurements. Furthermore, the calculation of the photon-current densities in Sec. 4.2.4 showed that the deviations are only in the order of 5 % above 5 MeV.

However, as shown in the right panel of Fig. 4.22, the deviations between the average inelastic cross sections are approximately constant, i.e., independent of the excitation energy. This indicates an inaccurate FEP efficiencies at low γ-ray energies. It was tested if differently strong absorption behaviors in the target depending on the amount of target material, which has to be passed before reaching the HPGe detectors, could be the reason for this discrepancy. This would affect mainly the low-energetic γ rays recorded by the $\theta = 90^\circ$ detectors (cf. Fig. 4.8). If the target was tilted, which could be one reason for the discrepancy between the photon distributions impinging on the target and the 0° detector, the effect of the absorption could be different. To estimate this impact, the ratios of the simulations with and without target were investigated for each detector individually. It was found that the difference is in the order of 5 % for the $\theta = 90^\circ$ detectors at 1346 keV and decreases with increasing energy. Above 3500 keV, the impact is negligible. In the case of the backward detector, it is negligible for all γ-ray energies. Therefore, it was concluded that the possibly different positions of target and source are, at least, not the only reason for the observed discrepancies of the $\sigma_{\gamma\gamma'}$ values. Nevertheless, it cannot be excluded that, in general, inaccurate efficiencies are the reason for the differences.

However, this asymmetry could also be an indication for a non-isotropic angular distribution of the ground-state decay of the 2_1^+ state. Decays of excited 0^+ states are isotropic and, therefore, they can be used as reference for testing the isotropy of γ rays corresponding to a different decay. Therefore, the ratios

$$\frac{A(2_1^+ \rightarrow 0_1^+)/\epsilon(E_{2_1^+ \rightarrow 0_1^+})}{A(0_i^+ \rightarrow 2_1^+)/\epsilon(E_{0_i^+ \rightarrow 2_1^+})} \qquad \text{with} \quad i = 2, 3 \tag{4.16}$$

were calculated. As stated in Eq. (4.16), the decays of the second and third 0^+ were observed in the experiment. When this ratio is the same for all HPGe detectors, it can be concluded that the angular distribution of the $2_1^+ \rightarrow 0_1^+$ decay is isotropic at the corresponding photon-beam energy. Although the corresponding γ-ray energies ($E_\gamma(0_2^+ \rightarrow 2_1^+) = 1522$ keV and $E_\gamma(0_2^+ \rightarrow 2_1^+) = 1680$ keV) [73] are similar to that of the ground-state decay of the 2_1^+ state ($E_\gamma(2_1^+ \rightarrow 0_1^+) = 1346$ keV), it cannot be assumed that the FEP efficiencies are the same (cf. Fig. 4.8). That prevents to draw a final conclusion. Nevertheless, the comparison showed different behaviors depending on the excitation energy. This implies that discrepancies cannot only occur due to inaccuracies of the FEP efficiencies because these would affect each beam energy in the same way.

In conclusion, the reason for the different average inelastic cross sections, depending on the used detector for the determination, could not be firmly identified. Hence, the means of all

average inelastic cross sections $\sigma_{\gamma\gamma'}$ were calculated to account for the observed discrepancies in the further analysis.

5 | Publication I: Low-lying dipole response of ^{64}Ni

Low-lying dipole response of ^{64}Ni

M. Müscher,[1,*] E. Litvinova,[2,3,4] R. Schwengner,[5] T. Beck,[3] D. Bemmerer,[5] F. Fiedler,[5] S. W. Finch,[6,7] U. Friman-Gayer,[8] S. Hammer,[5] J. Isaak,[9] R. V. F. Janssens,[7,10] A. R. Junghans,[5] N. Kelly,[11] F. Kluwig,[1] Krishichayan,[6,7] S. E. Müller,[5] O. Papst,[9] K. Römer,[5] D. Savran,[12] M. Scheck,[11] T. Schüttler,[1] J. Sinclair,[11,13] T. Szücs,[5,†] W. Tornow,[6,7] A. Wagner,[5] J. Wilhelmy,[1] and A. Zilges[1]

[1]*Universität zu Köln, Institut für Kernphysik, 50937 Köln, Germany*
[2]*Department of Physics, Western Michigan University, Kalamazoo, Michigan 49008, USA*
[3]*Facility for Rare Isotope Beams, Michigan State University, East Lansing, Michigan 48824, USA*
[4]*GANIL, CEA/DRF-CNRS/IN2P3, F-14076 Caen, France*
[5]*Helmholtz-Zentrum Dresden-Rossendorf, 01328 Dresden, Germany*
[6]*Department of Physics, Duke University, Durham, North Carolina 27708, USA*
[7]*Triangle Universities Nuclear Laboratory, Durham, North Carolina 27708, USA*
[8]*European Spallation Source ERIC, 22484 Lund, Sweden*
[9]*Institut für Kernphysik, Technische Universität Darmstadt, 64289 Darmstadt, Germany*
[10]*Department of Physics and Astronomy, University of North Carolina at Chapel Hill, Chapel Hill, North Carolina 27599, USA*
[11]*School of Computing, Engineering, and Physical Sciences, University of the West of Scotland, Paisley PA1 2BE, United Kingdom*
[12]*GSI Helmholtzzentrum für Schwerionenforschung GmbH, 64291 Darmstadt, Germany*
[13]*SUPA, Scottish Universities Physics Alliance, United Kingdom*

(Received 28 October 2023; accepted 23 February 2024; published 15 April 2024)

Two complementary real-photon scattering experiments were conducted on the proton-magic ^{64}Ni nucleus to study the dipole response up to its neutron-separation energy of $S_n = 9.7$ MeV. By combining both measurements, 87 $E1$ and 23 $M1$ transitions were identified above 4.3 MeV. The results of the observed $M1$ transitions were compared to shell-model calculations using two different model spaces. It was found that the inclusion of excitations across the $Z = 28$ shell gap in the calculations has a large impact. Furthermore, average cross sections for decays to the ground state (elastic transitions) as well as to lower-lying excited states (inelastic decays) were determined. The corresponding $E1$ channel was compared to calculations within the relativistic equation of motion (REOM) framework. Whereas the calculations of highest possible complexity reproduce the fragmentation and overall behavior of the $E1$ average elastic cross section well, the predicted absolute cross sections are approximately twice as high as the experimental upper limits even though the latter also include an estimate of the inelastic-decay channel.

DOI: 10.1103/PhysRevC.109.044318

I. INTRODUCTION

For decades, the investigation of the low-lying dipole response of atomic nuclei has been a topic of great interest. Especially, the accumulation of electric dipole ($E1$) strength on top of the low-energy tail of the isovector giant dipole resonance (IVGDR) [1], commonly denoted as the pygmy dipole resonance (PDR), has attracted a lot of attention [2–4]. Nevertheless, some open questions concerning this $E1$ excitation mode remain, including its microscopic structure and its origin.

Systematic studies of the PDR are one approach for achieving a better understanding. On the one hand, these can be performed along isotopic and isotonic chains to investigate the influence of changes in, e.g., shell structures, neutron excess, and deformation. Such studies were performed, e.g., on the $N = 82$ isotonic chain [5–11] and the $Z = 50$ isotopes [12–16] using real-photon scattering experiments.

On the other hand, comparisons between the observed electric dipole response induced in various nuclear reactions can be a testing ground for the excitation mechanism (see, e.g., Refs. [14,17,18]). These studies become difficult if a non-negligible contribution of $M1$ strength—likely stemming from spin-flip resonances—is also located close to the neutron-separation energy S_n. This is the case, e.g., in nuclei close to the $N = 28$ or $Z = 28$ shells, such as ^{54,56}Fe [19,20] and ^{58,60}Ni [21–23]. In these nuclei, a considerable magnetic dipole ($M1$) contribution was observed in $(\vec{\gamma}, \gamma')$ measurements with a polarized photon beam. Thus, especially for these nuclei, a clear distinction between $E1$ and $M1$ contributions is crucial.

Two complementary (γ, γ') experiments on the proton-magic $Z = 28$ nucleus ^{64}Ni were performed to expand the

*muescher@ikp.uni-koeln.de
†Present address: Institute for Nuclear Research (Atomki), 4001 Debrecen, Hungary.

investigations of the dipole response in medium-mass nuclei. Real-photon scattering measurements have already been performed on the two lightest stable, even-even Ni isotopes ^{58,60}Ni up to 10 MeV [21–23] and the $N = 36$ isotone ^{66}Zn up to the neutron-separation energy $S_n = 11.1$ MeV [24,25]. The combination of complementary (γ, γ') experiments using bremsstrahlung as well as polarized quasimonoenergetic photon beams from laser-Compton backscattering (LCB) enabled the clear identification of the observed transitions and the determination of absolute physical quantities.

This article starts with a short introduction to real-photon scattering experiments and continues with descriptions of the experiments and the analysis techniques. Finally, the experimental results for the $E1$ channel are compared to calculations in the equation of motion (EOM) framework, and the $M1$ ground-state transitions of resolved states are discussed with respect to shell-model calculations.

II. NUCLEAR RESONANCE FLUORESCENCE METHOD

The nuclear resonance fluorescence (NRF) method is based on real-photon scattering [26–28]. Real photons predominantly induce dipole and, with a lower probability, also quadrupole transitions from the ground state because they can only transfer small angular momenta. The deexcitation of the photoexcited state can either happen directly back to the ground state by the emission of a single photon (elastic transition) or via intermediate states and, subsequently, back to the ground state by emitting more than one γ ray (inelastic transition). Because real photons are used in the entrance and in the exit channel, many quantities can be extracted in a model-independent way. In this section only a short introduction to the formalism of NRF based on Refs. [26–28] is given. For further information, the reader is referred to these review articles.

A. State-to-state analysis

One measure for the probability that a certain transition occurs, which can directly be extracted from NRF experiments, is the so-called energy-integrated cross section I_S. It is calculated by correcting the number of recorded events at the respective γ-ray energy E_γ, i.e., the integrated peak area A in the deexcitation spectrum, for the number of target nuclei N_T, the number of incident photons per energy and area at the corresponding excitation energy $N_\gamma(E_x)$, the detection efficiency $\epsilon(E_\gamma)$, and the angular distribution $W_{\Pi L}(\theta, \phi)$:

$$I_S = \frac{A}{N_T N_\gamma(E_x)\epsilon(E_\gamma)W_{\Pi L}(\theta,\phi)}. \tag{1}$$

The scattering angle θ is defined as the angle between the incoming and the outgoing photons. The angle between the polarization plane, spanned by the direction of the electric field of the incoming photons and its direction of movement, and the direction of movement of the outgoing γ rays is denoted as ϕ. If an unpolarized photon source is utilized for the excitation, the angular distribution $W(\theta)$ is independent of ϕ. Since the angular distribution is dependent on the multipole order L and the radiation character Π, i.e., electric (E) or magnetic (M), the observed transition has to be characterized first.

To assign the multipolarity L, the ratio ω of the angular distributions at two different scattering angles has to be calculated according to

$$\omega = \frac{W(90^\circ)}{W(127^\circ)} = \frac{A(90^\circ)}{A(127^\circ)}\frac{\epsilon(E_\gamma, 127^\circ)\tau(127^\circ)}{\epsilon(E_\gamma, 90^\circ)\tau(90^\circ)}. \tag{2}$$

For this purpose, $\theta = 90^\circ$ and $\theta = 127^\circ$ are best suited since the difference between the ratios for pure dipole, $\omega(L = 1) = 0.73$, and quadrupole transitions, $\omega(L = 2) = 2.28$, is the largest. The theoretical ratios are compared to the number of recorded events at the different scattering angles corrected for the corresponding detection efficiencies $\epsilon(E_\gamma, \theta)$ and the effective measuring times τ [see Eq. (2)].

For the determination of the radiation character Π, among others, a linearly polarized γ-ray beam in the entrance channel can be used via the so-called analyzing power Σ_{hv}. This is defined by the angular distributions $W(\theta, \phi)$ ([29]):

$$\Sigma_{hv} = \frac{W(90^\circ, 0^\circ) - W(90^\circ, 90^\circ)}{W(90^\circ, 0^\circ) + W(90^\circ, 90^\circ)} = q\epsilon_{hv}. \tag{3}$$

The factor q corrects for the finite opening angles of the detectors and the degree of polarization. The quantity ϵ_{hv} denotes the experimental observable, i.e., the so-called asymmetry between the horizontal and the vertical detectors with respect to the polarization plane. It is calculated by replacing the theoretical angular distributions $W(\theta, \phi)$ by the number of recorded counts at the corresponding angles (θ, ϕ), corrected for $\epsilon(E_\gamma, \theta)$ and τ according to Eq. (2). The theoretically expected angular distributions of an electric (magnetic) dipole transition equal $W(90^\circ, 0^\circ) = 0$ (1.5) for a detector in the polarization plane and $W(90^\circ, 90^\circ) = 1.5$ (0) for a detector positioned perpendicular to this plane. Therefore, the analyzing power is $\Sigma_{hv} = +1$ for an $M1$ transition and $\Sigma_{hv} = -1$ for an $E1$ transition. In the following, the detector in the polarization plane is denoted as the $M1$ detector and the detector perpendicular to the polarization plane as the $E1$ detector, due to the angular distributions.

The total decay width Γ equals the sum of all partial decay widths Γ_f, with f being the populated state, including the ground-state decay width Γ_0. When the ratio Γ/Γ_0, which is the inverse ground-state decay branching ratio, is known, the reduced transition strengths $B(\Pi L)\downarrow$ for the deexcitation process can be deduced via

$$B(E1)\downarrow\,[e^2\mathrm{fm}^2] = 8.29\times10^{-4}\times\frac{\Gamma}{\Gamma_0}\frac{I_S[\mathrm{keV\,fm}^2]}{E_\gamma[\mathrm{MeV}]}$$

$$B(M1)\downarrow\,\left[\mu_\mathrm{N}^2\right] = 7.46\times10^{-2}\times\frac{\Gamma}{\Gamma_0}\frac{I_S[\mathrm{keV\,fm}^2]}{E_\gamma[\mathrm{MeV}]}, \tag{4}$$

where it was assumed that $E_\gamma = E_x$. To calculate the reduced transition strength for the excitation process, the following equation holds:

$$B(\Pi L)\uparrow = \frac{2J+1}{2J_0+1}B(\Pi L)\downarrow. \tag{5}$$

Here, J and J_0 are the spin quantum numbers of the excited and the ground state, respectively.

B. Average quantities

Besides the investigation of individual transitions, average quantities can be determined by using, e.g., NRF experiments with a quasimonoenergetic γ-ray beam.

In this way, elastic decays, which are too weak to appear as distinct peaks in the deexcitation spectra, can be included. For this purpose, the total number of recorded NRF events $A(\mathrm{tot})$ in the excitation-energy region δE is investigated and corrected for the number of incoming photons in the same energy range $N_{\gamma,\mathrm{tot}}$. The elastic cross section $\sigma_{\gamma\gamma}$ can be calculated using [30,31]

$$\sigma_{\gamma\gamma} = \frac{\sum_x I_{S,x\to 0}}{\delta E} \approx \frac{A(\mathrm{tot})}{N_T N_{\gamma,\mathrm{tot}}\,\overline{\epsilon(E_\gamma)}\,W_{\Pi L}(\theta,\phi)}. \quad (6)$$

Here, $\overline{\epsilon(E_\gamma)}$ is the average detection efficiency. The expression in Eq. (6) is exact if the energy distribution of the photon beam is constant within the energy interval δE or the strengths of the individual transitions are equally distributed.

The observation of every inelastic transition for each individual state is experimentally challenging. Therefore, the average inelastic cross section $\sigma_{\gamma\gamma'}$ was defined for estimating the contribution of the inelastic-decay channel. The analysis assumes that most of the intermediate states k decay via the low-lying excited 2^+ states. If these 2^+ levels are not directly excited by the quasimonoenergetic photons, the number of recorded ground-state decays of these states $A(2^+)$ can be used to compute the average inelastic cross section $\sigma_{\gamma\gamma'}$ via [6]

$$\sigma_{\gamma\gamma'} = \frac{\sum_x I_{S,x\to k}}{\delta E} \approx \frac{A(2^+)}{N_T N_{\gamma,\mathrm{tot}}\,\epsilon(E_{2^+})\,\overline{W_{\Pi L}(\theta,\phi)}}. \quad (7)$$

For this purpose, the integration of the photon flux has to be performed over the total excitation-energy region. The calculation of the angular distribution $\overline{W_{\Pi L}(\theta,\phi)}$ is challenging. Therefore, it is often assumed to be isotropic, because the lowest-lying states are fed by higher-lying ones and the angular distributions are driven towards isotropy.

The total, average photoabsorption cross section, which is the sum of the elastic and the inelastic cross sections $\sigma_\gamma = \sigma_{\gamma\gamma} + \sigma_{\gamma\gamma'}$, includes the complete dipole response, except for a small fraction of inelastic transitions bypassing the low-lying excited 2^+ states.

III. EXPERIMENTAL DETAILS

In order to study the photoresponse of ^{64}Ni, two complementary real-photon scattering experiments were performed. First, an energetically continuous and mainly unpolarized bremsstrahlung beam, and second, a quasimonoenergetic and fully linearly-polarized photon beam generated by laser-Compton backscattering (LCB) were used as photon sources. The combination of both (γ,γ') experiments enables the differentiation between $E1$, $M1$, and $E2$ transitions and the extraction of quantities such as absolute, energy-integrated cross sections I_S (see Ref. [28] and references therein). In the following, experimental details of both complementary experiments are provided.

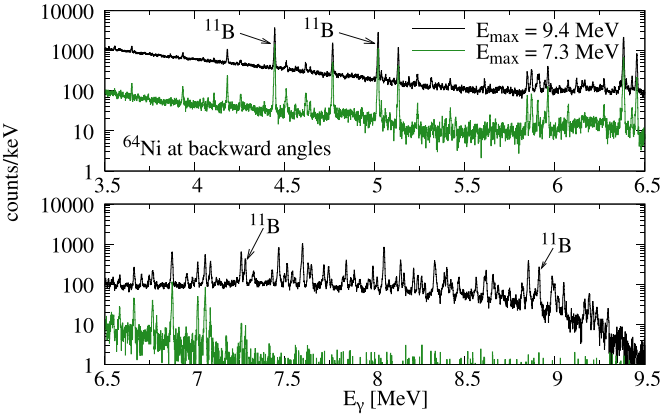

FIG. 1. Deexcitation spectra recorded by the detectors at backward angles of the 7.3 MeV (green) and the 9.4 MeV (black) bremsstrahlung measurements. The most prominent transitions of the calibration target ^{11}B are indicated.

Two bremsstrahlung measurements on ^{64}Ni were conducted at the γELBE facility at the Helmholtz-Zentrum Dresden-Rossendorf (HZDR) [32] using maximal photon energies of $E_{\mathrm{max}} = 7.3$ MeV for 120 h (LE measurement) and of $E_{\mathrm{max}} = 9.4$ MeV for 80 h (HE measurement). For the production of the bremsstrahlung beam with lower (higher) maximal photon energy, an electron beam with $E_{e^-} = 7.3$ MeV ($E_{e^-} = 9.4$ MeV) impinged on a 7 µm (12.5 µm) niobium radiator. The energetically continuous bremsstrahlung beam was collimated (diameter of 4 cm at the target position) and impinged on the ^{64}Ni target disk with a diameter of 1.9 cm. It weighed 1456.56 mg and had an isotopic enrichment of 92.1%. In addition to the target of interest, a ^{11}B target with a similar diameter and a weight of 300 mg (isotopic enrichment 99.5%) served as calibration for the absolute photon-flux determination. The emitted γ rays were detected by four high-purity germanium (HPGe) detectors, two at a scattering angle of $\theta = 90°$ and two at $\theta = 127°$ relative to the incoming photon beam. These were surrounded by lead shields for passive background suppression, and by Compton-suppression bismuth germanate (BGO) shields for additional active background suppression. The distances between the detectors and the targets were 28 cm for the 90° and 32 cm for the backward (127°) detectors. By taking into account the corresponding opening angles of the detectors, the ratios of the angular distributions [cf. Eq. (2)] equal $\omega = 0.74$ and $\omega = 2.15$ for dipole and quadrupole transitions, respectively [19]. Figure 1 illustrates the summed deexcitation spectra of both detectors under backward angles for the low-energy (LE) measurement in green and the high-energy (HE) one in black. The neutron-separation energy of ^{64}Ni is $S_n = 9.7$ MeV.

A complementary $(\vec{\gamma},\gamma')$ experiment was performed on ^{64}Ni at the High Intensity γ-ray Source (HIγS) located at TUNL utilizing a linearly-polarized and quasimonoenergetic γ-ray beam [33]. The photon beam passed a collimator with diameter of 1.9 cm before it impinged on the target. Because of the beam divergence, the beam had a diameter of approximately 2 cm at the target position. For the detection of the deexciting γ rays, the γ^3 setup was used

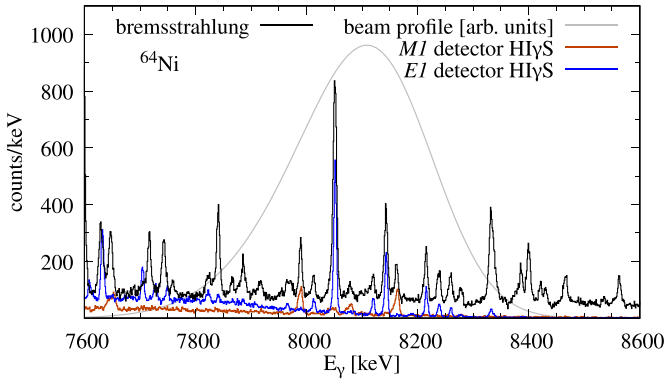

FIG. 2. The deexcitation spectra recorded by the $M1$ detector $(90^\circ, 0^\circ)$ and the $E1$ detector $(90^\circ, 90^\circ)$ at HIγS at a beam energy of 8.05 MeV are shown as orange and blue histograms, respectively. The photon-flux distribution in arbitrary units, which impinged on the target, is depicted in gray. The summed deexcitation spectrum recorded by the $\theta = 127^\circ$ detectors of the bremsstrahlung experiment is illustrated in black.

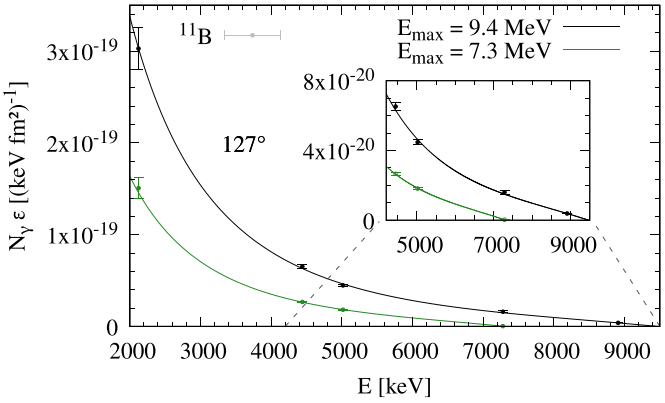

FIG. 3. The products of photon flux and detection efficiency of the backward detectors for the HE and the LE bremsstrahlung measurements are depicted in black and green, respectively. The shapes were scaled to the corresponding ^{11}B values (full circles). See text for details.

[34]. It consisted of four HPGe detectors placed at $(\theta, \phi) = (90^\circ, 90^\circ)$, $(95^\circ, 180^\circ)$, $(135^\circ, 45^\circ)$, and $(135^\circ, 315^\circ)$. Although two HPGe detectors were positioned at backward angles in the experiment, only one of these was taken into account during the analysis due to uncertainties concerning the precise positioning of the other with respect to the target. Additionally, the γ^3 setup includes four $LaBr_3$ detectors which can be used for γ-γ coincidence measurements. For this work, only the HPGe detectors were used.

In total, the experiment was performed with 26 different beam-energy settings between 4.33 and 10 MeV (4.33, 4.48, 4.63, 4.75, 4.93, 5.13, 5.43, 5.63, 5.86, 6.15, 6.38, 6.55, 6.75, 6.95, 7.15, 7.35, 7.55, 7.8, 8.05, 8.3, 8.55, 8.8, 9.05, 9.3, 9.6, and 10.0 MeV) for approximately 3 to 4 h each. The deexcitation spectra recorded by the $M1$ $(90^\circ, 0^\circ)$ and $E1$ $(90^\circ, 90^\circ)$ detectors at a beam energy of 8.05 MeV are displayed as orange and blue histograms, respectively, in Fig. 2. The excitation region is indicated by the beam profile (gray) in arbitrary units. In addition, the bremsstrahlung spectrum (black) recorded by the backward detectors is illustrated for comparison. For all measurements up to 9.05 MeV, the same ^{64}Ni target was used as for the bremsstrahlung experiment. For the three settings with the highest energies (9.3, 9.6, and 10 MeV), it was replaced by a ^{64}Ni target with a diameter of 8 mm and a total weight of 4 g (isotopic enrichment of 92.3%). Before each measurement, a HPGe detector with a relative detection efficiency of 123%, denoted as 0° detector, was positioned in the beam with reduced intensity for measuring the incoming photon-flux distribution.

IV. ANALYSIS AND RESULTS

In this section, the analysis procedures for obtaining the quantities introduced in Sec. II are discussed, and the results are presented.

For the determination of the full-energy-peak efficiencies $\epsilon(E_\gamma)$, source measurements up to 3.5 MeV were performed, and GEANT4 simulations [35–37] were used for the extrapolation to 10 MeV [38,39].

For the bremsstrahlung measurement, the photon-flux distribution was determined by calculating the bremsstrahlung cross section [40] using the process description by Roche *et al.* [41], corrected by the screening of the nuclear Coulomb potential by the surrounding electrons [42]. Afterwards, the products of photon flux and efficiency $N_\gamma(E_x)\epsilon(E_\gamma)$ of the HE (black) and LE (green) measurements were individually scaled to known transitions of the calibration standard ^{11}B [43,44]. These are illustrated by filled circles in Fig. 3 for the detectors positioned at $\theta = 127^\circ$.

For assigning multipolarities to the observed transitions, the intensity ratios were calculated according to Eq. (2). If the experimental intensity ratio was in agreement, within its 2σ range, with only one of the theoretical ratios of the angular distributions ($\omega = 0.74$ for a dipole and $\omega = 2.15$ for a quadrupole transition), a firm assignment was made. A tentative identification was proposed if the experimental ratio was in accordance with only one of the theoretical values within its 3σ range. By assuming that only elastic transitions were observed, spin quantum numbers were associated to corresponding states due to the 0^+ ground state of ^{64}Ni (see Table I). Up to a γ-ray energy of 6.5 MeV, the low-energy measurement was used for multipolarity assignments and, for higher energies, the 9.4 MeV one was preferred to minimize the effect of feeding contributions from higher-lying states to the levels of interest. Tentatively assigned spin quantum numbers are given in parentheses in Table I.

Afterwards, the energy-integrated cross sections I_S were computed using Eq. (1). For all firmly and tentatively identified dipole transitions, the energy-integrated cross sections I_S were calculated using the 127° detectors as the corresponding statistical uncertainties are smaller compared to those of the 90° detectors.

By using the HIγS data and applying Eq. (3), the radiation character was deduced. The index h (v) indicates that the detector positioned parallel (perpendicular) to the polarization plane, i.e., $\phi = 0^\circ$ ($\phi = 90^\circ$), was utilized. A firm (tentative)

TABLE I. The table provides excitation energies E_x and assigned spin and parity quantum numbers J^π. Tentatively assigned ones are given in parentheses. The energy-integrated cross section I_S and the corresponding product of reduced transition strength $B(\Pi L)\downarrow$ and Γ_0/Γ are listed. When the radiation character could not be determined, the reduced transition strengths for both possibilities are given. The statistical and systematic uncertainties are quoted in the first and second parentheses, respectively. If the parity quantum number was assigned by comparing the energy-integrated cross sections, it is indicated with an asterisk. Two I_S values are given if they were extracted from the HIγS data and the radiation character is unknown. The first (second) value corresponds to an assumed $E1$ ($M1$) transition deduced from the spectra of the $E1$ ($M1$) detector. A systematic uncertainty of ± 1 keV is assumed for the excitation energies.

E_x (keV)	J^π	I_S (keV fm^2)	$B(E1)\downarrow \times\Gamma_0/\Gamma$ (10^{-5} e^2fm^2)	$B(M1)\downarrow \times\Gamma_0/\Gamma$ ($10^{-3}\mu_N^2$)
4617	1^+	1.55(9)(16)		25.1(14)(25)
4765	1^-	11.79(22)(118)	205(4)(20)	
4995[a]	1^+			
5059	1	0.51(7)(5)	8.4(12)(8)	7.5(11)(8)
5130	1^-	11.81(24)(118)	190(4)(19)	
5419	1	0.80(9)(8)	12.1(14)(12)	10.9(12)(11)
5640	$1^{(+)}$	0.38(7)(4)		5.0(10)(5)
5846	1^-	2.90(17)(29)	41.0(24)(41)	
5905	1^-	2.56(17)(26)	35.8(24)(36)	
5961	1^-	6.06(25)(61)	84(3)(8)	
6074	1^-	4.3(12)(7)[b]	58(16)(9)	
6166	1^+	1.25(17)(13)		15.1(20)(15)
6273	1^+	2.16(14)(22)		25.6(17)(26)
6382	1^-	48.5(4)(49)	629(6)(63)	
6402[a]	1^+	0.68(5)(10)[b]		7.9(6)(11)
6429	1^+	2.88(15)(29)		33.3(18)(33)
6455	1^-	17.98(28)(180)	230(4)(23)	
6537	1^+	0.83(12)(8)		9.5(14)(9)
6582	1^-	1.70(14)(17)	21.4(18)(21)	
6663	1^-	5.16(20)(52)	64.0(25)(64)	
6687[a]	$1^+, 2^+$	0.57(7)(6)[b]		6.4(8)(6)
6765	1^-*	4.75(20)(48)	58.1(25)(58)	
6875	1^-	19.3(3)(19)	232(4)(23)	
7016	1^-	8.25(25)(83)	97.3(30)(97)	
7050	1	0.44(7)(6)[b]	5.2(9)(7)	
		0.23(5)(3)[b]		2.5(5)(3)
7058	1^-	15.2(3)(15)	178(4)(18)	
7086	1^-	5.3(3)(11)[b]	62(4)(13)	
7175	1^-	1.12(18)(11)	12.9(21)(13)	
7258	1^-	18.0(8)(36)[b]	205(9)(42)	
7272	1^+	0.76(7)(15)[b]		7.8(7)(16)
7328	1^-	4.4(3)(4)	50(4)(5)	
7387[a]	1, 2	0.53(14)(7)[b]	6.0(16)(8)	
		0.67(7)(8)[b]		6.7(7)(8)
7430	1^-	5.71(27)(57)	64(3)(6)	
7457	1	2.18(30)(22)	24.1(34)(24)	21.7(30)(22)
7466	1^-	31.1(5)(31)	344(6)(34)	
7499	1^-	3.83(21)(47)[b]	42.2(23)(52)	
7513	1^-	11.1(3)(11)	122(4)(12)	
7557	1^-	2.60(24)(26)	28.5(26)(28)	
7590	1^-	7.8(4)(8)	85(4)(8)	
7599	1^-	42.1(6)(42)	459(7)(46)	
7631	1^-	10.3(3)(11)[b]	112(3)(12)	

TABLE I. (*Continued.*)

E_x (keV)	J^π	I_S (keV fm^2)	$B(E1)\downarrow \times\Gamma_0/\Gamma$ (10^{-5} e^2fm^2)	$B(M1)\downarrow \times\Gamma_0/\Gamma$ ($10^{-3}\mu_N^2$)
7648	1^-	10.1(3)(11)[b]	109(3)(12)	
7687[a]	1, 2	1.91(18)(21)[b]	20.6(19)(22)	
		0.78(9)(9)[b]		7.6(8)(8)
7717	1^+*	11.5(4)(11)		111(4)(11)
7743	1^-	11.5(4)(12)	123(4)(12)	
7760	1^+	2.50(26)(25)		24.0(25)(24)
7824	1^-	1.92(17)(24)[b]	20.3(18)(25)	
7841	1^-	17.4(4)(17)	183(5)(18)	
7866	1^-	3.54(30)(35)	37(3)(4)	
7878	1	0.89(13)(11)[b]	9.3(14)(11)	
		1.12(12)(13)[b]		10.6(11)(12)
7887	1^-	6.37(25)(77)[b]	66.8(26)(81)	
7907	1^-	1.24(27)(12)	13.0(28)(13)	
7918	1	0.77(12)(9)[b]	8.1(12)(10)	
		1.60(13)(19)[b]		15.1(12)(18)
7966	1^-	3.5(4)(3)	36(4)(4)	
7990	1^+	11.2(4)(11)		105(4)(10)
8013	1^-	4.4(3)(4)	46(3)(5)	
8043	1	3.6(6)(7)[b]	37(6)(7)	
		1.59(18)(27)[b]		14.7(17)(25)
8052	1^-	47.1(11)(78)[b]	484(11)(80)	
8079	1^+	2.67(29)(27)		24.6(27)(25)
8120	1^-	5.2(3)(5)	53(4)(5)	
8144	1^-	20.0(5)(33)[b]	203(5)(34)	
8163	1^+	8.4(4)(8)		77(4)(8)
8216	1^-	12.4(4)(12)	124(4)(12)	
8239	1^-	8.4(5)(11)[b]	84(5)(12)	
8260	1^-	7.9(4)(8)	79(4)(8)	
8278	1	4.2(3)(4)	42(3)(4)	37.7(29)(38)
8333	1^-	23.9(11)(32)[b]	238(10)(32)	
8342	1^-	12.5(10)(17)[b]	124(10)(17)	
8360[a]	1^+	0.62(12)(10)[b]		5.5(11)(9)
8376	1^+	3.6(4)(4)		32(4)(3)
8387	1^-	11.3(5)(11)	112(5)(11)	
8401	1^-	16.5(5)(22)[b]	163(5)(22)	
8421	1^+	6.0(5)(6)		53(4)(5)
8431	1^+	4.2(5)(4)		37(4)(4)
8467	1^-	10.6(5)(11)	104(5)(10)	
8495[a]	1^-	2.09(31)(26)[b]	20.4(30)(25)	
8520[a]	1^-	0.89(22)(13)[b]	8.6(22)(13)	
8536	$1^{(-)}$	1.40(20)(17)[b]	13.6(20)(16)	
8564	1^+*	9.7(5)(10)		84(4)(8)
8586[a]	1^+	1.26(11)(16)[b]		10.9(10)(14)
8609	1^-	11.6(6)(12)	111(6)(11)	
8619	1^-	17.3(7)(17)	166(6)(17)	
8657	1^-	15.2(5)(18)[b]	145(5)(17)	
8666	1^-	6.10(30)(74)[b]	58.3(28)(70)	
8680	1^+	0.78(11)(9)[b]		6.7(9)(8)
8687	1^-	5.8(8)(6)	55(8)(5)	
8710	1^-	4.2(4)(4)	39(4)(4)	
8748	1^-	5.6(5)(6)	53(4)(5)	
8778[a]	1^-	1.08(25)(16)[b]	10.2(24)(15)	
8786[a]	(1^-)	1.27(25)(17)[b]	12.0(24)(16)	
8818	1^-	8.4(7)(8)	79(7)(8)	
8826	1^-	7.4(4)(9)[b]	69(3)(9)	
8844	1^-*	3.3(5)(3)	31(5)(3)	
8854	1^-	51.2(12)(51)	478(11)(48)	

TABLE I. (*Continued.*)

E_x (keV)	J^π	I_S (keV fm^2)	$B(E1)\downarrow \times\Gamma_0/\Gamma$ (10^{-5} e^2fm^2)	$B(M1)\downarrow \times\Gamma_0/\Gamma$ ($10^{-3}\mu_N^2$)
8865	1	3.89(25)(50)[b]	36.3(24)(46)	
		1.28(13)(17)[b]		10.7(11)(42)
8883	1^-	4.4(5)(4)	41(5)(4)	
8893	1^-	8.5(6)(8)	79(6)(8)	
8903	1^-	6.8(6)(7)	63(6)(6)	
8913[a]	1^+	0.93(15)(12)[b]		7.8(13)(10)
8921[a]	1^-	2.26(24)(31)[b]	21.0(22)(29)	
8934[a]	1^-	1.60(20)(20)[b]	14.8(19)(19)	
8959	1	2.35(45)(24)	21.7(41)(22)	19.6(37)(20)
8986	1^-	23.4(22)(23)	216(20)(22)	
8993	$1^{(-)}$	8.9(19)(9)	82(18)(8)	
9000	1^-	17.3(13)(17)	159(12)(16)	
9009	1	2.52(72)(25)	23.2(66)(23)	20.8(59)(21)
9019	1^-	9.9(7)(10)	91(7)(9)	
9034[a]	1, 2	1.21(20)(15)[b]	11.1(19)(14)	
		1.04(13)(11)[b]		8.6(10)(9)
9050	1^-	19.1(9)(19)	175(8)(17)	
9064	1^-	2.84(54)(28)	25.9(49)(26)	
9076[a]	(1^+)	0.57(10)(6)[b]		4.6(8)(5)
9091[a]	(1^-)	1.78(17)(19)[b]	16.2(16)(18)	
9109[a]	1^+	1.07(13)(11)[b]		8.8(11)(9)
9123[a]	1^-	0.98(17)(11)[b]	8.9(15)(10)	
9132[a]	1, 2	1.13(18)(13)[b]	10.3(16)(12)	
		0.73(12)(8)[b]		6.0(10)(6)
9167	1^-	9.3(8)(9)[b]	84(7)(8)	
9180	1^+	2.55(64)(25)		20.7(52)(21)
9192	1^-	19.0(11)(19)	171(10)(17)	
9212	1^-	8.9(8)(9)	80(7)(8)	
9234	1^-	8.8(8)(9)	79(7)(8)	
9265	$1^{(-)}$	3.0(6)(3)	27.1(56)(27)	
9295	1^-	9.8(9)(10)	87(8)(9)	
9331[a]	(1^-)			
9339[a]	1^-			
9348[a]	$1^+, 2^+$			
9356[a]	1^-			
9363[a]	1, 2			
9369	1^-	6.0(10)(6)	53(9)(5)	
9402[a]	1, 2			
9411[a]	1^-			
9426[a]	1, 2			
9463[a]	1^-			
9474[a]	1^-			
9490[a]	1^-			
9502[a]	1, 2			
9513[a]	1^-			
9522[a]	1^-			
9539[a]	$1^+, 2^+$			
9548[a]	1, 2			
9558[a]	1^-			
9575[a]	1^-			
9600[a]	(1^-)			
9635[a]	(1^-)			
9641[a]	1, 2			
9651[a]	1, 2			

[a]Only observed at HIγS.
[b]Determined from HIγS data.

assignment was made if the asymmetries ϵ_{hv} are in agreement with only one of the simulated asymmetries within their 2σ (3σ) ranges, which include the finite opening angles of the detectors. For example, the simulation yielded values of $\epsilon_{hv} = -0.92$ for $E1$ and $\epsilon_{hv} = 0.90$ for $M1$ transitions with the setup configuration used for the beam energies between 5.86 and 9.05 MeV. An additional uncertainty of 10% was assumed for the simulated asymmetries to take into account a possible deviation of the absolute position of source and target. This uncertainty was justified by the observation of a discrepancy between the $E1$ and $M1$ detector (in total 10%), when calculating the absolute photon flux. In the case of a tentative identification, the corresponding quantum number is given in parentheses in Table I.

In instances where the multipolarity is not firmly known from the γELBE measurements and the asymmetry ϵ_{hv} agrees with the simulated one for an $E1$ transition, a multipole order of $L = 1$ was assumed. Indeed, the asymmetries of an $E1$ and an $M2$ transition are similar, but the probability of inducing $M2$ transitions is negligible. Because the asymmetries ϵ_{hv} of $M1$ and $E2$ transitions are very similar as well, a complete characterization of the transition was done using the HIγS data in the case of an asymmetry value indicating an $M1$ transition. For this purpose, the backward ($\theta = 135^\circ$) detector (indicated by the index b) of the γ^3 setup was taken into account and the asymmetries ϵ_{hb} and ϵ_{vb} were calculated analogously to Eq. (3) [45]. For a firm (tentative) assignment, the experimental values have to be in agreement within 2σ (3σ) with both simulated asymmetries ϵ_{hb} and ϵ_{vb}. These have uncertainties of 10% as well.

At HIγS, a HPGe detector was used to record the shape of the incoming photon flux as stated in Sec. III. The resulting spectra consist of background radiation, γ rays directly stemming from the photon beam, and the resulting detector response. For the deconvolution of the latter two contributions, the unfolding code *Horst* was utilized [46]. It includes a Monte Carlo approach for estimating the impact of uncertainties resulting from the fitting procedure and statistical uncertainties in the spectra as well as from the detector response (for details, see Ref. [46]). The detector response was obtained by performing GEANT4 simulations using the toolkit *utr* [39]. Figure 4 shows the result of the procedure for a beam energy of $E_{\text{beam}} = 8.55$ MeV. The recorded and one of the unfolded spectra are illustrated as gray and black histograms, respectively. In addition, the photon distribution was calculated by using the parameters of the accelerator (red points) [47,48]. A good agreement of both distributions is observed. Experimental values for the photon-current densities were determined using known ^{64}Ni transitions, analyzed in the bremsstrahlung measurement, by rearranging Eq. (1), and adding a correction for the different effective recording times of the individual detectors. For this purpose, the transitions detected by the HPGe detector at $\theta, \phi = 135^\circ, 45^\circ$ were used (light-blue points). Moreover, the dark blue and orange data points were deduced from the detector perpendicular to the polarization plane ($E1$ detector) and the detector parallel to the polarization plane ($M1$ detector), respectively. These were not utilized for the scaling of the photon-flux distribution.

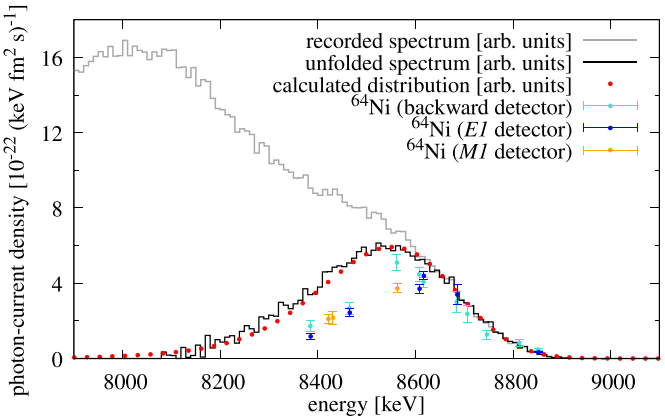

FIG. 4. The recorded photon spectrum of the 0° detector for a beam energy of 8.55 MeV is illustrated in gray and the deconvoluted spectrum as the black histogram. In addition, the same quantity was calculated by utilizing the electron-beam parameters (red points). Experimentally expected photon-current densities using transitions of ^{64}Ni investigated with the backward, $E1$, and $M1$ detectors are displayed as light blue, dark blue, and orange circles, respectively.

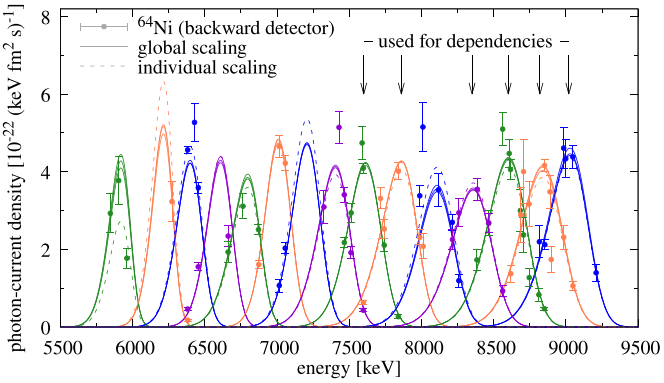

FIG. 5. The absolute photon-current densities are shown for all beam energies between 5.86 and 9.05 MeV. The absolute photon-current densities were obtained by scaling, on the one hand, each distribution to the corresponding ^{64}Ni data (dashed curve) and, on the other hand, all shapes to the ^{64}Ni data of all beam-energy settings at once. The different colors serve for the distinction between the different beam-energy settings. See text for further details.

In this experiment, a considerable deviation between the photon-flux distributions impinging on the 0° detector and on the ^{64}Ni target was observed. One possible explanation can be found in a nonoptimal alignment of the target and the beam. Since the diameters of the target and the beam are very similar and the photon beam has a spatial energy-distribution (high energies are in the center of the beam and low energies at the edges), a displacement would lead to less lower-energy photons impinging on the target than on the 0° detector. Because of this, it was assumed that the number of photons of the recorded profile, which have energies higher than the centroid energy of the deconvoluted spectrum, is the same as the one incident on the ^{64}Ni target. Therefore, the high-energy sides of the deconvoluted 0° spectra were used to describe the high-energy sides of the photon-flux distributions incident on the ^{64}Ni target. For determining the low-energy part, six beam-energy settings, for which the complete shapes of the photon fluxes impinging on the target are well described by the ^{64}Ni data points (indicated by arrows in Fig. 5), were used to define energy dependencies of the widths and centroid energies of the distributions. These were applied to deduce the energy distributions of photons for all beam-energy settings. This step was carried out for all Monte Carlo results obtained from the deconvolution performed with the code *Horst*.

It has to be emphasized that this procedure is based on the assumption that all beam energies were affected in the same way by the possible displacement of the target. However, because the target was moved between the 5.63 and 5.86 MeV measurements, and a ^{64}Ni target with a smaller diameter was used for beam energies above 9.05 MeV (for which the aforementioned effect would be even higher), this procedure was only used for all experimental runs between 5.86 and 9.05 MeV. For beam energies below 5.86 MeV and above 9.05 MeV, an insufficient number of transitions of ^{64}Ni was observed in the bremsstrahlung experiment to determine the distributions by applying the same procedure as explained above. Therefore, only relative quantities could be extracted for these beam energies.

After the determination of the photon-flux distributions, these were scaled to the ^{64}Ni values extracted for isolated transitions. For this procedure, two approaches are possible: (i) the scaling parameters are calculated for each beam energy individually, (ii) a more global method introduced in Ref. [49] is used. The result of the independent scaling is shown by the dashed curves in Fig. 5. For some beam-energy settings, only very few data points are available, which introduces large uncertainties. Therefore, the global procedure presented in Ref. [49] was applied in addition. Here, advantage was taken of the fact that the low-energy background generated by atomic processes in the target is proportional to the total number of incident photons on the target per beam energy. Hence, the low-energy backgrounds for each detector and each beam energy were simulated. By integrating the simulated and experimental spectra in the same energy region (in this case between 370 and 480 keV) and calculating the ratios, the total numbers of photons impinging on the target during the measurement were determined. In this way and by using the same number of simulated photons for all beam energies, the photon-flux distributions were scaled relative to each other. At these low energies, the full-energy-peak efficiencies of the detectors at $\theta = 90°$ were significantly influenced by the absorption of photons within the target before reaching the detector which is dependent on the target's position. To minimize this effect, only the deexcitation spectra of the backward detector were utilized for this purpose. Then, all relatively-scaled photon distributions were simultaneously scaled to all ^{64}Ni values. A more detailed description of this method can be found in Ref. [49].

As can be seen in Fig. 5, the dashed and solid curves are in good agreement for beam energies with data points distributed over the total beam-energy profile. In these cases, the individual scaling should also provide reliable values with small uncertainties.

The energy-integrated cross sections I_S of transitions only observed in the HIγS experiment, or which were possibly affected by feeding or single-escape contributions in the bremsstrahlung experiment, were calculated using the HIγS data and are identified as such in Table I. For the computation of I_S for an $E1$ ($M1$) transition, the detector perpendicular (parallel) to the polarization plane was used. Because the absolute photon-current densities were determined using the backward detector, correction factors had to be applied for the calculation of absolute quantities using the $E1$ and $M1$ detectors. These correction factors take into account uncertainties associated with inaccuracies of the relative products of detection efficiency and angular distribution with respect to the backward detector. The absolute photon-current densities determined using the backward detector were scaled to transitions investigated with the corresponding $\theta = 90^\circ$ detector. For both detectors, the deviations were approximately 5%. Only $E1$ ($M1$) transitions were utilized for the scaling of the photon-current densities of the detector perpendicular (parallel) to the polarization plane, therefore no correction factor could be determined for the other radiation character, and it was assumed to be negligible.

For the estimate of the uncertainty, a Monte Carlo approach was used. Each experimental quantity going into the calculations of the energy-integrated cross sections according to Eq. (1), such as the peak area A of the corresponding transition or the values entering the photon-flux determination, was varied within its statistical uncertainty for each iteration. The mean I_S and its standard deviation were determined from the resulting probability distributions for the outcomes of the two flux-scaling procedures separately. Subsequently, the Monte Carlo approach was once again applied to average both results, yielding the final energy-integrated cross section. The corresponding standard deviation represents the statistical uncertainty. The systematic uncertainty associated with the difference between the two scaling approaches was extracted from the discrepancies between the final I_S values and the values obtained from the two separate procedures. Furthermore, a systematic uncertainty of 10% was applied, reflecting the determination of the product of efficiency and photon flux at γELBE. This uncertainty accounts for the accuracy of the fit functions used to describe the ^{11}B calibration points. Both contributions were combined and are presented in Table I as systematic uncertainties. When extracting the energy-integrated cross sections and reduced transition strengths from the γELBE measurement, only the latter is quoted as systematic uncertainty. To minimize the statistical uncertainties, the peak area extracted from the detector perpendicular (parallel) to the polarization plane was used for an identified $E1$ ($M1$) transition. If a radiation-character assignment was not possible and the HIγS results had to be used, the energy-integrated cross sections for both possibilities are given. Then, the first value was extracted from the perpendicular $\phi = 90^\circ$ detector assuming an $E1$ transition and the second from the parallel $\phi = 0^\circ$ detector assuming an $M1$ transition. For known $E2$ transitions, it was observed that feeding contributions occur also in the LE bremsstrahlung measurement up to approximately 4.5 MeV and the HIγS data only cover the energy range above 4.3 MeV. Therefore, only ground-state transitions above this energy are included in Table I. It should be pointed out that below 5.86 MeV no absolute photon-current densities could be determined for the HIγS data. Hence, energy-integrated cross sections and transition strengths may be contaminated by feeding and single-escape contributions below this energy.

TABLE II. Energy-integrated cross sections determined from the bremsstrahlung (γELBE) and the HIγS experiments using the $E1$ and the $M1$ detectors are given for transitions with unknown radiation character due to the asymmetry ϵ_{hv}. The first quantity in parentheses is the statistical uncertainty and the second is the systematical uncertainty of the photon flux at HIγS. The uncertainty of the photon flux at γELBE is not included.

	I_S (keV fm^2)		
E_x (keV)	γELBE	HIγS $E1$ det.	HIγS $M1$ det.
6765	4.75(20)	4.32(19)(12)	1.06(8)(3)
7717	11.5(4)	3.16(31)(7)	10.73(36)(19)
8564	9.7(5)	3.37(25)(7)	8.71(26)(17)
8844	3.3(5)	3.43(31)(11)	1.86(15)(5)

In four cases, the radiation character was assigned by comparing the two possible I_S values determined from the HIγS data to the γELBE result. The corresponding energy-integrated cross sections are presented in Table II. These spin-parity quantum numbers are indicated by an asterisk in Table I. Feeding contributions to these states, which would affect the energy-integrated cross sections extracted from the bremsstrahlung analysis, were excluded due to the comparison of the HE and LE measurements at γELBE.

In all, 87 1^- states and 23 1^+ states were firmly identified between 4.3 MeV and S_n by combining the HIγS and γELBE results. Eight states were tentatively identified as 1^- states and two as 1^+ ones. For eleven states, $J = 1$ was determined.

Besides the investigation of individual transitions, average elastic cross sections $\sigma_{\gamma\gamma}$ were determined for all beam-energy settings with known absolute photon-current densities from the HIγS data, i.e., for all beam energies between 5.86 and 9.05 MeV. For this purpose, the recorded deexcitation spectra were deconvoluted using the code *Horst*. Afterwards, the absolute photon-current density and the deconvoluted spectra were integrated in the same energy range δE to apply Eq. (6). Because of the nonconstant photon-current density and individual, very strong transitions of ^{64}Ni, the width of the integration interval was chosen to be $\delta E = 50$ keV. No $E2$ transition was identified in the state-to-state analysis above 5 MeV. Hence, only the $E1$ and $M1$ channels of the elastic cross section were disentangled following the approach described in Ref. [45]. Because the recorded deexcitation spectra of both $\theta = 90^\circ$ detectors consist of superpositions of $E1$ and $M1$ transitions, two linear equations with two unknown parameters, $\sigma_{\gamma\gamma}(M1)$ and $\sigma_{\gamma\gamma}(E1)$, were set up according to Eq. (6). As described above, the determination of the absolute photon-current densities using the $E1$ and $M1$ detectors showed 5% discrepancies with respect to the backward detector. This corresponds to uncertainties of the product of angular distribution and efficiency. As stated above, these deviations were

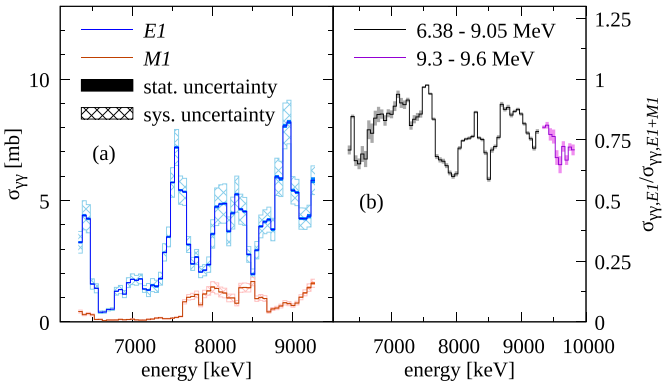

FIG. 6. In panel (a), the moving average over a range of 200 keV of the elastic cross sections of the $E1$ and $M1$ channels deduced in 50 keV steps is shown in blue and orange, respectively. The statistical uncertainties (shaded areas) are small. The systematic uncertainties (resulting from the photon fluxes of the γELBE and HIγS measurements, see text) are depicted as crosshatched areas. Panel (b) illustrates the fraction of the $E1$ contribution with respect to the total cross section. This ratio was calculated not only for beam energies between 6.38 and 9.05 MeV (black), but also for the beam-energy settings of 9.3 and 9.6 MeV for which absolute measurements were not possible (purple).

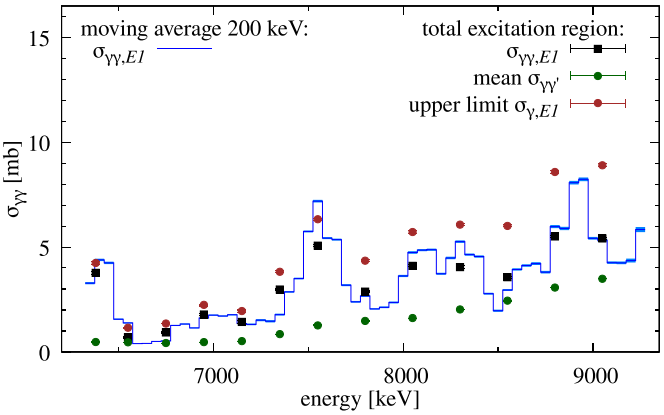

FIG. 7. The comparison of the average elastic cross section $\sigma_{\gamma\gamma,E1}$ with respect to the $E1$ channel is shown, extracted in 50 keV steps in terms of the moving average over an energy range of 200 keV (blue histogram) and from the investigation of the total excitation-energy region at once (black points). Additionally, the average inelastic cross sections $\sigma_{\gamma\gamma'}$, which include $E1$ and $M1$ transitions, are illustrated in dark green. The corresponding upper limit for the photoabsorption cross section $\sigma_{\gamma,E1}$ was calculated (brown). Only statistical uncertainties are included. For details, see text.

quantified for $E1$ ($M1$) transitions for the $E1$ ($M1$) detector, but no correction could be determined for the other radiation character. Therefore, it was only applied to the corresponding term in the individual linear equation. However, for the other radiation character, i.e., the $M1$ ($E1$) channel recorded by the detector perpendicular (parallel) to the polarization plane, no correction factor could be determined and applied.

The linear equations were solved for all combinations of photon flux and peak area extracted in the previous steps. For the determination of elastic cross sections and their corresponding statistical and systematic uncertainties, the same procedure used for the energy-integrated cross section was applied.

Because of some rest gas present in the beam line during the measurements at $E_{\text{beam}} = 5.86$ MeV and $E_{\text{beam}} = 6.15$ MeV, the deconvoluted deexcitation spectra contained, even after the deconvolution, events not resulting from NRF reactions in the target. Hence, these two energy runs were neglected in this part of the analysis.

In panel (a) of Fig. 6, the $M1$ and the $E1$ average elastic cross sections in terms of moving averages over a range of 200 keV are displayed in orange and blue, respectively. Furthermore, the fraction of the $E1$ contribution normalized to the sum of $E1$ and $M1$ elastic cross sections is given in panel (b) of Fig. 6. The calculation of this ratio has the advantage that systematic uncertainties are eliminated. Additionally, it could also be determined for the beam-energy settings of 9.3 and 9.6 MeV where the photon-current densities are unknown (purple data in Fig. 6). The 10 MeV deexcitation spectra recorded by the HPGe detectors do not show any strength and, therefore, no results are given. It can be observed that the $M1$ channel is weak compared to the $E1$ channel for all energies, except between 7.5 and 8.5 MeV. In this energy region, the $M1$ channel contributes more to the average elastic cross section and the strengths of both channels are partly comparable. Above 8.5 MeV, the $M1$ contribution drops again. This is indicated in panel (b) of Fig. 6 as well.

To determine the average inelastic cross section $\sigma_{\gamma\gamma'}$, the ground-state transitions of the 2^+_1 state at 1346 keV, the 2^+ levels at 3154 and 3275 keV, and of a state at 2972 keV, whose spin-parity quantum number is given as $(1, 2^+)$, were investigated [50]. By applying Eq. (7), extracting the peak areas $A(2^+)$ of the ground-state decays of the low-lying 2^+ states from the deexcitation spectra of each HPGe detector individually, and assuming $\overline{W_{\Pi L}(\theta, \phi)} \approx 1$, the average inelastic cross sections $\sigma_{\gamma\gamma'}$ were calculated. The investigation using all HPGe detectors accounts for systematic uncertainties introduced by, e.g., detection efficiencies at low γ-ray energies or not completely isotropic angular distributions. For the uncertainty estimate, the Monte Carlo approach was used by combining each extracted photon-current density (as explained above) with the peak areas $A(2^+)$, which were varied within their statistical uncertainties following a Gaussian distribution. The determination of uncertainties was performed in analogy to the procedure described before for the elastic cross section. Additionally, the contribution from the extraction of the inelastic cross section using the different HPGe detectors was included.

The results serve only as estimate of the average inelastic cross sections since the nonconstant photon distribution could not be taken into account. Therefore, the photon-current densities were integrated over the total excitation-energy region. The sums of the average inelastic cross sections corresponding to all observed ground-state decays of the low-lying 2^+ states are presented in dark green in Fig. 7.

In addition, Fig. 7 illustrates the comparison of the average elastic cross sections corresponding to the $E1$ channel,

extracted in $\delta E = 50$ keV steps in terms of the moving average over a range of 200 keV (blue data), and from the investigation of the complete excitation-energy region at once $\delta E = E_{\text{beam,total}}$ (black squares). The general trends of the average elastic cross sections $\sigma_{\gamma\gamma,E1}$ determined using both methods are in good agreement although the fine structure of the strength is, of course, better described by the continuous analysis in 50 keV steps. Because of this agreement, it was concluded that the average inelastic cross section can be estimated by using the determined $\sigma_{\gamma\gamma'}$ values: In Fig. 7, the sums of the average elastic $E1$ cross sections $\sigma_{\gamma\gamma,E1}$ and the average inelastic cross sections $\sigma_{\gamma\gamma'}$ are illustrated in brown, i.e., the total photoabsorption cross section $\sigma_{\gamma,E1}$ is displayed. Because $\sigma_{\gamma\gamma'}$ includes the $E1$ and $M1$ channels, the depicted photoabsorption cross sections $\sigma_{\gamma,E1}$ provide only an upper limit. Nevertheless, the importance of including the inelastic-decay channel at high excitation energies can be seen.

V. DISCUSSION

In this section, the experimental results are compared to theory. Here, the $E1$ response contained in elastic transitions is compared to calculations performed within the relativistic equation of motion (REOM) framework. This is part of the relativistic nuclear field theory (RNFT) that represents the most optimal balance of fundamentality, predictive power, and feasibility for nuclear structure calculations. The apparent advantages of RNFT are its covariance, connection to particle physics, nonperturbative character, and transparent treatment of subleading contributions to the nucleon-nucleon forces in complex nuclei. The only input to RNFT is the meson masses and coupling constants, slightly renormalized in the framework of the covariant density functional theory, compared to their vacuum values and universal across the nuclear chart. Up to now, the REOM has not been adopted for calculations of nuclear response of unnatural parity in the neutral sector. Therefore, shell-model calculations were performed to interpret the $M1$ strength of individual transitions of ^{64}Ni observed in the experimental data. The shell-model approach is capable of providing accurate treatment of complex multiparticle-multihole configurations in sufficiently small model spaces, that is, the case of the $M1$ response. However, it is more difficult to extend to model spaces covering two major shells required for the $E1$ excitations in the energy interval under study.

The most important details concerning both calculations are given below.

A. Relativistic equation of motion approach

The most convenient tool to quantify the nuclear strength functions over a wide range of energies is response theory. In major textbooks and many practical applications, response theory is confined by the random phase approximation (RPA) or its superfluid variant, the quasiparticle RPA (QRPA). In the context of the most fundamental *ab initio* equation of motion (EOM) framework [51,52], QRPA neglects completely the dynamical interaction kernel, while in the diagrammatic formulation, (Q)RPA is associated with a one-loop approximation. In Rowe's EOM [53], (Q)RPA is represented by the simplest one-particle–one-hole (two-quasiparticle) 1p1h (2q) excitation operator generating the excited states by its action on a noncorrelated ground state, while more accurate solutions require higher-complexity ($npnh$) correlations in both the excited and ground states of the system.

(Q)RPA is known to reproduce some basic features of giant resonances and soft modes. However, a detailed and accurate description of nuclear spectra requires a much more advanced theory. All the approximations beyond (Q)RPA were shown to be derivable from the dynamical kernel of the *ab initio* EOM for the two-fermion response function [54,55]. In particular, the leading approximation beyond (Q)RPA is the quasiparticle-vibration coupling (qPVC) in the minimal coupling scheme including $2q \otimes 1$phonon configurations in the two-fermion in-medium propagator, where the phonon represents correlated $2q$ pairs. Realistic implementations of this approach may employ effective interactions, which yield quite reasonable phonons already within (Q)RPA, combined with subtraction restoring the self-consistency of the *ab initio* framework [56]. The minimal qPVC extension of (Q)RPA by the $2q \otimes 1$phonon configurations is often insufficient, and higher configuration complexity may be needed to describe fine details of nuclear spectra. The two-fermionic cluster decomposition of the fully correlated dynamical kernel of the response function suggests that the next-level complexity nonperturbative approximation is the $2q \otimes 2$phonon or correlated six-quasiparticle configurations in the intermediate propagators.

Based on the recent developments of Refs. [54,55], calculations for the electromagnetic dipole response of ^{64}Ni were performed with the NL3* meson-exchange interaction [57]. This parametrization (an upgrade of NL3) demonstrates a reliable performance in the description of nuclear masses and radii [58]. Furthermore, the NL3* has the advantage of its ansatz being separable in the momentum representation, which allows for an economical and efficient implementation for calculations of the nuclear response.

The calculations were conducted in the three many-body approximations of growing complexity: relativistic QRPA (RQRPA), relativistic $2q \otimes 1$phonon EOM (REOM^2) and relativistic $2q \otimes 2$phonon EOM (REOM^3). The upper index in REOM^n is adopted as a universal complexity index, marking the maximal number of correlated or noncorrelated particle-hole configurations in the intermediate propagators: 2p2h for REOM^2 and 3p3h for REOM^3. Natural-parity phonons up to 20 MeV with $J = [1, 6]$ were used in both REOM^2 and REOM^3, and the intermediate $2q \otimes 1$phonon propagators with both parities and $J = [0, 6]$ were included in the model space of REOM^3. The $2q$ configurations were included up to 100 MeV, while the $2q \otimes 1$phonon ones were accommodated up to 30 MeV. Including $2q \otimes 2$phonon configurations up to high energy is technically challenging, and the energy cutoff of 25 MeV was the maximum that is feasible on the supercomputer cluster at Western Michigan University. Further details are similar to those of calculations presented in Ref. [59].

REOM^2, previously dubbed as relativistic (quasiparticle) time blocking approximation [R(Q)TBA], brings a major

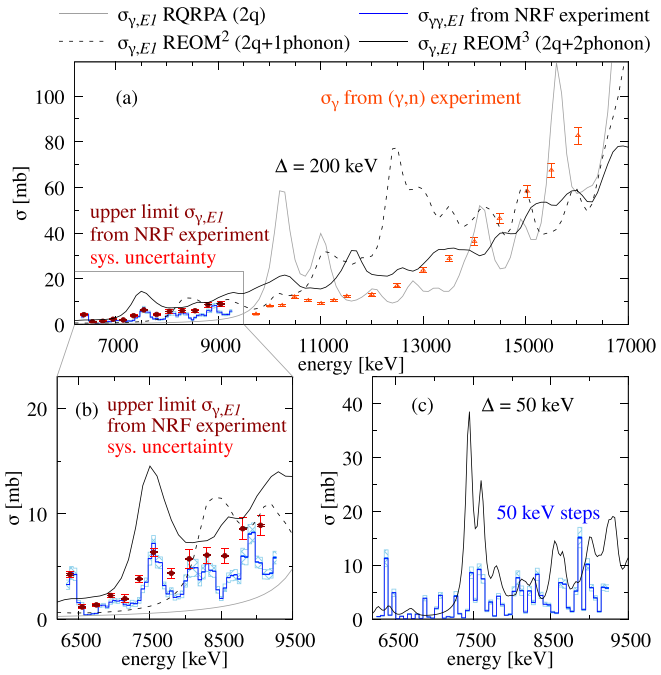

FIG. 8. (a) The $E1$ photoabsorption cross section $\sigma_{\gamma,E1}$ of ^{64}Ni in the three many-body approximations of growing complexity: relativistic QRPA (RQRPA) (gray), relativistic $2q \otimes 1$phonon EOM (REOM^2) (dashed black), and relativistic $2q \otimes 2$phonon EOM (REOM^3) (solid black). The results up to 17 MeV were obtained with the $\Delta = 200$ keV smearing parameter (the imaginary part of the energy argument and corresponding to half the width of the individual peaks) in comparison with the experimental NRF elastic cross section $\sigma_{\gamma\gamma,E1}$ (blue). These data are depicted as moving averages over a range of 200 keV. The statistical (systematic) uncertainties are shown as blue shaded (light-blue crosshatched) areas. Furthermore, the upper limits for the $E1$ photoabsorption cross sections $\sigma_{\gamma,E1}$, which also include the average inelastic cross sections, and the statistical uncertainties determined in the NRF experiment are depicted as dark-red points. The corresponding systematic uncertainties are illustrated as light-red error bars. Additionally, the total photoabsorption cross section σ_γ extracted from a (γ,n) measurement by Utsonomiya *et al.* (orange triangles) [60] are given. (b) The same data as in (a) but just up to 9500 keV to emphasize the energy region associated with the PDR. (c) For a better comparison of the fine structure observed in the NRF experiment with the REOM^3 calculation, the experimental results extracted in 50 keV steps are illustrated together with the REOM^3 results obtained with a smearing parameter of $\Delta = 50$ keV.

refinement and significant improvement of the description as compared to RQRPA, as displayed in panels (a) and (b) of Fig. 8. However, it can be observed that more complex configurations than $2q \otimes 1$phonon are needed for a more accurate description of the experimental data. By adding more complex $2q \otimes 2$phonon configurations in REOM^3 the strength distribution is still visibly changed. It can be seen that a significant portion of the strength moves toward lower energies. In particular, the pygmy-resonance domain below 10 MeV manifests considerable structural differences between the REOM^2 and REOM^3 approaches [cf. panel (b) of Fig. 8]. On the theory side, the model-independent framework [54,61] indicates that, in principle, configurations up to NpNh complexity have to be included to solve the many-body problem of N particles exactly. Therefore, any effort toward high-complexity configurations should improve the description of a many-body system. However, a comparison of the RQRPA, REOM^2, and REOM^3 numerical results indicates that the quantitative importance of complex configurations decreases with complexity. Hence, it can be assumed that reaching the desired accuracy is feasible within the model spaces of maximal complexity not significantly exceeding $2q \otimes 2$phonon in the coupling regimes of nuclear structure.

The theoretical results given in Fig. 8 represent the total $E1$ photoabsorption cross sections $\sigma_{\gamma,E1}$. The average $E1$ elastic cross sections $\sigma_{\gamma\gamma,E1}$ deduced from the NRF measurements are displayed in blue. The experimental upper limits of the $E1$ photoabsorption cross section shown in dark red include the inelastic decay channel for which no distinction between $E1$ and $M1$ transitions was possible, as described in the previous section. Hence, these results represent upper limits with respect to the $E1$ channel. In the case of the photoabsorption cross section deduced from the (γ,n) experiment (orange), also the $M1$ channel is included, but it was theoretically shown in Ref. [60] that this contribution is negligible above approximately 10.5 MeV. Because no absolute cross sections could be determined between 9.3 MeV and S_n in this NRF measurement, a conclusive comparison of the NRF and the (γ,n) data is not possible. However, there are indications of additional $E1$ strength and structures on top of the low-energy tail of the IVGDR in the PDR region.

Whereas the RQRPA and the REOM^2 results do not show strength distributions comparable to the NRF data, the REOM^3 results reproduce the experimentally-determined enhancement of the cross section at 7.5 MeV. Furthermore, when comparing the REOM^3 cross sections obtained with a 50 keV smearing parameter and the average elastic cross sections deduced in 50 keV steps [panel (c)], a good agreement in the strength fragmentation can be observed up to 8.5 MeV. At higher energies, the energies of the enhancements cannot exactly be reproduced but similar structures can be identified. Here, the inelastic contribution is not included since it could not be extracted in 50 keV steps and, therefore, no fine structure could be investigated.

The agreement of REOM^3 with experimental data, although improved compared to the less advanced approaches, is still imperfect. Especially, the summed cross section between 6.0 and 9.3 MeV is almost two times higher than the experimentally extracted upper limit of the total photoabsorption cross section (dark-red data points) as illustrated in Fig. 9. This indicates that some mechanisms of the strength formation are still to be included to achieve spectroscopic accuracy, and that the interaction can be of better quality. In the paradigm of a parameter-free many-body theory, the only parameters are those characterizing the local interaction between two nucleons (effective or bare), while all the many-body correlations are computed without changing these parameters or introducing new ones.

Within this paradigm, a complete response theory for atomic nuclei should take into account the continuum, including the multiparticle escape, a more complete set of

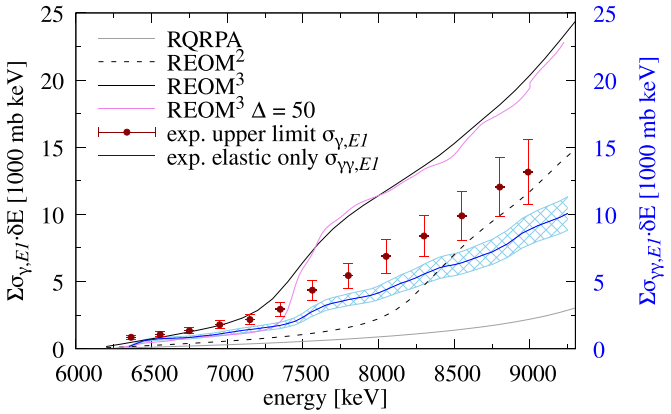

FIG. 9. The running sums of the $E1$ photoabsorption cross sections $\Sigma\sigma_{\gamma,E1}$ of ^{64}Ni deduced from RQRPA (gray), REOM^2 (dashed black), and REOM^3 calculations are depicted. In the case of the REOM^3, the result using a smearing parameter of $\Delta = 200$ keV is shown as a black solid curve, and the $\Delta = 50$ keV calculation as a purple solid one. The running sums of the experimentally deduced upper limit for the total photoabsorption cross section of the $E1$ contribution and the corresponding statistical uncertainties are depicted in dark red. The systematic uncertainties are shown in lighter red. The running sum of the experimental NRF elastic cross section $\sigma_{\gamma\gamma,E1}$ is illustrated in blue (systematic uncertainties as light-blue crosshatched areas) with the corresponding y axis on the right side.

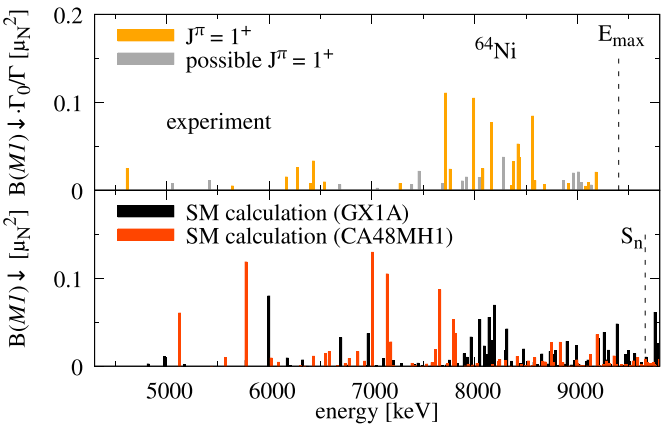

FIG. 10. Upper panel: The products of experimental $B(M1, 1^+ \to 0_1^+)$ and the ground-state decay branching ratio Γ_0/Γ are illustrated for all firmly identified $M1$ transitions as orange bars and for all transitions with unknown radiation character as gray bars. The maximum energy, for which absolute values could experimentally be determined, is indicated by a dashed vertical line. Lower panel: $B(M1, 1^+ \to 0_1^+)$ values for the lowest 100 1^+ states deduced by the shell-model calculations using, on the one hand, the CA48MH1 Hamiltonian and, on the other, the GX1A Hamiltonian are shown as red and black bars, respectively. Here, the neutron-separation threshold of ^{64}Ni is indicated by a dashed vertical line.

phonons (including those of unnatural parity and isospin-flip), complex ground-state correlations, and, in principle, even higher-complexity configurations, which are expected to further affect the strength functions and potentially improve the description of the fine structure. These factors may be individually less significant than the included correlations but altogether they can make a sizable contribution. These effects will be addressed in future work.

For a better comparison, the contribution of the inelastic-decay channel in the experiment has to be further investigated with respect to the contributions of $E1$ and $M1$ transitions. Furthermore, the deduced average inelastic cross sections serve only as an estimate of the inelastic-decay channel, since the nonconstant photon-current densities were neglected in the analysis. By analyzing γ-γ coincidence data, a smaller energy region δE can be investigated, similar to that used for the average elastic cross section.

B. Shell-model calculations

Shell-model calculations for ^{64}Ni were carried out using the code NUSHELLX@MSU [62] with two different model spaces.

First, the fp model space with the GX1A Hamiltonian [63,64] was used as previously for the lighter nuclide ^{54}Fe [19]. The model space included the proton and neutron orbitals $(1f_{7/2}, 2p_{3/2}, 1f_{5/2}, 2p_{1/2})$ without limits in occupation numbers. The calculated 2_1^+ state has an excitation energy of $E_x = 1.268$ MeV and a transition strength to the ground state of $B(E2, 2_1^+ \to 0_1^+) = 139\ e^2\text{fm}^4$. The corresponding experimental values are $E_x = 1.346$ MeV and $B(E2, 2_1^+ \to 0_1^+) = 119(4)\ e^2\text{fm}^4$ [50].

As an alternative, the ca48pn model space with the CA48MH1 Hamiltonian [65,66] was applied, which had also been used for the investigation of 1^+ states in the isotone ^{66}Zn [24] and in ^{60,64,68}Fe [67]. The model space included the $\pi(1f_{7/2}^{(8-f)}, 1f_{5/2}^{f}, 2p_{3/2}^{f}, 2p_{1/2}^{p1})$ proton orbitals with $f = 0$ to 4, $p1 = 0$ to 2, and the $\nu(1f_{5/2}^{f5}, 2p_{3/2}^{p3}, 2p_{1/2}^{p1}, 1g_{9/2}^{g9})$ neutron orbitals, where $f5$ and $p3$ can have values from zero to the respective maximum, and $g9 = 0$ to 2. The 2_1^+ state was calculated at $E_x = 0.750$ MeV with a transition strength of $B(E2, 2_1^+ \to 0_1^+) = 423\ e^2\text{fm}^4$ using standard effective charges of $e_\pi = 1.5e$ and $e_\nu = 0.5e$. It is noted that the Hamiltonians were not specifically adjusted to nuclides around ^{64}Ni. The calculations for $J^\pi = 1^+$ states were performed for the lowest 100 states. Reduced transition strengths $B(M1, 1^+ \to 0_1^+)$ were calculated using effective g factors of $g_s^{\text{eff}} = 0.74 g_s^{\text{free}}$ [68].

The experimentally deduced products of $B(M1, 1^+ \to 0_1^+)$ and the ground-state decay branching ratio Γ_0/Γ given in Table I for all firm and possible 1^+ states are compared with the calculated ones in Fig. 10. The first 1^+ state in the shell-model calculation using the CA48MH1 (GX1A) Hamiltonian appears at 2.941 (2.692) MeV, whereas the first experimental state with a firm 1^+ assignment is located at 4.617(1) MeV. However, excitation energies below 4.33 MeV were not covered by the HIγS measurement. Therefore, the lowest-lying calculated 1^+ states within the shell model are not given in the figure.

Around 8 MeV, an accumulation of strong $M1$ transitions and a number of transitions with smaller $B(M1)$ values

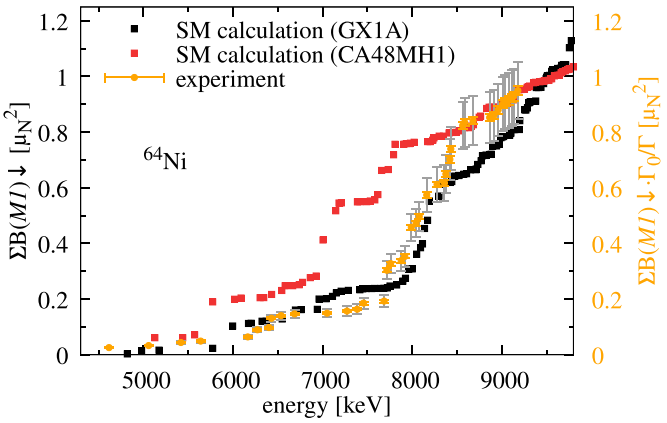

FIG. 11. Running sums $\sum B(M1, 1^+ \rightarrow 0_1^+)$ of the calculated values using the CA48MH1 and GX1A Hamiltonians are shown as red and black squares, respectively. The experimentally extracted products of $B(M1, 1^+ \rightarrow 0_1^+)$ and ground-state decay branching ratio Γ_0/Γ (right y axis) of ^{64}Ni are given by orange circles with the corresponding statistical uncertainties. The systematic uncertainties are depicted in gray.

above 8.5 MeV are observed in the experiment (upper part of Fig. 10). This resembles the distribution calculated with the GX1A Hamiltonian (black bars in the lower panel). The shell-model results obtained with the CA48MH1 Hamiltonian show prominent strengths between 7 and 7.5 MeV and also a distribution of smaller strengths at higher energy (red bars in the lower panel). This behavior is also indicated in the running sums calculated using all values above 4 MeV determined theoretically and experimentally (cf. Fig. 11). The experimental running sum includes all firmly assigned as well as all possible $M1$ transitions observed in the NRF experiments. All the curves indicate a steplike behavior caused by strong peaks in the $B(M1)$ distributions. Whereas the steepest step occurs between 7.5 and 8 MeV in the experimental (orange) and the GX1A (black) data, the CA48MH1 results (red) contain two steep steps at 7 and 7.5 MeV. Because of these two steps, the running sums in CA48MH1 exceed the experimental ones as well as those calculated in GX1A above 7 MeV, but approach the experimental values again at 8.5 MeV. Additionally, it is indicated that the strength in the GX1A shell-model calculations is more smoothly distributed compared to the experimental strength between approximately 8.5 and 9.5 MeV. The differences between the distributions of $M1$ strength obtained with the two model spaces may be traced back to differences in the ingredients, such as single-particle energies and two-body matrix elements. The calculation using GX1A without limitations reproduces the energy of the 2_1^+ state and the $B(E2, 2_1^+ \rightarrow 0_1^+)$ value better than the one using CA48MH1, which may indicate a better adjustment of model space and Hamiltonian to the present nuclide. In both model spaces, the excitation of protons from the $1f_{7/2}$ orbital to the fp orbitals across the $Z = 28$ gap plays an important role for the generation of $M1$ strength. In GX1A, also the neutron $1f_{7/2}$ orbital is included while CA48MH1 starts above $N = 28$, but includes the $1g_{9/2}$ orbital in addition. Both these orbitals give minor contributions to the respective calculated states, but may nevertheless influence the results in different ways.

It has to be kept in mind that the experimental data are given as the product of the reduced transition strength and the ground-state decay branching ratio. In this sense, the pictured experimental values serve only as upper limit. On the other hand, only resolved transitions are contained in the experimental data.

It can be concluded that the experimental summed strength of $\Sigma B(M1, 1^+ \rightarrow 0_1^+) = 0.949(16)(102)\mu_N^2$ between 4.3 and 9.3 MeV is well reproduced by both shell-model calculations which amount to $\Sigma B(M1, 1^+ \rightarrow 0_1^+) = 0.96\mu_N^2$ using the CA48MH1 Hamiltonian and to $\Sigma B(M1, 1^+ \rightarrow 0_1^+) = 0.89\mu_N^2$ with the GX1A Hamiltonian. The summed strength is very similar to that of the neutron-magic ($N = 28$) ^{54}Fe [19] and almost three times larger than that of the $N = 36$ isotone ^{66}Zn [24] up to 9.3 MeV. This increase is expected because proton excitations across $Z = 28$ play an important role for $M1$ excitations of ^{64}Ni, whereas this contribution is small for ^{66}Zn, which already has two protons above the $Z = 28$ shell closure.

VI. SUMMARY AND OUTLOOK

Real-photon scattering experiments on ^{64}Ni were performed using both an energetically continuous, mainly unpolarized (bremsstrahlung) photon beam and a quasimonoenergetic, linearly polarized γ-ray beam. This combination enabled the firm (tentative) identification of 87 (8) $E1$, 23 (2) $M1$, and 11 dipole transitions of unknown radiation character between 4.3 and 9.7 MeV. For 11 observed transitions, neither the multipole order nor the radiation character could be firmly assigned. Because of the use of a calibration standard during the bremsstrahlung experiment, absolute energy-integrated cross sections of transitions up to 9.3 MeV were deduced by combining both experiments. In addition to the analysis of individual transitions, average elastic cross sections $\sigma_{\gamma\gamma}$ were determined up to 9.2 MeV. The contributions of the $E1$ and $M1$ channel with respect to the total elastic cross section were calculated up to the neutron-separation energy $S_n = 9.7$ MeV of ^{64}Ni. It was observed that the $E1$ contribution is, in general, larger than the $M1$ contribution although an accumulation of $M1$ transitions was observed between 7.5 and 8.5 MeV.

Shell-model calculations were performed using two different Hamiltonians (CA48MH1 and GX1A). The resulting reduced $M1$ transition strengths $B(M1, 1^+ \rightarrow 0_1^+)$ were compared to the experimentally deduced products of reduced transition strength and ground-state decay branching ratio $B(M1, 1^+ \rightarrow 0_1^+) \times \Gamma_0/\Gamma$ of individual transitions. Although the agreement of the summed strength between 4.3 and 9.3 MeV is good for both calculations with respect to the experimental value, the fine structure, i.e., an accumulation of strength between 7.5 and 8.5 MeV, is better reproduced by the shell-model calculation carried out in the fp model space with the GX1A Hamiltonian. The experimental summed strength is very similar to that of the neutron-magic $N = 28$ nucleus ^{54}Fe [19] and almost three times larger than that of the $N = 36$ isotone ^{66}Zn [24] up to 9.3 MeV. Also, the calculated $M1$ strength of ^{64}Ni exceeds the one of ^{66}Zn by about 50%. Large

$M1$ strengths are attributed to proton excitations across the $Z = 28$ gap, including holes in the $1f_{7/2}$ orbital. These play an important role for excited 1^+ states of ^{64}Ni, whereas their contributions to states of ^{66}Zn, which already has two protons above the $Z = 28$ shell closure, are smaller.

The average elastic cross section of the $E1$ channel and an upper limit of the total photoabsorption cross section, including decays to states other than the ground state, were compared to calculations in the relativistic equation of motion REOM framework including $2q \otimes$ 1phonon REOM^2 and $2q \otimes$ 2phonon REOM^3 configurations. It was found that the inclusion of more complex configurations leads to a lowering of the energy of a significant part of the $E1$ strength. The $E1$ part of the photoabsorption cross sections $\sigma_{\gamma,E1}$ extracted from the calculations were compared to the NRF results. It was observed that the REOM^3 calculation describes the gross structures of the average elastic cross section well, i.e., enhancements of the cross section up to approximately 8.5 MeV. At higher energies, the energies of the enhancements are not as well described, but nevertheless, similar structures can be observed. Besides the good reproduction of the cross section's behavior, the absolute value of the REOM^3 calculation is approximately two times larger than the experimental value. Possible reasons for this discrepancy can be found on both the experimental and theoretical sides. On the one hand, for the estimate of the average inelastic cross section, the nonconstant photon distribution was neglected. This can be taken into account by investigating γ-γ coincidence data, and extracting the inelastic cross section in smaller energy steps than it was done for the elastic cross section. On the other hand, more mechanisms contributing to the strength formation have to be included in the theory for a better description of the experimental data.

For both radiation characters, the missing exact knowledge of the inelastic decay channel makes comparisons to theory difficult. Furthermore, a remeasurement at energies between 9.3 MeV and S_n is important for conclusive comparisons to, e.g., the (γ,n) data by Utsonomiya *et al.* [60] with respect to a possible enhancement of $E1$ strength on top of the low-energy tail of the IVGDR in the PDR region.

ACKNOWLEDGMENTS

The authors thank the accelerator staff at HIγS and γELBE for providing excellent photon beams and A. Hartmann for the technical assistence. The work of E.L. was supported by the GANIL Visitor Program, US-NSF Grant No. PHY-2209376, and US-NSF Career Grant No. PHY-1654379. R.S. thanks B. A. Brown for his support in using the code NUSHELLX@MSU and gratefully acknowledges the allocation of computing time through the Centers for High-Performance Computing of Helmholtz-Zentrum Dresden-Rossendorf and of Technische Universität Dresden. The members of the UWS Nuclear Physics Research Group acknowledge financial support from the UK Science and Technology Facilities Council (STFC, Grant No. ST/P005101/1). This work was supported in part by the U.S. Department of Energy, Office of Nuclear Physics under Grants No. DE-FG02-97ER41033 (Duke University) and No. DE-FG02-97ER41041 (UNC). J.I. and O.P. are supported by the Deutsche Forschungsgemeinschaft (DFG, German Research Foundation), Project ID No. 279384907-SFB1245, and by the grant "Nuclear Photonics" within the LOEWE program of the State of Hesse. J.I. acknowledges the support by the State of Hesse within the Research Cluster ELEMENTS (Project ID No. 500/10.006). This work was supported by the BMBF (05P21PKEN9).

[1] M. Harakeh and A. van der Woude, *Giant Resonances* (Oxford University Press, Oxford, 2001).
[2] D. Savran, T. Aumann, and A. Zilges, Prog. Part. Nucl. Phys. **70**, 210 (2013).
[3] A. Bracco, E. Lanza, and A. Tamii, Prog. Part. Nucl. Phys. **106**, 360 (2019).
[4] E. Lanza, L. Pellegri, A. Vitturi, and M. Andrés, Prog. Part. Nucl. Phys. **129**, 104006 (2023).
[5] D. Savran, M. Fritzsche, J. Hasper, K. Lindenberg, S. Müller, V. Y. Ponomarev, K. Sonnabend, and A. Zilges, Phys. Rev. Lett. **100**, 232501 (2008).
[6] A. P. Tonchev, S. L. Hammond, J. H. Kelley, E. Kwan, H. Lenske, G. Rusev, W. Tornow, and N. Tsoneva, Phys. Rev. Lett. **104**, 072501 (2010).
[7] R.-D. Herzberg *et al.*, Phys. Lett. B **390**, 49 (1997).
[8] B. Löher *et al.*, Phys. Lett. B **756**, 72 (2016).
[9] A. Zilges, S. Volz, M. Babilon, and P. Mohr, Phys. Lett. B **542**, 43 (2002).
[10] S. Volz, N. Tsoneva, M. Babilon, and M. Elvers, Nucl. Phys. A **779**, 1 (2006).
[11] D. Savran *et al.*, Phys. Rev. C **84**, 024326 (2011).
[12] K. Govaert, F. Bauwens, J. Bryssinck, D. De Frenne, E. Jacobs, W. Mondelaers, L. Govor, and V. Y. Ponomarev, Phys. Rev. C **57**, 2229 (1998).
[13] F. Schlüter (private communication).
[14] J. Endres *et al.*, Phys. Rev. C **85**, 064331 (2012).
[15] B. Özel-Tashenov *et al.*, Phys. Rev. C **90**, 024304 (2014).
[16] M. Müscher *et al.*, Phys. Rev. C **102**, 014317 (2020).
[17] M. Weinert, M. Spieker, G. Potel, N. Tsoneva, M. Müscher, J. Wilhelmy, and A. Zilges, Phys. Rev. Lett. **127**, 242501 (2021).
[18] D. Savran *et al.*, Phys. Lett. B **786**, 16 (2018).
[19] R. Schwengner *et al.*, Phys. Rev. C **101**, 064303 (2020).
[20] T. Shizuma, T. Hayakawa, H. Ohgaki, H. Toyokawa, T. Komatsubara, N. Kikuzawa, T. Inakura, M. Honma, and H. Nakada, Phys. Rev. C **87**, 024301 (2013).
[21] F. Bauwens, J. Bryssinck, D. De Frenne, K. Govaert, L. Govor, M. Hagemann, J. Heyse, E. Jacobs, W. Mondelaers, and V. Y. Ponomarev, Phys. Rev. C **62**, 024302 (2000).
[22] M. Scheck *et al.*, Phys. Rev. C **87**, 051304(R) (2013).
[23] M. Scheck *et al.*, Phys. Rev. C **88**, 044304 (2013).
[24] R. Schwengner *et al.*, Phys. Rev. C **103**, 024312 (2021).
[25] D. Savran *et al.*, Phys. Rev. C **106**, 044324 (2022).
[26] F. R. Metzger, Prog. Nucl. Phys. **7**, 53 (1959).
[27] U. Kneissl, H. Pitz, and A. Zilges, Prog. Part. Nucl. Phys. **37**, 349 (1996).

[28] A. Zilges, D. Balabanski, J. Isaak, and N. Pietralla, Prog. Part. Nucl. Phys. **122**, 103903 (2022).
[29] N. Pietralla *et al.*, Phys. Rev. Lett. **88**, 012502 (2001).
[30] C. Romig *et al.*, Phys. Rev. C **88**, 044331 (2013).
[31] J. Isaak *et al.*, Phys. Lett. B **727**, 361 (2013).
[32] R. Schwengner *et al.*, Nucl. Instrum. Methods Phys. Res., Sect. A **555**, 211 (2005).
[33] H. R. Weller, M. W. Ahmed, H. Gao, W. Tornow, Y. K. Wu, M. Gai, and R. Miskimen, Prog. Part. Nucl. Phys. **62**, 257 (2009).
[34] B. Löher *et al.*, Nucl. Instrum. Methods Phys. Res., Sect. A **723**, 136 (2013).
[35] S. Agostinelli *et al.*, Nucl. Instrum. Methods Phys. Res., Sect. A **506**, 250 (2003).
[36] J. Allison *et al.*, IEEE Trans. Nucl. Sci. **53**, 270 (2006).
[37] J. Allison *et al.*, Nucl. Instrum. Methods Phys. Res., Sect. A **835**, 186 (2016).
[38] R. Massarczyk *et al.*, Phys. Rev. C **86**, 014319 (2012).
[39] U. Friman-Gayer, J. Kleeman, and O. Papst (2022), https://github.com/uga-uga/utr.
[40] E. Haug, Radiat. Phys. Chem. **77**, 207 (2008).
[41] G. Roche, C. Ducos, and J. Proriol, Phys. Rev. A **5**, 2403 (1972).
[42] F. Salvat, J. D. Martnez, R. Mayol, and J. Parellada, Phys. Rev. A **36**, 467 (1987).
[43] F. Ajzenberg-Selove, Nucl. Phys. A **506**, 1 (1990).
[44] G. Rusev, A. P. Tonchev, R. Schwengner, C. Sun, W. Tornow, and Y. K. Wu, Phys. Rev. C **79**, 047601 (2009).
[45] J. Isaak *et al.*, Phys. Rev. C **103**, 044317 (2021).
[46] U. Friman-Gayer, J. Kleeman, and O. Papst (2022), https://github.com/uga-uga/Horst.
[47] Y. Wu (private communication).
[48] C. Sun and Y. K. Wu, Phys. Rev. ST Accel. Beams **14**, 044701 (2011).
[49] M. Tamkas *et al.*, Nucl. Phys. A **987**, 79 (2019).
[50] B. Singh and J. Chen, Nucl. Data Sheets **178**, 41 (2021).
[51] S. Adachi and P. Schuck, Nucl. Phys. A **496**, 485 (1989).
[52] J. Dukelsky, G. Röpke, and P. Schuck, Nucl. Phys. A **628**, 17 (1998).
[53] D. J. Rowe, Rev. Mod. Phys. **40**, 153 (1968).
[54] E. Litvinova and P. Schuck, Phys. Rev. C **100**, 064320 (2019).
[55] E. Litvinova and Y. Zhang, Phys. Rev. C **106**, 064316 (2022).
[56] V. I. Tselyaev, Phys. Rev. C **88**, 054301 (2013).
[57] G. Lalazissis, S. Karatzikos, R. Fossion, D. P. Arteaga, A. Afanasjev, and P. Ring, Phys. Lett. B **671**, 36 (2009).
[58] S. E. Agbemava, A. V. Afanasjev, D. Ray, and P. Ring, Phys. Rev. C **89**, 054320 (2014).
[59] E. Litvinova, arXiv:2308.07574.
[60] H. Utsunomiya *et al.*, Phys. Rev. C **98**, 054619 (2018).
[61] M. Q. Hlatshwayo, J. Novak, and E. Litvinova, Phys. Rev. C **109**, 014306 (2024).
[62] B. A. Brown and W. Rae, Nucl. Data Sheets **120**, 115 (2014).
[63] M. Honma, T. Otsuka, B. A. Brown, and T. Mizusaki, Phys. Rev. C **69**, 034335 (2004).
[64] M. Honma, T. Otsuka, B. A. Brown, and T. Mizusaki, Eur. Phys. J. A **25**, 499 (2005).
[65] M. Hjorth-Jensen, T. T. Kuo, and E. Osnes, Phys. Rep. **261**, 125 (1995).
[66] M. Hjorth-Jensen (private communication).
[67] R. Schwengner, S. Frauendorf, and B. A. Brown, Phys. Rev. Lett. **118**, 092502 (2017).
[68] M. Honma, T. Otsuka, T. Mizusaki, M. Hjorth-Jensen, and B. A. Brown, J. Phys.: Conf. Ser. **20**, 7 (2005).

6 Results and discussion

In the beginning of this chapter, it has to be emphasized that the discussion is focused on comparisons between results obtained from different real-photon scattering experiments if not other noted. Due to the same excitation mechanism and similar limitations of the performed experiments, the results are most suited for comparisons. Nevertheless, it suffers from different experimental sensitivity limits which has to be kept in mind for some of the conclusions drawn.

For getting more insights in the underlying structures and mechanisms of the different dipole-excitation modes, studies along isotopic and isotonic chains are indispensable. The $Z = 28$ isotopic chain deals as good testing ground for investigations using real photons as probe due to its four stable, even-even isotopes ^{58,60,62,64}Ni. The two most abundant isotopes ^{58,60}Ni have already been measured using bremsstrahlung and LCB photon beams and the results are published in Refs. [55–57]. Bremsstrahlung and LCB experiments on ^{62}Ni have been conducted as well, although only the analysis of a recently-performed bremsstrahlung experiment covering an energy region up to 8.5 MeV is finalized [88]. The last missing even-even $Z = 28$ isotope, which had to be studied in (γ, γ') experiments, is ^{64}Ni. The analysis of these data was the scope of this thesis.
A compilation of the results obtained in state-to-state analyses is illustrated in Fig. 6.1. In addition to the Ni isotopes, the results of the $Z = 26$ isotopes ^{54,56}Fe [53, 54] and of the $N = 36$ isotone ^{66}Zn are shown [58]. This enables, besides the investigation of the evolution of the low-lying dipole strength with increasing neutron number, the study of the impact on the strength when crossing the magic $Z = 28$ or $N = 28$ shell closures.

The following conclusions were drawn without taking into account the results of ^{62}Ni since the radiation characters of the observed transitions were not determined in NRF experiments so far. It has to be taken into account that the data depict the energy-integrated cross sections of resolved, elastic transitions only. Furthermore, it has to be noted that, in the case of ^{54}Fe, additional $E1$ and $M1$ transitions were observed above 10 MeV which are not included in this figure.

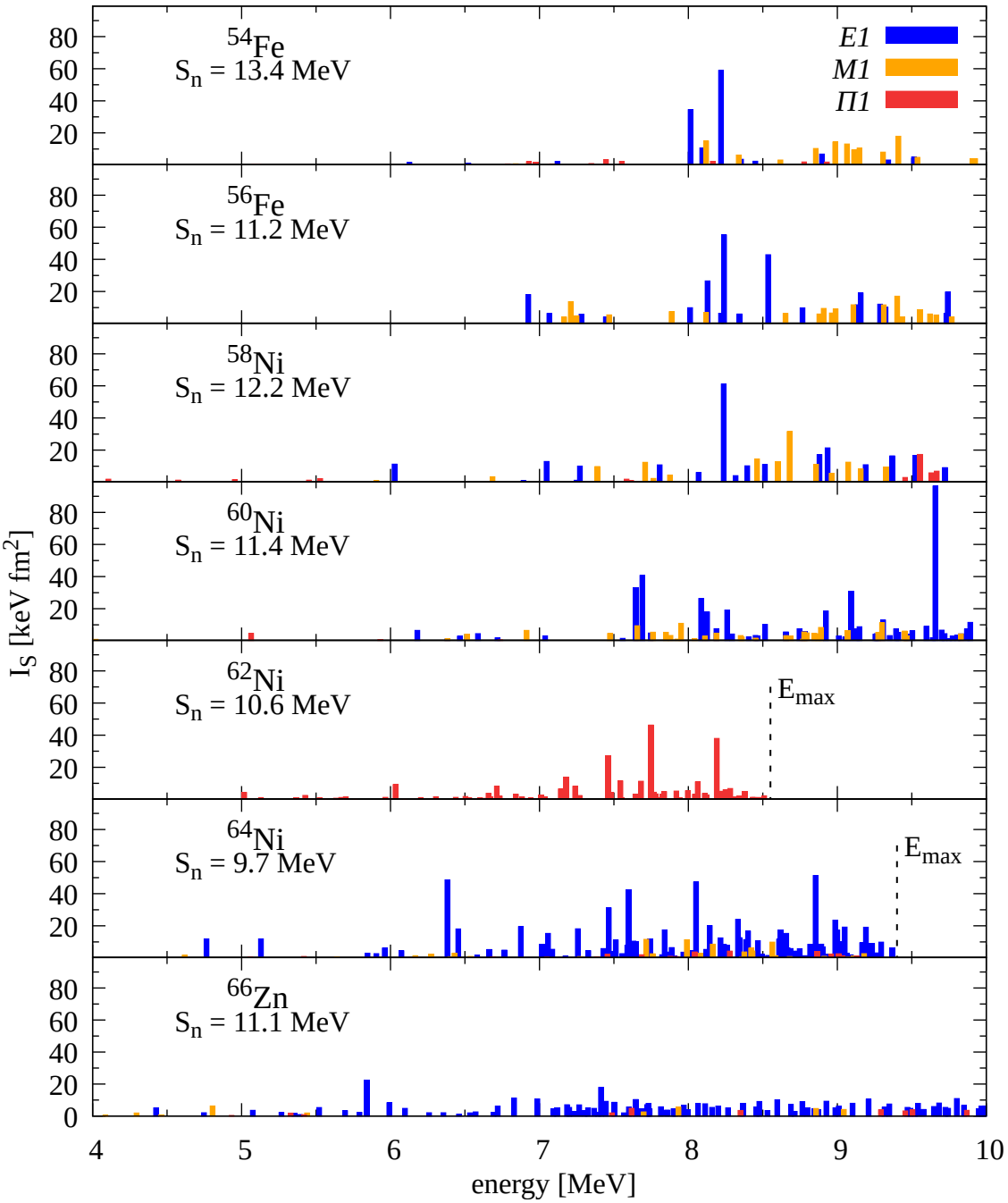

Figure 6.1: The absolute energy-integrated cross sections of ^{54,56}Fe [53, 54], ^{58,60,62,64}Ni [55–57, 88], and ^{66}Zn [58] are shown between 4 and 10 MeV. The energy-integrated cross sections of transitions firmly and tentatively characterized as $E1$ or $M1$ transition are illustrated as blue and orange bars, respectively. If no radiation character was assigned, the corresponding value is displayed as red bar.

Table 6.1: Ratios between $\sum I_S(E1)$ and $\sum I_S(M1)$ for medium-mass nuclei in the $Z \approx 28$ region, the corresponding N/Z ratios and Coulomb-Corrected Fermi energies Δ_{CCF} are given.

nucleus	N/Z	Δ_{CCF} [MeV]	$\sum I_S(E1) / \sum I_S(M1)$	up to [MeV]
$^{54}_{26}\mathrm{Fe}_{28}$	1.08	3.9	1.36(5)	11.55
$^{56}_{26}\mathrm{Fe}_{30}$	1.15	7.0	1.83(16)	9.77
$^{58}_{28}\mathrm{Ni}_{30}$	1.07	4.5	1.67(5)	9.73
$^{60}_{28}\mathrm{Ni}_{32}$	1.14	6.8	3.5(3)	9.9
$^{64}_{28}\mathrm{Ni}_{36}$	1.29	11.6	10.91(23)	9.24
$^{66}_{30}\mathrm{Zn}_{36}$	1.20	7.6	18.1(1.3)	10.06

Figure 6.1 illustrates that, in general, strong dipole transitions can be observed when investigating the $Z = 26$ iron isotopes (^{54}Fe is neutron magic $N = 28$) and the proton-magic nickel isotopes, whereas the dipole response of ^{66}Zn consists of many relatively-weak transitions. This behavior is pronounced in the $E1$ channel and will be discussed in Sec. 6.2.
Moreover, it can be observed that the ratios between $E1$ and $M1$ strengths change for the elastic-decay channel. These ratios of $\sum I_S(E1)$ and $\sum I_S(M1)$ are summarized in Table 6.1 together with the corresponding N/Z ratios and the Coulomb-Corrected Fermi energies Δ_{CCF}. The latter serves as measure for the strength of the neutron binding with respect to the proton binding and is calculated according to [19]

$$\Delta_{\mathrm{CCF}} = (S_{2p} - S_{2n})/2 + E_C \tag{6.1}$$

where S_{2p} (S_{2n}) is the two-proton (two-neutron) separation energy and E_C the Coulomb barrier. S_{2p} and S_{2n} of ^{54,56}Fe, ^{58,60}Ni, ^{66}Zn and of ^{64}Ni were taken from Ref. [89] and Ref. [90], respectively.

The contributions of $E1$ and $M1$ strength are almost the same for the two iron isotopes and ^{58}Ni. For ^{60}Ni, the $E1$ contribution is already two times higher than in the neighboring isotope ^{58}Ni. This changes even more when adding more neutrons. The $E1$ contribution is eleven times higher than the $M1$ part for ^{64}Ni, i.e., by adding four neutrons the ratio is increased by a factor of three. This increase gets even steeper when crossing the magic $Z = 28$ shell closure (^{66}Zn).
This behavior already shows that the processes generating $M1$ and $E1$ strengths are completely different (as described in Chapter 1). Therefore, the $E1$ and $M1$ channels will be discussed separately in the following.

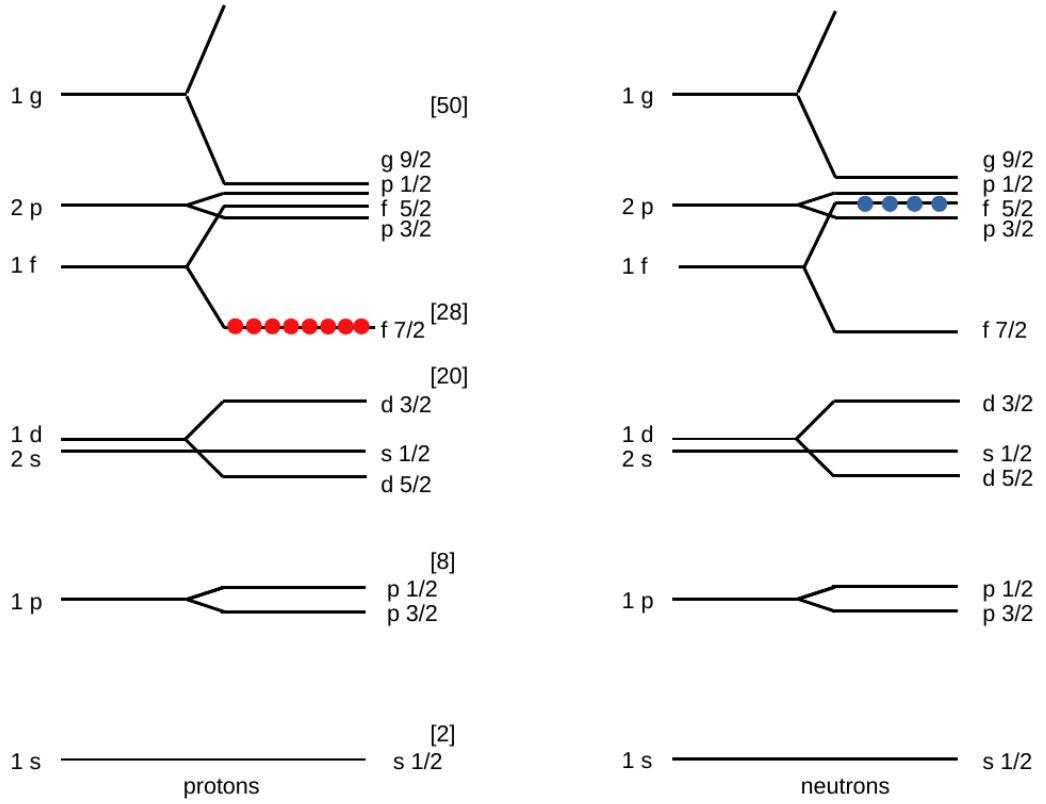

Figure 6.2: Shell-model scheme. The figure is modeled after Fig. 80 of Ref. [92]. The valence protons (red) and neutrons (blue) of ^{64}Ni are presented.

6.1 M1 transitions

As illustrated in Fig. 6.1, $M1$ transitions were identified in the dipole response of ^{66}Zn, the iron, and the nickel isotopes which were studied with linearly-polarized γ-ray beams. All these nuclides are so called fp nuclei, i.e., the valence nucleons occupy the $1f$ and $2p$ shells. A scheme of the shell model and the valence nucleons of ^{64}Ni are displayed in Fig. 6.2 and a description of the nuclear shell model can be found, e.g., in Ref. [91].

In these nuclei, a considerable amount of $M1$ spin-flip transitions is expected which is associated with the $[2p_{3/2^-}, 2p_{1/2^-}]$ and $[1f_{7/2^-}, 1f_{5/2^-}]$ configurations. For a better comparison of the strengths, the running sums of the energy-integrated cross sections for all tentatively and firmly identified $M1$ transitions were calculated for every nuclide. These are depicted in Fig. 6.3.

In general, the running sums of all nuclides except for ^{66}Zn show a step-like behavior, which

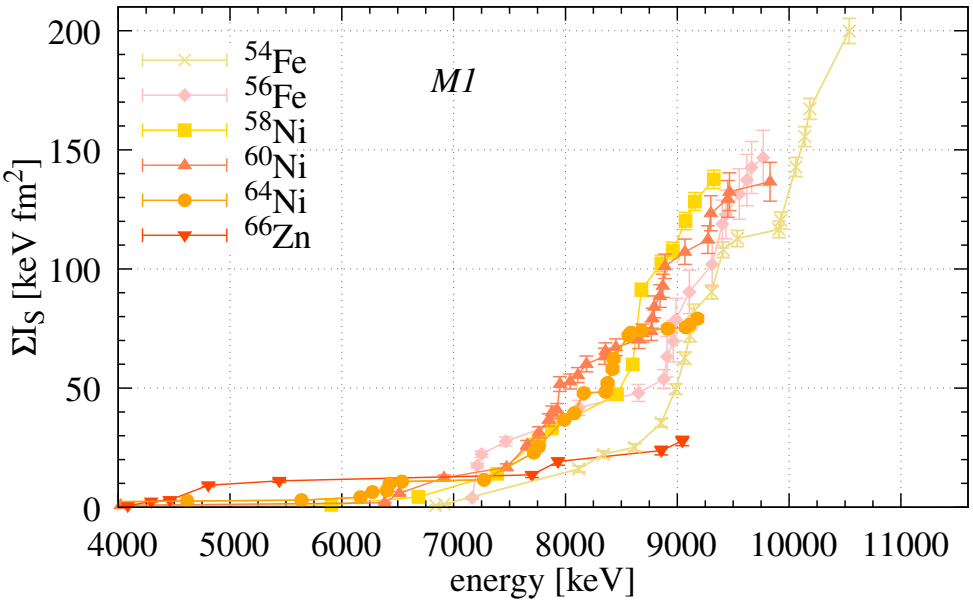

Figure 6.3: Running sums of energy-integrated cross sections of all firmly and tentatively identified, resolved $M1$ ground-state transitions above 4 MeV deduced for ^{54,56}Fe [53, 54], ^{58,60,64}Ni [55–57], and ^{66}Zn [58].

results due to individual strong $M1$ transitions. In general, the $M1$ response of ^{58}Ni and ^{60}Ni exhibit a great resemblance. This is expected since the same proton and neutron orbitals contribute to the spin-flip resonance. In Ref. [56], it is stated that the interaction of the protons in the $1f_{7/2^-}$ subshell with the neutrons in the $1f_{5/2^-}$ and $1f_{7/2^-}$ subshells leads to a decrease of the energy difference between these neutron spin-orbit partners from the iron to the nickel isotopes. This was observed by higher excitation energies of $M1$ transitions, associated with neutron excitations from the $1f_{7/2^-}$ to the $1f_{5/2^-}$ subshell, for ^{56}Fe compared to ^{58,60}Ni.
As displayed in Fig. 6.3, the running sum of the energy-integrated cross sections of ^{54}Fe shows two steep increases at higher excitation energies than ^{56}Fe and ^{58,60}Ni. The second step is located at approximately 10 MeV. Because the measurements on ^{56}Fe and ^{58,60}Ni were limited to excitation energies below 10 MeV, it cannot be excluded that $M1$ excitations above 10 MeV exist in these nuclei as well. These could result in a comparable increase of the $M1$ strength at these energies. Moreover, it should be kept in mind that it is also possible that part of the $M1$ strength is located above the neutron-separation threshold which cannot be easily observed in real-photon scattering experiment. Therefore, a final conclusion cannot be drawn.
A considerable change of the $M1$ response can also be observed from ^{60}Ni to ^{64}Ni. At approximately 9 MeV, a steep increase in the $M1$ response of ^{56}Fe and ^{58,60}Ni is present. The

absence of this step in the ^{64}Ni results causes the approximately three times smaller summed energy-integrated cross section at 9.3 MeV. As indicated in Table I in Chapter 5, no $M1$ transition was observed between 9.3 MeV and 9.7 MeV, i.e., the complete resolved, elastic $M1$ strength is already included in the comparison. It is suggested that a possible reason for this difference can be found in the occupations of different neutron shells: whereas the four valence neutrons of ^{60}Ni occupy the $2p_{3/2^-}$ subshell, in addition, the $1f_{5/2^-}$ shell is partly filled with four neutrons in the case of ^{64}Ni. Hence, neutron excitations from $1f_{7/2^-} \rightarrow 1f_{5/2^-}$ seem to be less probable and the same holds for neutron excitations from $2p_{3/2^-}$ to $2p_{1/2^-}$. Nevertheless, proton $1p-1h$ excitations from the $1f_{7/2^-}$ to the $1f_{5/2^-}$ subshell might explain the still considerable $M1$ strength of ^{64}Ni.
The comparison of the results of the $N = 36$ isotones ^{64}Ni and ^{66}Zn indicates that the $M1$ strength is approximately halved and three times less $M1$ excitations can be observed when adding two protons to the proton-magic nucleus. This might be explained by the smaller contribution of spin flips of protons from the $1f_{7/2^-}$ to the $1f_{5/2^-}$ subshell due to the two additional protons of ^{66}Zn. The importance of the contribution of proton excitations across the $Z = 28$ shell gap for ^{64}Ni was also observed in shell-model calculations included in the manuscript (see Chapter 5). Because the two additional protons of ^{66}Zn occupy the $2p_{3/2^-}$ subshell, it is suggested that the $[1f_{7/2^-}, 1f_{5/2^-}]$ contribution might be larger than that of $[2p_{3/2^-}, 2p_{1/2^-}]$ for these nuclei.
It has to be emphasized that the conclusions drawn are based only on the comparison of the experimental real-photon scattering data and a simple interpretation of the corresponding results within the shell model. Of course, the situation is much more complex resulting from the interplay of the nucleons. This is already indicated by the comparison of the $M1$ strength of ^{56}Fe and ^{58,60}Ni. For these, it was shown that the protons in the $1f_{7/2^-}$ subshell influence the neutron $1f_{7/2^-}$ and $1f_{5/2^-}$ subshells. This effect is denoted as shell evolution (see Ref. [93] and references therein).

To investigate if observed discrepancies between the $M1$ strengths of different nuclides occur due to missing strength contained in weak transitions below the sensitivity limit, the average elastic cross sections with respect to the $M1$ decay channel have to be compared (cf. Sec. 4.2.6). No average quantities were determined for ^{54,56}Fe and ^{58,60}Ni, but for ^{66}Zn [59]. Therefore, a comparison of the two $N = 36$ isotones can be conducted.
In Fig. 6.4, the disentangled average elastic cross sections with respect to $E1$ and $M1$ contributions are displayed. It was decided to show only the ^{64}Ni results deduced from the analysis of the total excitation-energy region at once to enable a better comparison with the ^{66}Zn

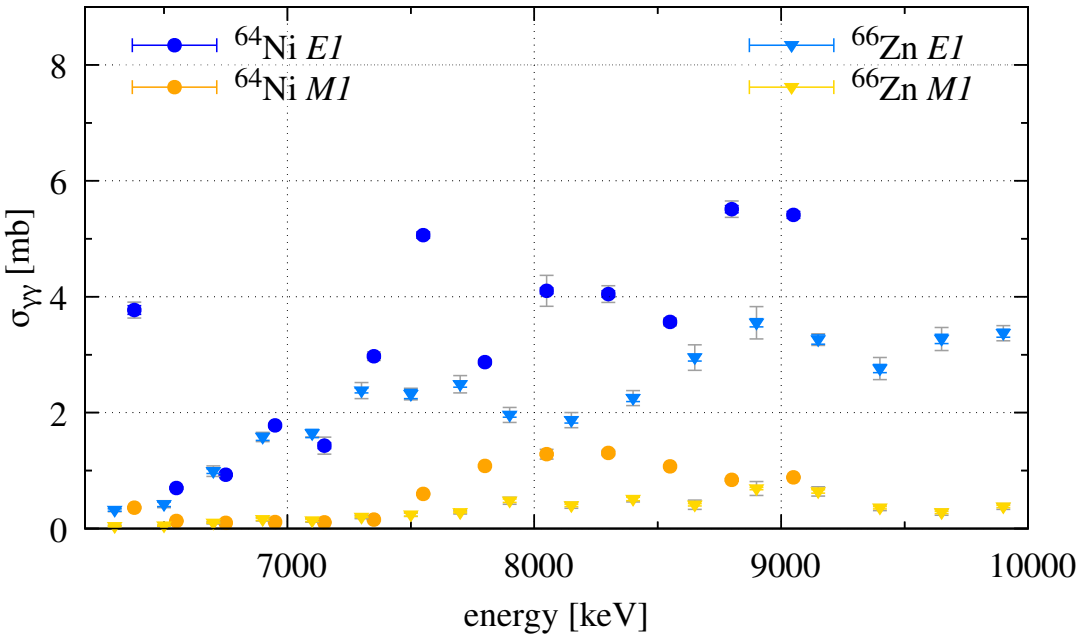

Figure 6.4: The average elastic cross sections deduced for ^{64}Ni (filled circles) and ^{66}Zn [59] (filled triangles) are illustrated. The disentanglement procedure for both isotones is the same and the $E1$ (blue) and $M1$ (orange) contributions are separately shown. The statistical (systematic) uncertainties are indicated with the corresponding colors (in gray).

data (see Sec. 4.2.6). It can be seen that $M1$ transitions contribute only little compared to $E1$ transitions to the elastic-decay channel of both isotones and absolute $M1$ values up to approximately 7500 keV look very similar. Above this energy, the $M1$ elastic cross section gets larger in both nuclei, although this increase is approximately two times higher in the case of ^{64}Ni. This is exactly what was observed in the state-to-state results (cf. Fig. 6.3) and could be predicted using the simplified picture of the nuclear shell model illustrated in Fig. 6.2.

6.2 E1 transitions

As stated in Chapter 1, the Pygmy Dipole Resonance (PDR) is observed as an accumulation of additional $E1$ strength on top of the low-energy tail of the IsoVector Giant Dipole Resonance (IVGDR). Furthermore, it was described that multimessenger investigations are needed to learn more about the properties of the excited states. Nevertheless, the comparison of real-photon scattering results along isotopic and isotonic chains can yield new insights and first indications about the underlying structures of the states.
Figure 6.1 shows the evolution of the resolved $E1$ transitions in the $A \approx 60$ mass region. It is

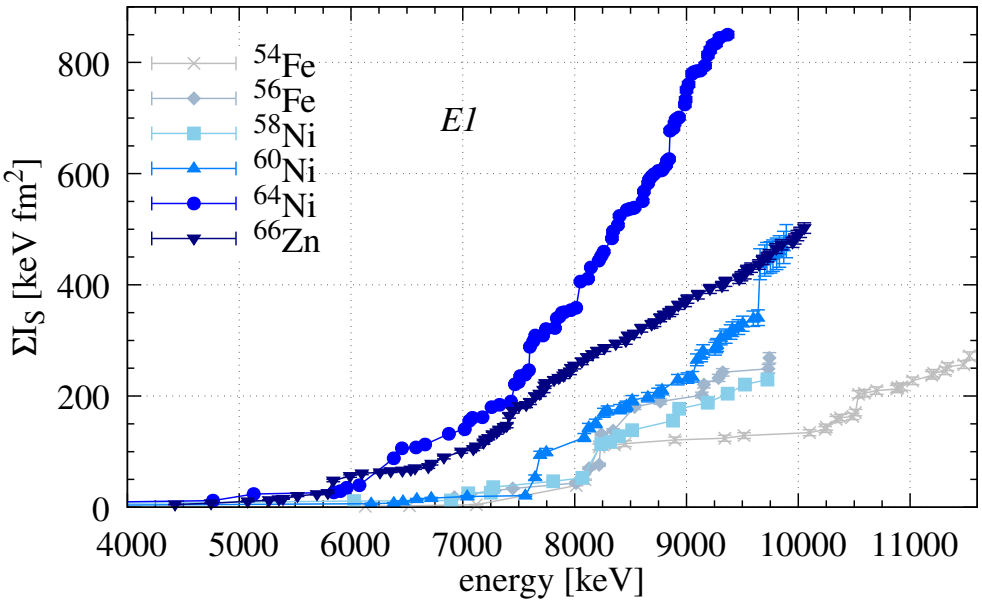

Figure 6.5: Running sums of energy-integrated cross sections of resolved, firm $E1$ ground-state transitions above 4 MeV deduced for ^{54,56}Fe [53, 54], ^{58,60,64}Ni [55–57], and ^{66}Zn [58].

indicated that the fragmentation of the strength increases with increasing neutron number in the nickel isotopic chain, i.e., the number of 1^- states is the largest for ^{64}Ni. Strikingly, the comparison of ^{64}Ni and ^{66}Zn highlights that no simple correlation between the fragmentation of the $E1$ strength and increasing neutron excess (N/Z ratio) as well as with increasing CCF energy (cf. Table 6.1) exists. Otherwise, the fragmentation of the $E1$ strength should decrease from ^{64}Ni to ^{66}Zn. Instead, adding two protons to the proton-magic $N = 36$ isotone increases the fragmentation. Whereas distinct strong transitions are present for all Ni and Fe isotopes, most induced $E1$ transitions of ^{66}Zn are relatively weak. This behavior can also be observed in the $E1$ running sums of the energy-integrated cross sections presented in Fig. 6.5, because the increase corresponding to ^{66}Zn is very smooth. In contrast, the running sums of the iron and the nickel isotopes show a more step-like behavior. This indicates that the fragmentation of the PDR is dependent, among others, on the shell structure and is higher for non-magic nuclei.

Moreover, the investigation of the running sums shows that the $E1$ strength contained in resolved, elastic transitions up to 9.3 MeV is the largest for the nucleus with the largest neutron excess ^{64}Ni. This is not surprising if, at least, some part of the low-lying $E1$ response is associated with an oscillation of excess neutrons. In contradiction to this picture stands the summed strengths of ^{60}Ni and ^{66}Zn which are similar above 9.5 MeV (cf. Fig. 6.5).

However, especially in the case of ^{66}Zn, it is important to investigate the amount of strength

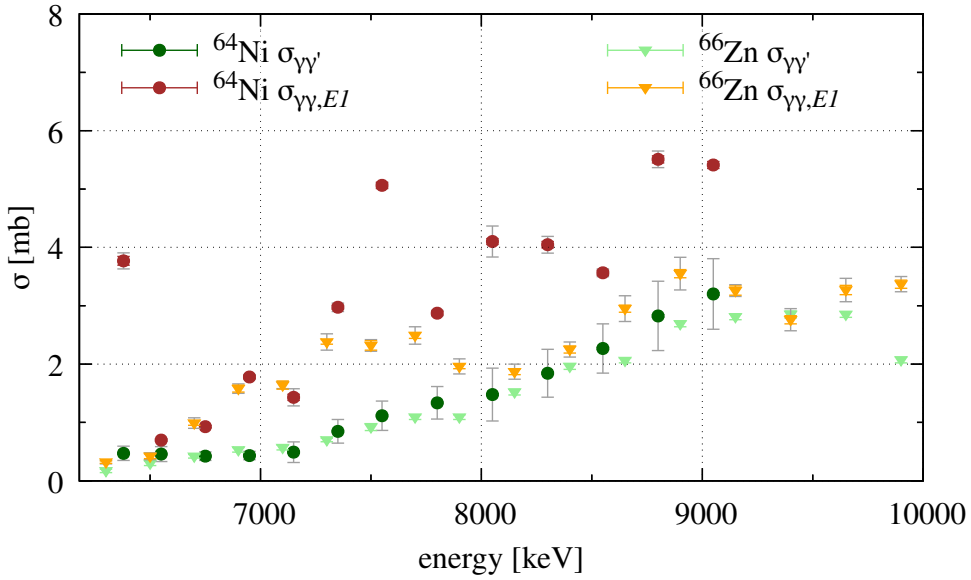

Figure 6.6: The average $E1$ cross sections of ^{64}Ni (filled circles) and ^{66}Zn [59] (filled triangles) are illustrated. The elastic contribution is shown in red and an upper limit for the $E1$ inelastic contribution is displayed in green. The statistical (systematic) uncertainties are indicated with the corresponding colors (in gray). For the inelastic cross sections of ^{66}Zn, no systematic uncertainties are given in Ref. [59].

hidden in the background before drawing final conclusions. As aforementioned, the comparison of the average elastic cross section is only possible for ^{64}Ni and ^{66}Zn. As depicted in Fig. 6.4, the overall trend of the $E1$ channel does not change if also unresolved elastic transitions are included. Up to approximately 7.5 MeV, the average elastic cross sections of both isotones are very similar besides one strong resonance of ^{64}Ni at 6.4 MeV. Above 7.5 MeV, an accumulation of strong resonances of ^{64}Ni lead to a more pronounced $E1$ response compared to ^{66}Zn. This shows that the inclusion of unresolved transitions does not change the conclusions drawn for the $E1$ channel with respect to the $N = 36$ isotones.

However, it has to be pointed out that this behavior could change when including the inelastic decay channel as described in Sec. 4.2.6. Therefore, the total $E1$ photoresponse has to be compared. As stated in Sec. 4.2.6, the disentanglement of $E1$ and $M1$ transitions was not possible in the inelastic decay channel. Hence, the presented results serve only as estimation when discussing the total $E1$ response.

As an estimation, Fig. 6.6 illustrates that the inelastic decay channels of ^{64}Ni (dark-green circles) and ^{66}Zn (light-green triangles) are very similar. This is surprising due to the different behavior of the average elastic $E1$ cross section. It is shown that an approximately equal amount of strength is contained in direct $E1$ ground-state transitions and inelastic decays for

^{66}Zn above 8 MeV. For ^{64}Ni, the main contribution to the total $E1$ cross section is exhausted by elastic transitions (approximately two thirds) up to 9.05 MeV. As mentioned in Chapter 1, the ground-state decay branching serves as indication of the complexity of the wave function of a state. Therefore, this observation might be an indication that the contribution of more complex configurations is increased for non-magic nuclides.

In conclusion, this chapter underlines the importance of performing systematic studies along isotopic and isotonic chains using the same experimental probe. The comparison of the dipole responses of neighboring nuclides can reveal properties of the investigated excitation modes.

7 Summary and outlook

In this thesis, two complementary real-photon scattering experiments on ^{64}Ni were analyzed to investigate the dipole response up to the neutron-separation threshold $S_n = 9.7\,\mathrm{MeV}$.
Two measurements using an energetically-continuous photon beam were conducted at the γELBE facility of the Helmholtz-Zentrum Dresden-Rossendorf to induce dipole transitions up to 9.4 MeV. These experiments allowed the distinction between dipole and quadrupole transitions, the extraction of absolute energy-integrated cross sections for transitions in the total excitation region, and the study of feeding contributions to lower-lying excited states.
A complementary (γ, γ') experiment on ^{64}Ni was performed at the γ^3 setup at the HIγS facility utilizing a quasimonoenergetic and linearly-polarized γ-ray beam covering excitation energies between 4.3 and 10.0 MeV. Since only states in a small energy region were excited ($\Delta E/E \approx 300\,\mathrm{keV}$), decays directly back to the ground-state (elastic decays) can be differentiated from transitions to lower-lying excited states (inelastic decays). The detector configuration of the γ^3 setup and the linear polarization of the incoming photon beam enabled the assignment of radiation characters to the observed transitions. In this way, $E1$ and $M1$ transitions were distinguished.
The combination of both experiments results in the firm identification of 87 1^- states and 23 1^+ states between 4.3 MeV and the neutron-separation threshold of ^{64}Ni. Furthermore, eight states were tentatively identified as 1^- states and two as 1^+ states. For eleven additional states, $J = 1$ was assigned. For transitions up to 9.3 MeV, absolute energy-integrated cross sections were determined.
Furthermore, average cross sections of ^{64}Ni were deduced from the HIγS data. For the average elastic cross section a disentanglement of the $E1$ and $M1$ contributions was performed. It shows that, although $M1$ strength exists in the dipole response of ^{64}Ni, its contribution is comparably small. The inelastic cross sections were estimated by using ground-state decays of the low-lying 2^+ states which collect the main part of inelastic transitions. It was found that approximately one third of the total photoabsorption cross section is exhausted by the inelastic-decay channel at excitation energies around 9.3 MeV. At lower energies, this contribution is smaller. An approximately linear increase of the inelastic cross section with increasing excitation energy was observed. However, the extracted values serve only as es-

timation of the inelastic-decay channel due to the assumption of a constant energy distribution of the photon beam and that the induced transitions of ^{64}Ni are similarly strong. For a more precise computation of the average inelastic cross sections of ^{64}Ni, an energetically-continuous analysis has to be performed using $\gamma - \gamma$ coincidences. No absolute cross sections could be determined between 9.3 MeV and S_n due to experimental reasons. Because of the importance of this energy region for the investigation of neutron-capture reactions in nucleosynthesis processes [94–96], a remeasurement should be performed.

In Chapter 5, the experimentally determined average cross sections regarding the $E1$ channel were compared to results obtained in the relativistic equation of motion (REOM) framework. The comparison showed that the theory can predict the gross structure of the $E1$ photoabsorption cross section but overestimates the experimental values by approximately a factor of two. This indicates that additional mechanisms generating the strength in the REOM calculation have to be included. Furthermore, the used experimental inelastic cross section includes not only $E1$ but also $M1$ transitions. For a conclusive comparison of the $E1$ channel, these contributions have to be disentangled.
In addition, shell-model calculations using two different model spaces were performed to investigate the $M1$ decay channel of ^{64}Ni. The results were compared to the experimentally-accessible quantity $B(M1)\downarrow \cdot \Gamma_0/\Gamma$ values because the ground-state decay branching ratios Γ_0/Γ were not determined in the experimental analyses. A good agreement between experiment and theory was achieved. It was observed that the excitation of protons across the $Z = 28$ gap play an important role using both model spaces to better reproduce the experimental data.

The evolution of the $M1$ and $E1$ channels was systematically investigated in this work by comparing ground-state decays observed in various (γ, γ') measurements on medium-mass nuclei near $Z \approx 28$. The results with respect to the $M1$ channel, which is associated with spin-flip excitations in the fp shells, were interpreted in a simple approach on the basis of the shell-model scheme. These systematic investigations have to be extended to theory. It is proposed to apply the same theoretical approach to a variety of nuclei in this mass region. These theoretical systematic investigations would complement the experimental systematics presented in this work and new insights in the interactions between nucleons generating the $M1$ strength could be gained.

The fragmentation of the $E1$ strength in the PDR region was investigated in the $A \approx 60$ nu-

clei based on resolved elastic ground-state decays. The systematic comparison revealed that the fragmentation depends on the shell structure of the nucleus as well, despite the otherwise assumed connection between PDR strength and gross nuclear parameters such as N/Z. Concerning the evolution of the absolute strengths, no final conclusion could be drawn due to the missing inelastic-decay channel. However, it is likely that such shell effects have also an impact on the absolute strengths.

The inelastic-decay channel was included in the comparison of the average $E1$ cross sections of the $N = 36$ isotones ^{64}Ni and ^{66}Zn. The average elastic $E1$ cross section of ^{64}Ni is approximately two times larger above 7.5 MeV compared to ^{66}Zn and consists of a variety of strong resonances, i.e., different patterns can be observed. In contrast, the average inelastic cross sections, which include $E1$ as well as $M1$ contributions for both isotones, show approximately the same behavior in relative and absolute scales up to 9.05 MeV. This implies that the ground-state branching ratios are considerably smaller for higher-lying states of ^{66}Zn than of ^{64}Ni up to this energy. By using this quantity as indicator for the complexity of the underlying wave functions of a state, it is suggested that the structures of the states considerably change above approximately 7.5 MeV from the proton-magic nucleus ^{64}Ni to the non-magic isotone ^{66}Zn.

To deeper investigate this assumed change in structure, theoretical calculations using, e.g., the quasiparticle-phonon model (QPM) can be performed similar to that applied for ^{120}Sn [43] and ^{208}Pb [41]. To test such theoretical calculations, the single-particle structure probed by the (d, p) reaction could be used. However, neither ^{63}Ni nor ^{65}Zn are stable and, therefore, no (d, p) or $(d, p\gamma)$ experiments can be conducted to study the single-particle structures of ^{64}Ni and ^{66}Zn. The two neighboring even-even nuclides, ^{62}Ni [42] and ^{68}Zn are accessible in (d, p) and $(d, p\gamma)$ measurements. The valence neutrons populate the $1f_{5/2}$ shell for ^{62,64}Ni and ^{66,68}Zn, i.e., the same neutron configurations will contribute in corresponding (d, p) or $(d, p\gamma)$ studies. Because of this, the impact of two additional protons above the $Z = 28$ shell closure can be investigated by extrapolating from ^{62}Ni to ^{64}Ni and from ^{68}Zn to ^{66}Zn. For this comparison, the (γ, γ')-bremsstrahlung data of ^{62}Ni up to its neutron-separation threshold of $S_n = 10.6$ MeV has to be analyzed. Furthermore, complementary (γ, γ') experiments on ^{68}Zn have to be performed in addition to a $(d, p\gamma)$ experiment on ^{67}Zn. Moreover, theoretical calculations for ^{62,64}Ni and ^{66,68}Zn have to be conducted to investigate the wave functions of the excited states.

To conclude, many real-photon scattering experiments have been performed to understand the interaction of γ rays with atomic nuclei for the last decades. The advent of new experimental

techniques and advanced facilities further improved this knowledge by, e.g., the distinction between $E1$ and $M1$ excitations. In addition, the comparison of excitation and deexcitation patterns observed during experiments with different excitation probes revealed more insights into the mechanisms generating these modes and the underlying structures of the excited states. Nevertheless, there are still properties of the various dipole-excitation modes which have not been discovered so far and further experimental and theoretical studies are necessary.

Bibliography

[1] W. C. Röntgen, *Über Eine Neue Art von Strahlen*, Berlin, Heidelberg: Springer Berlin Heidelberg, 1949 pp. 2–16, ISBN: 978-3-662-13247-0, DOI: 10.1007/978-3-662-13247-0_2.

[2] G. de Hevesy, *Some Applications of Isotopic Indicators*, www.nobelprize.org, Nobel Foundation, URL: https://www.nobelprize.org/prizes/chemistry/1943/hevesy/lecture/ access: October, 15th 2023.

[3] A. Zilges *et al.*, *The Pygmy Dipole Resonance – status and new developments*, J. Phys. Conf. Ser. **580** (2015) 012052, DOI: 10.1088/1742-6596/580/1/012052.

[4] W. Bothe and W. Gentner, *Atomumwandlungen durch γ-Strahlen*, Z. Phys. **106** (1937) 236, DOI: 10.1007/BF01340320.

[5] A. B. Migdal, J. Phys. (USSR) **8** (1944) 331.

[6] M. N. Harakeh and A. van der Woude, *Giant resonances: Fundamental high frequency modes of nuclear excitation*, Oxford University Press, 2001.

[7] H. Steinwedel *et al.*, *Hydrodynamik von Kerndipolschwingungen*, Z. Naturforsch., A **5** (1950) 413, DOI: 10.1515/zna-1950-0801.

[8] M. Goldhaber and E. Teller, *On Nuclear Dipole Vibrations*, Phys. Rev. **74** (1948) 1046, DOI: 10.1103/PhysRev.74.1046.

[9] U. Kneissl *et al.*, *Low-lying dipole modes in vibrational nuclei studied by photon scattering*, J. Phys. G Nucl. Part. Phys. **32** (2006) R217, DOI: 10.1088/0954-3899/32/8/R01.

[10] G. A. Bartholomew, *Neutron Capture Gamma Rays*, Annu. Rev. Nucl. Sci. **11** (1961) 259, DOI: 10.1146/annurev.ns.11.120161.001355.

[11] J. S. Brzosko *et al.*, *Effect of the pigmy resonance on the calculations of the neutron capture cross section*, Can. J. Phys. **47** (1969) 2849, DOI: 10.1139/p69-348.

[12] R. Mohan *et al.*, *Three-Fluid Hydrodynamical Model of Nuclei*, Phys. Rev. C **3** (1971) 1740, DOI: 10.1103/PhysRevC.3.1740.

[13] D. Vretenar *et al.*, *Toroidal dipole resonances in the relativistic random phase approximation*, Phys. Rev. C **65** (2002) 021301, DOI: 10.1103/PhysRevC.65.021301.

[14] A. Repko *et al.*, *Toroidal nature of the low-energy $E1$ mode*, Phys. Rev. C **87** (2013) 024305, DOI: 10.1103/PhysRevC.87.024305.

[15] P. Von Neumann-Cosel *et al.*, *Evidence for a toroidal electric dipole mode in nuclei*, (2023), URL: https://www.researchgate.net/publication/374731378_Evidence_for_a_toroidal_electric_dipole_mode_in_nuclei access: October, 16th 2023.

[16] E. Lanza and A. Vitturi, *Handbook of Nuclear Physics*, ed. by I. Tanihata, H. Toki, and T. Kajino, Springer Singapore, 2023, chap. Theoretical Description of Pygmy (Dipole) Resonances.

[17] A. Bracco *et al.*, *Isoscalar and isovector dipole excitations: Nuclear properties from low-lying states and from the isovector giant dipole resonance*, Prog. Part. Nucl. Phys. **106** (2019) 360, DOI: https://doi.org/10.1016/j.ppnp.2019.02.001.

[18] E.G. Lanza *et al.*, *Three-Fluid Hydrodynamical Model of Nuclei*, Prog. Part. Nucl. Phys. **129** (2023) 104006, DOI: https://doi.org/10.1016/j.ppnp.2022.104006.

[19] D. Savran *et al.*, *Experimental studies of the Pygmy Dipole Resonance*, Prog. Part. Nucl. Phys. **70** (2013) 210, DOI: https://doi.org/10.1016/j.ppnp.2013.02.003.

[20] F. R. Metzger, *Resonance Fluorescence in Nuclei*, Prog. Nucl. Phys. **7** (1959) 53.

[21] U. Kneissl *et al.*, *Investigation of nuclear structure by resonance fluorescence scattering*, Prog. Part. Nucl. Phys. **37** (1996) 349, DOI: https://doi.org/10.1016/0146-6410(96)00055-5.

[22] A. Zilges *et al.*, *Photonuclear reactions—From basic research to applications*, Prog. Part. Nucl. Phys. **122** (2022) 103903, DOI: https://doi.org/10.1016/j.ppnp.2021.103903.

[23] K. Govaert *et al.*, *Dipole excitations to bound states in ^{116}Sn and ^{124}Sn*, Phys. Rev. C **57** (1998) 2229, DOI: 10.1103/PhysRevC.57.2229.

[24] B. Özel-Tashenov *et al.*, *Low-energy dipole strength in $^{112,120}Sn$*, Phys. Rev. C **90** (2014) 024304, DOI: 10.1103/PhysRevC.90.024304.

[25] F. Schlüter, *Untersuchung der elektrischen Dipolstärke unterhalb der Teilchenschwelle in ^{124}Sn*, Diploma thesis, University of Cologne, 2011.

[26] J. Endres *et al.*, *Structure of the pygmy dipole resonance in ^{124}Sn*, Phys. Rev. C **85** (2012) 064331, DOI: 10.1103/PhysRevC.85.064331.

[27] M. Müscher *et al.*, *High-sensitivity investigation of low-lying dipole strengths in* ^{120}Sn, Phys. Rev. C **102** (2020) 014317, DOI: 10.1103/PhysRevC.102.014317.

[28] R. Schwengner *et al.*, *Pygmy dipole strength in* ^{86}Kr *and systematics of* $N = 50$ *isotones*, Phys. Rev. C **87** (2013) 024306, DOI: 10.1103/PhysRevC.87.024306.

[29] J. Wilhelmy *et al.*, *Dipole response of* ^{87}Rb *and its impact on the* $^{86}Rb(n,\gamma)^{87}Rb$ *cross section*, Phys. Rev. C **102** (2020) 044327, DOI: 10.1103/PhysRevC.102.044327.

[30] R. Schwengner *et al.*, *Dipole response of* ^{88}Sr *up to the neutron-separation energy*, Phys. Rev. C **76** (2007) 034321, DOI: 10.1103/PhysRevC.76.034321.

[31] N. Benouaret *et al.*, *Dipole strength in* ^{89}Y *up to the neutron-separation energy*, Phys. Rev. C **79** (2009) 014303, DOI: 10.1103/PhysRevC.79.014303.

[32] R. Schwengner *et al.*, *Pygmy dipole strength in* ^{90}Zr, Phys. Rev. C **78** (2008) 064314, DOI: 10.1103/PhysRevC.78.064314.

[33] G. Rusev *et al.*, *Enhanced electric dipole strength below particle-threshold as a consequence of nuclear deformation*, Phys. Rev. C **79** (2009) 061302, DOI: 10.1103/PhysRevC.79.061302.

[34] D. Savran *et al.*, *Multi-messenger investigation of the Pygmy Dipole Resonance in* ^{140}Ce, Phys. Lett. B **786** (2018) 16, DOI: https://doi.org/10.1016/j.physletb.2018.09.025.

[35] D. Savran *et al.*, *Nature of the Pygmy Dipole Resonance in* ^{140}Ce *Studied in* $(\alpha, \alpha'\gamma)$ *Experiments*, Phys. Rev. Lett. **97** (2006) 172502, DOI: 10.1103/PhysRevLett.97.172502.

[36] J. Endres *et al.*, *Splitting of the pygmy dipole resonance in* ^{138}Ba *and* ^{140}Ce *observed in the* $(\alpha, \alpha'\gamma)$ *reaction*, Phys. Rev. C **80** (2009) 034302, DOI: 10.1103/PhysRevC.80.034302.

[37] J. Endres *et al.*, *Isospin Character of the Pygmy Dipole Resonance in* ^{124}Sn, Phys. Rev. Lett. **105** (2010) 212503, DOI: 10.1103/PhysRevLett.105.212503.

[38] F. C. L. Crespi *et al.*, *Isospin Character of Low-Lying Pygmy Dipole States in* ^{208}Pb *via Inelastic Scattering of* ^{17}O *Ions*, Phys. Rev. Lett. **113** (2014) 012501, DOI: 10.1103/PhysRevLett.113.012501.

[39] L. Pellegri *et al.*, *Pygmy dipole resonance in* ^{124}Sn *populated by inelastic scattering of* ^{17}O, Phys. Lett. B **738** (2014) 519, DOI: https://doi.org/10.1016/j.physletb.2014.08.029.

[40] F. C. L. Crespi *et al.*, 1^- *and* 2^+ *discrete states in* ^{90}*Zr populated via the* (^{17}*O,*^{17}*O' γ*) *reaction*, Phys. Rev. C **91** (2015) 024323, DOI: 10.1103/PhysRevC.91.024323.

[41] M. Spieker *et al.*, *Accessing the Single-Particle Structure of the Pygmy Dipole Resonance in* ^{208}*Pb*, Phys. Rev. Lett. **125** (2020) 102503, DOI: 10.1103/PhysRevLett.125.102503.

[42] M. Spieker *et al.*, *Experimental study of excited states of* ^{62}*Ni via one-neutron* (*d*, *p*) *transfer up to the neutron-separation threshold and characteristics of the pygmy dipole resonance states*, Phys. Rev. C **108** (2023) 014311, DOI: 10.1103/PhysRevC.108.014311.

[43] M. Weinert *et al.*, *Microscopic Structure of the Low-Energy Electric Dipole Response of* ^{120}*Sn*, Phys. Rev. Lett. **127** (2021) 242501, DOI: 10.1103/PhysRevLett.127.242501.

[44] P. Kuchenbrod, *Towards the reduced dipole transition strength B(E1) in* ^{120}*Sn below the neutron threshold*, Master's thesis, TU Darmstadt, 2022.

[45] K. Heyde *et al.*, *Magnetic dipole excitations in nuclei: Elementary modes of nucleonic motion*, Rev. Mod. Phys. **82** (2010) 2365, DOI: 10.1103/RevModPhys.82.2365.

[46] N. Pietralla *et al.*, *Experiments on multiphonon states with proton–neutron mixed symmetry in vibrational nuclei*, Prog. Part. Nucl. Phys. **60** (2008) 225, DOI: https://doi.org/10.1016/j.ppnp.2007.08.002.

[47] N. Lo Iudice and F. Palumbo, *New Isovector Collective Modes in Deformed Nuclei*, Phys. Rev. Lett. **41** (1978) 1532, DOI: 10.1103/PhysRevLett.41.1532.

[48] N. Lo Iudice and F. Palumbo, *Positive parity isovector collective states in deformed nuclei*, Nucl. Phys. A **326** (1979) 193, DOI: https://doi.org/10.1016/0375-9474(79)90375-0.

[49] F. Iachello, *Electron scattering in the interacting boson model*, Nucl. Phys. A **358** (1981) 89, DOI: https://doi.org/10.1016/0375-9474(81)90308-0.

[50] A.E.L. Dieperink, *Geometrical analysis of the interacting boson model*, Prog. Part. Nucl. Phys. **9** (1983) 121, DOI: https://doi.org/10.1016/0146-6410(83)90016-9.

[51] D. Bohle *et al.*, *New magnetic dipole excitation mode studied in the heavy deformed nucleus* ^{156}*Gd by inelastic electron scattering*, Phys. Lett. B **137** (1984) 27, DOI: https://doi.org/10.1016/0370-2693(84)91099-2.

[52] W. Ziegler *et al.*, *Orbital magnetic dipole strength in* ^{148,150,152,154}*Sm and nuclear deformation*, Phys. Rev. Lett. **65** (1990) 2515, DOI: 10.1103/PhysRevLett.65.2515.

[53] R. Schwengner *et al.*, *Electric and magnetic dipole strength in ^{54}Fe*, Phys. Rev. C **101** (2020) 064303, DOI: 10.1103/PhysRevC.101.064303.

[54] T. Shizuma *et al.*, *Dipole strength distribution in ^{56}Fe*, Phys. Rev. C **87** (2013) 024301, DOI: 10.1103/PhysRevC.87.024301.

[55] F. Bauwens *et al.*, *Dipole transitions to bound states in ^{56}Fe and ^{58}Ni*, Phys. Rev. C **62** (2000) 024302, DOI: 10.1103/PhysRevC.62.024302.

[56] M. Scheck *et al.*, *Photoresponse of ^{60}Ni below 10-MeV excitation energy: Evolution of dipole resonances in f p-shell nuclei near $N = Z$*, Phys. Rev. C **88** (2013) 044304, DOI: 10.1103/PhysRevC.88.044304.

[57] M. Scheck *et al.*, *Decay pattern of the pygmy dipole resonance in ^{60}Ni*, Phys. Rev. C **87** (2013) 051304, DOI: 10.1103/PhysRevC.87.051304.

[58] R. Schwengner *et al.*, *Electric and magnetic dipole strength in ^{66}Zn*, Phys. Rev. C **103** (2021) 024312, DOI: 10.1103/PhysRevC.103.024312.

[59] D. Savran *et al.*, *Model-independent determination of the dipole response of* ^{66}Zn *using quasimonoenergetic and linearly polarized photon beams*, Phys. Rev. C **106** (2022) 044324, DOI: 10.1103/PhysRevC.106.044324.

[60] K. S. Krane *et al.*, *Directional correlations of gamma radiations emitted from nuclear states oriented by nuclear reactions or cryogenic methods*, At. Data Nucl. Data Tables **11** (1973) 351, DOI: https://doi.org/10.1016/S0092-640X(73)80016-6.

[61] L. W. Fagg and S. S. Hanna, *Polarization Measurements on Nuclear Gamma Rays*, Rev. Mod. Phys. **31** (1959) 711, DOI: 10.1103/RevModPhys.31.711.

[62] R. Schwengner *et al.*, *The photon-scattering facility at the superconducting electron accelerator ELBE*, Nucl. Instrum. Methods Phys. Res., Sect. A **555** (2005) 211, DOI: https://doi.org/10.1016/j.nima.2005.09.024.

[63] H. R. Weller *et al.*, *Research opportunities at the upgraded HIγS facility*, Prog. Part. Nucl. Phys. **62** (2009) 257, DOI: https://doi.org/10.1016/j.ppnp.2008.07.001.

[64] B. Löher *et al.*, *The high-efficiency γ-ray spectroscopy setup γ3 at HIγS*, Nucl. Instrum. Methods Phys. Res., Sect. A **723** (2013) 136, DOI: https://doi.org/10.1016/j.nima.2013.04.087.

[65] H. G. Essel and N. Kurz, *The general purpose data acquisition system MBS*, IEEE Transactions on Nuclear Science **47** (2000) 337, DOI: 10.1109/23.846176.

[66] F. Ajzenberg-Selove, *Energy levels of light nuclei A = 11–12*, Nucl. Phys. A **506** (1990) 1, DOI: https://doi.org/10.1016/0375-9474(90)90271-M.

[67] G. Rusev *et al.*, *Multipole mixing ratios of transitions in* ^{11}B, **79** (2009) 047601, DOI: 10.1103/PhysRevC.79.047601.

[68] G. Roche *et al.*, *Bremsstrahlung Cross-Section Formula Including a High-Order Coulomb Correction*, Phys. Rev. A **5** (1972) 2403, DOI: 10.1103/PhysRevA.5.2403.

[69] F. Salvat *et al.*, *Analytical Dirac-Hartree-Fock-Slater screening function for atoms (Z=1–92)*, Phys. Rev. A **36** (1987) 467, DOI: 10.1103/PhysRevA.36.467.

[70] E. Haug, *Bremsstrahlung cross-section with screening and Coulomb corrections at high energies*, Radiat. Phys. Chem. **77** (2008) 207, DOI: https://doi.org/10.1016/j.radphyschem.2007.10.003.

[71] R. Massarczyk *et al.*, *Electromagnetic dipole strength of* ^{136}*Ba below the neutron separation energy*, Phys. Rev. C **86** (2012) 014319, DOI: 10.1103/PhysRevC.86.014319.

[72] R. Schwengner, private communication (2018).

[73] B. Singh and J. Chen, *Nuclear Data Sheets for A=64*, Nucl. Data Sheets **178** (2021) 41, DOI: https://doi.org/10.1016/j.nds.2021.11.002.

[74] U. Friman-Gayer *et al.*, *Histogram original reconstruction spectrum tool*, https://github.com/uga-uga/Horst, 2022.

[75] U. Friman-Gayer *et al.*, *GEANT4 simulation of the Upper Target Room (UTR) at the HIGS facility*, https://github.com/uga-uga/utr, 2022.

[76] S. Agostinelli *et al.*, *Geant4—a simulation toolkit*, Nucl. Instrum. Methods Phys. Res., Sect. A **506** (2003) 250, DOI: https://doi.org/10.1016/S0168-9002(03)01368-8.

[77] J. Allison *et al.*, *Geant4 developments and applications*, IEEE Transactions on Nuclear Science **53** (2006) 270, DOI: 10.1109/TNS.2006.869826.

[78] J. Allison *et al.*, *Recent developments in Geant4*, Nucl. Instrum. Methods Phys. Res., Sect. A **835** (2016) 186, DOI: https://doi.org/10.1016/j.nima.2016.06.125.

[79] N. Pietralla *et al.*, *Parity Measurements of Nuclear Levels Using a Free-Electron-Laser Generated γ-Ray Beam*, Phys. Rev. Lett. **88** (2001) 012502, DOI: 10.1103/PhysRevLett.88.012502.

[80] J. Isaak *et al.*, *Dipole response in* ^{128,130}Te *below the neutron threshold*, Phys. Rev. C **103** (2021) 044317, DOI: 10.1103/PhysRevC.103.044317.

[81] Y. Wu, private communication (2022).

[82] C. Sun and Y. K. Wu, *Theoretical and simulation studies of characteristics of a Compton light source*, Phys. Rev. ST Accel. Beams **14** (2011) 044701, DOI: 10.1103/PhysRevSTAB.14.044701.

[83] M. Tamkas *et al.*, *Low-lying dipole strength in the well-deformed nucleus* ^{156}Gd, Nucl. Phys. A **987** (2019) 79, DOI: https://doi.org/10.1016/j.nuclphysa.2019.03.014.

[84] C. Romig *et al.*, *Low-lying dipole strength of the open-shell nucleus* ^{94}*Mo*, Phys. Rev. C **88** (2013) 044331, DOI: 10.1103/PhysRevC.88.044331.

[85] J. Isaak *et al.*, *Constraining nuclear photon strength functions by the decay properties of photo-excited states*, Phys. Lett. B **727** (2013) 361, DOI: https://doi.org/10.1016/j.physletb.2013.10.040.

[86] A. P. Tonchev *et al.*, *Spectral Structure of the Pygmy Dipole Resonance*, Phys. Rev. Lett. **104** (2010) 072501, DOI: 10.1103/PhysRevLett.104.072501.

[87] M. Müscher *et al.*, *Low-lying dipole response of* ^{64}Ni, Phys. Rev. C **109** (2024) 044318, DOI: 10.1103/PhysRevC.109.044318.

[88] T. Schüttler, *Untersuchung der Dipolstärke in* ^{62}*Ni*, Bachelor's thesis, University of Cologne, 2022.

[89] M. Wang *et al.*, *The AME 2012 atomic mass evaluation (II). Tables, graphs and references**, Chinese Physics C **36** (2012) 1603, DOI: 10.1088/1674-1137/36/12/003.

[90] M. Wang *et al.*, *The AME 2020 atomic mass evaluation (II). Tables, graphs and references**, Chinese Physics C **45** (2021) 030003, DOI: 10.1088/1674-1137/abddaf.

[91] K. L. G. Heyde, *The Nuclear Shell Model*, Springer Berlin, Heidelberg, 1990.

[92] Theo Mayer-Kuckuk, *Kernphysik*, ger, 7., überarb. und erw. Aufl, Stuttgart [u.a.]: Teubner, 2002, ISBN: 3519132230.

[93] T. Otsuka *et al.*, *Evolution of shell structure in exotic nuclei*, Rev. Mod. Phys. **92** (2020) 015002, DOI: 10.1103/RevModPhys.92.015002.

[94] L. Crespo Campo *et al.*, *Statistical γ-decay properties of* ^{64}*Ni and deduced (n, γ) cross section of the s-process branch-point nucleus* ^{63}*Ni*, Phys. Rev. C **94** (2016) 044321, DOI: 10.1103/PhysRevC.94.044321.

[95] C. Lederer *et al.*, ^{62}*Ni(n, γ) and* ^{63}*Ni(n, γ) cross sections measured at the n_TOF facility at CERN*, Phys. Rev. C **89** (2014) 025810, DOI: 10.1103/PhysRevC.89.025810.

[96] M. Weigand *et al.*, ^{63}*Ni*(n, γ) *cross sections measured with DANCE*, Phys. Rev. C **92** (2015) 045810, DOI: 10.1103/PhysRevC.92.045810.

List of Figures

List of Tables

Danksagung

Ich möchte mich ganz herzlich bei Herrn Prof. Dr. Andreas Zilges bedanken, dass er mir die Möglichkeit gegeben hat, auch meine Dissertation in seiner Arbeitsgruppe zu schreiben. Die Freiheiten und das Vertrauen, das er seinen Doktoranden und Doktorandinnen entgegenbringt, hat es mir ermöglicht, mich weiterzuentwickeln und vieles zu lernen. Ich habe die Möglichkeit bekommen, auf vielen Konferenzen und Workshops meine Arbeit zu präsentieren und viele unterschiedliche Eindrücke und Einblicke zu gewinnen, wofür ich sehr dankbar bin.

Ein großer Dank geht an Herrn Prof. Dr. Jan Jolie für die Begutachtung dieser Arbeit.

Für die Übernahme des Vorsitzes der Prüfungskommission danke ich Herrn Prof. Dr. Joachim Krug.

Ich möchte mich bei Deniz Savran für seine Hilfe und die Beantwortung meiner zahlreichen Fragen bezüglich der Datenanalyse bedanken. Weiterhin gilt mein Dank Johann Isaak und Udo Friman-Gayer, die mich ebenfalls bei der Datenanalyse unterstützt haben und mir ihre Codes zur Verfügung gestellt haben. Es hat mich immer wieder begeistert, wie hilfsbereit alle KRFler, die ich kennenlernen durfte, sind und es ein wirklich angenehmes Zusammenarbeiten ist ohne Konkurrenzdenken.

Ich bedanke mich ganz herzlich bei Herrn Dr. Ronald Schwengner für seine Unterstützung bei den unzähligen Experimenten, die wir in Dresden durchführen durften in den letzten Jahren. Seine Hilfe bei den experimentellen Arbeiten, aber auch die Theorierechnungen, die er im Rahmen dieser Arbeit durchgeführt hat und seine ständige Bereitschaft, meine Fragen zu beantworten, waren sehr wichtig und hilfreich für mich.

Ein weiterer Dank geht an alle jetzigen und ehemaligen Gruppenmitglieder der AG Zilges. Der freundliche Umgang und die netten Unterhaltungen haben dazu beigetragen, dass ich immer gerne in das Institut gekommen bin. (Die Einführung des Kuchenmittwochs war natürlich die beste und wichtigste Idee.) Ich möchte besonders Anna, Sarah, Felix, Mark, Michelle und Elena hervorheben, die mir zu guten Freunden und Freundinnnen geworden sind. Ich bin

wirklich dankbar dafür, dass ich euch kennenlernen konnte und mit euch arbeiten durfte.

Desweiteren möchte ich mich bei der ”Pygmy-Gang” bedanken. Dabei danke ich vor allem Micha, für all die lustigen und angenehmen (Italien-)Reisen, die wir zusammen erleben durften und auch für jede Diskussion über ”die” Pygmy. Deine menschenfreundliche, offene Art und dein Verständnis hat das Arbeiten mit dir immer sehr angenehm gemacht. Außerdem bedanke ich mich herzlich bei Julius und Flo, die mir immer mit Rat und Tat zur Seite standen und sich geduldig meine Erläuterungen von neuauftretenden Problemen angehört und zu der Lösungsfindung beigetragen haben. An dieser Stelle möchte ich mich auch nochmal dafür bedanken, dass ihr, Micha, Flo und Tanja, diese Arbeit und das Manuskript (auch in kürzester Zeit) korrekturgelesen habt und mir somit maßgeblich bei dem Erstellen dieser Arbeit, geholfen habt. Ohne eure Hilfe wäre das so nicht möglich gewesen.

Natürlich ist es auch wichtig, dass es zwischendurch eine gute Ablenkung von der Arbeit gibt. Diese habe ich oft in Büro 204 gefunden. Ich danke allen ”Bewohnern” (und auch vielen der ehemaligen) dieses Büros für viele schöne und lustige Abende (und manchmal auch schon Nachmittage). Es tat immer gut, bei euch vorbeizukommen und einfach auch mal über etwas anderes als die Arbeit zu reden, wenn ich mal eine Pause brauchte. Natürlich gab es dabei auch die ein oder andere Physikdiskussion, die mir immer wieder gezeigt hat, dass ich Kernphysik interessant finde. Hervorheben möchte ich Arwin, der tapfer die gesamte Arbeit korrekturgelesen und sich getraut hat, noch Anmerkungen zu machen.

Natürlich danke ich auch meiner Familie und meinen Freunden, die über die gesamten Jahre für mich da waren und mir den Rücken stärkten. Die Ablenkung und Freude, die ihr mir gegeben habt, hat mir immer Kraft gegeben.

Erklärung zur Dissertation

gemäß der Promotionsordnung vom 12. März 2020

Hiermit versichere ich an Eides statt, dass ich die vorliegende Dissertation selbstständig und ohne die Benutzung anderer als der angegebenen Hilfsmittel und Literatur angefertigt habe. Alle Stellen, die wörtlich oder sinngemäß aus veröffentlichten und nicht veröffentlichten Werken dem Wortlaut oder dem Sinn nach entnommen wurden, sind als solche kenntlich gemacht. Ich versichere an Eides statt, dass diese Dissertation noch keiner anderen Fakultät oder Universität zur Prüfung vorgelegen hat; dass sie - abgesehen von unten angegebenen Teilpublikationen und eingebundenen Artikeln und Manuskripten - noch nicht veröffentlicht worden ist sowie, dass ich eine Veröffentlichung der Dissertation vor Abschluss der Promotion nicht ohne Genehmigung des Promotionsausschusses vornehmen werde. Die Bestimmungen dieser Ordnung sind mir bekannt. Darüber hinaus erkläre ich hiermit, dass ich die Ordnung zur Sicherung guter wissenschaftlicher Praxis und zum Umgang mit wissenschaft-lichem Fehlverhalten der Universität zu Köln gelesen und sie bei der Durchführung der Dissertation zugrundeliegenden Arbeiten und der schriftlich verfassten Dissertation beachtet habe und verpflichte mich hiermit, die dort genannten Vorgaben bei allen wissenschaftlichen Tätigkeiten zu beachten und umzusetzen. Ich versichere, dass die eingereichte elektronische Fassung der eingereichten Druckfassung vollständig entspricht.

Teilpublikationen:
M. Müscher *et al.*, *Low-lying dipole response of* ^{64}*Ni*, Physical Review C **109** (2024), 044318

Diese Dissertation beinhaltet die Gewinnung von Primärdaten sowie die Analyse solcher Daten, die auf den Servern des Instituts für Kernphysik der Universität zu Köln gesichert und zugänglich sind.

Köln, den 25.04.2024

(Miriam Müscher)